Semiconductors, Vol. 34, No. 12, 2000, pp. 1355–1362. Translated from Fizika i Tekhnika Poluprovodnikov, Vol. 34, No. 12, 2000, pp. 1409–1416.

REVIEWS

The Scanning Tunneling Microscopy and Scanning Tunneling Spectroscopy of Amorphous Carbon

V. I. Ivanov-Omskiĭ, A. B. Lodygin*, and S. G. Yastrebov

Ioffe Physicotechnical Institute, Russian Academy of Sciences, Politekhnicheskaya ul. 26, St. Petersburg, 194021 Russia

**e-mail: lodygin@pop.ioffe.rssi.ru*

Submitted May 11, 2000; accepted for publication June 11, 2000

Abstract—The most important methods for studying the surface of amorphous diamond-like carbon are scanning tunneling microscopy and scanning tunneling spectroscopy. In this review, publications concerned with studying the topography and electronic properties of the surface of amorphous diamond-like carbon films using a tunneling microscope are considered; related publications devoted to the microprobe study of field emission from amorphous carbon and to the tunneling microscopy of metal–carbon nanocomposites are also reviewed. *© 2000 MAIK "Nauka/Interperiodica".*

1. INTRODUCTION

Interest in amorphous diamond-like carbon (DLC) has persisted for the last decade. Initially, the amorphous-carbon films attracted the attention of researchers due to the high strength, chemical resistance, hardness, and the wide-range optical transparency of these films [1]. This made it possible to consider DLC film as a material for the development of universal coating. In addition, a DLC film is of interest as an object that contains spontaneously emerging nanometer-sized structural features.

In the second half of the 1990s, it became clear that DLC films are also promising as materials for cold cathodes by virtue of a low threshold for field emission [2]. The unique properties of amorphous carbon are related to special features of its mesoscopic structure (see, for example, [3]). The films of amorphous carbon (*a*-C) and also of hydrogenated amorphous carbon (*a*-C:H) consist of two mutually embedded phases: (i) a diamond-like phase that features the sp^3 hybridization of carbon atoms, a tetrahedral structure, and a wide (up to 4 eV) band gap, and (ii) a graphite-like phase that is composed of fragments of graphite planes and other distorted fragments, such as the units of the fullerene molecules. The latter phase features the sp^2 hybridization, comparatively high electrical conductivity, and a band gap that is either narrow or zero, depending on the cluster size. The two-phase model of amorphous carbon was suggested by J. Robertson and E. O'Reilly in 1987 [4].

Characteristic cluster sizes of each phase can be up to several nanometers [5]. Therefore, the methods that can be used to study the topography and electronic structure of material with nanometer and subnanometer resolution are especially important for gaining insight into the structure of amorphous diamond-like carbon. Scanning tunneling microscopy and scanning tunneling spectroscopy are exactly such methods. However, the high resistivity of amorphous carbon has prevented these methods from being used with good results in studies of this material for a long time.

2. SCANNING TUNNELING MICROSCOPY OF AMORPHOUS CARBON

B. Marchon, M. Salmeron, and W. Siekhaus were apparently the first to study the amorphous diamond-like carbon using a scanning tunneling microscope (STM) [6]. The measurements were performed in an atmospheric-air medium. The material studied was in the form of 100 to 300-Å-thick DLC films deposited by magnetron sputtering onto metal substrates in an argon atmosphere.

As a rule, a tunneling microscope either operates in the constant-elevation mode (in which case the tip is moved by the drive above the sample surface, and the tunnel current is measured for a constant voltage) or in the mode of constant tunneling current (in which case the STM's feedback loop maintains the distance between the tip and the surface such that the tunneling current is equal to a prescribed value). Both modes were used in [6] to study the surface. The resistance of the tunnel junction was $2 \times 10^6\ \Omega$, and it was noted [6] that a large fraction of this resistance might be attributed to the film itself. No indications of a structure were observed in some of the images obtained [6]; apparently, this indicated that the resistivity of the films was high, thus precluding the use of the STM method. However, an atomic-scale resolution was attained for some of the samples; thus, it was possible to directly observe the surface structure of *a*-C films. Figure 1 shows an image obtained in the constant-elevation mode. The joined six- and five-carbon rings can be distinguished on the right in Fig. 1. Distances between the atoms in

Fig. 1. An STM image of an *a*-C film; the image was obtained with a bias voltage of 20 mV applied to the film in the constant-elevation mode. The shown surface area is 28×12 Å^2 [6].

Fig. 2. An STM image of an *a*-C film; the image was obtained in the constant-current mode. The shown surface area is 40×40 Å^2 [6].

these rings are 1.3–1.6 Å, which corresponds to the interatomic distance for carbon with different types of bonds. The five-carbon rings represent a fairly stable configuration of sp^3-hybridized carbon because the valence angle in these rings (108°) is almost the same as for the tetrahedral structure (109.5°). Such rings may form both at the surface itself and in the gaseous phase even prior to deposition. The latter is confirmed by the mass-spectrometry data [7]. On the left in Fig. 1, one can see a distorted hexagonal configuration that corresponds to a graphite domain ~15 Å in size. The light areas in the CMT image correspond to the π bonds because the electron energy in the π-bonded carbon state is the closest to the Fermi energy. It was noted [6] that the observed pattern (each carbon atom can be distinguished) is indicative of the Kekule-localized π bonds, which is characteristic of small polycyclic hydrocarbons. It should be mentioned for the sake of comparison that only every second carbon atom can be distinguished in an STM image of the crystalline-graphite surface (see [8]). This effect is caused by interplane links in the graphite, and the absence of this effect indicates that there is no laminated structure characteristic of graphite [8].

The absence of features indicative of the long-range order in the images confirms that the observed pattern is caused by the film structure rather than by parasitic multiple reproductions of a single feature.

Figure 2 shows an STM image of a region that has hexagonal symmetry, has an interatomic distance characteristic of graphite (1.42 Å), and is no larger than 15 Å; the image was obtained [6] in the constant-current (10 nA) mode with a bias voltage of +20 mV. Other features of interest are observed in the right-hand and upper parts of Fig. 2; these features correspond to the domains with hexagonal symmetry and an interatomic distance of ~2.5 Å, which corresponds to the (111) plane in diamond. Thus, both the graphite- and diamond-like fragments are present on the surface of amorphous diamond-like carbon. Regular structures with a step of 2.7×4.5 Å, which corresponded to the reconstructed 1×2 diamond surface, could be observed [6] in addition to the above-mentioned structures. Such a reconstruction is characteristic of diamond when free bonds at the diamond surface are not saturated with hydrogen. This is experimentally observed for crystalline diamond using an STM [9].

The influence of the substrate temperature on the structure of *a*-C film was studied and reported elsewhere [10]. As previously [6], dc magnetron sputtering was used [10] to obtain the *a*-C films. Atomic-scale resolution was attained [10]. Figure 3 shows the STM images of the films [10] grown at 450 and 30°C. Graphite domains 20–40 Å in size are observed on the film surfaces. An increase in the substrate temperature results in a shift of equilibrium to the formation of sp^2-hybridized clusters and in the enhancement of structural regularity. The fact that each graphite atom (rather than each second one) is observed in the STM images is related [10] to the special features of packing in a graphite domain. The neighboring planes in single-crystal graphite are shifted with respect to each other and form the ABAB order, whereas the nanocrystallites, in which the planes are positioned exactly one above another, are apparently present in the amorphous-carbon films (the AAAA order). This is a form of the so-called turbostratic graphite [11]. Somewhat smaller sizes of graphite-cluster (15 Å) were observed in the DLC films obtained by electron-beam evaporation of graphite [12].

The surface of the DLC obtained by methane decomposition in a high-frequency plasma discharge was studied using an STM [13, 14]. The resolution was lower than that reported previously [6, 10] but a larger surface area was studied [13]. On the whole, the DLC surface was flat; however, nanometer-sized features in the form of hillocks 40–60 Å in size were present at the surface (Fig. 4). The existence of such special features on the surface of a number of DLC films is confirmed by studies using a scanning atomic-force microscope (AFM) [15–17]. However, DLC films also exist that do not have the aforementioned special features (for example, the films studied in [18]).

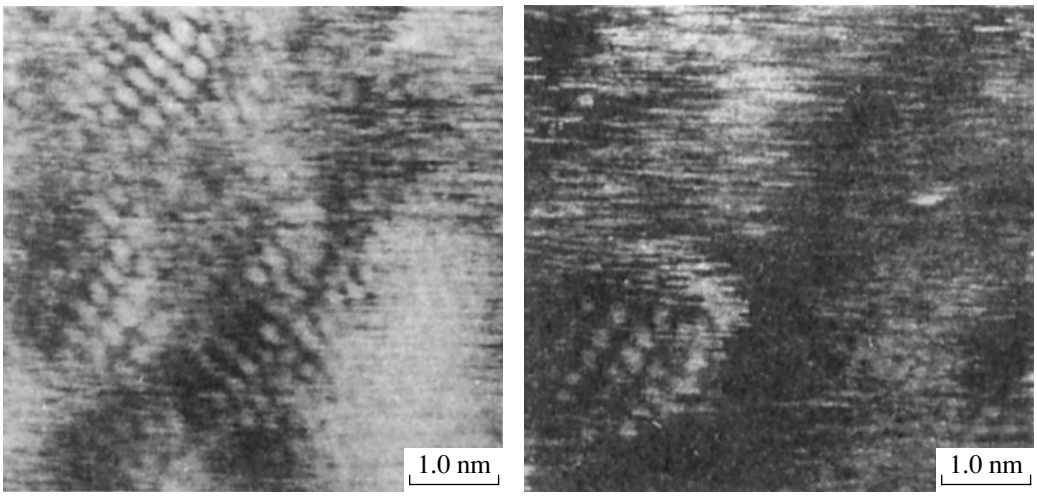

Fig. 3. The STM images of *a*-C films grown at temperatures of 450°C (the left-hand panel) and 30°C (the right-hand panel) [10].

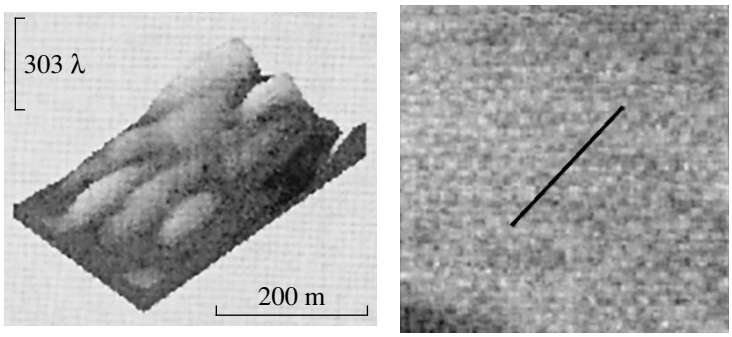

Fig. 4. The special feature of the DLC-film surface relief pattern is shown on the left; the shown surface area is 225×360 Å^2 [13]. The DLC surface without any features is shown on the right [18].

The results of STM studies of the carbon films grown by electron-beam evaporation of graphite were reported in [19]. The substrate temperature was varied in a wide range (from room temperature to 800°C). The STM images of the films grown at room temperature indicate that the film's structure is unordered. As the temperature increased, graphite nanocrystallites similar to those observed previously [9] formed. The size of the graphite domains increased with increasing temperature and attained the value of 200 Å at 800°C. The STM data are confirmed by the results of electron and Raman spectroscopies.

The influence of ion bombardment on the DLC surface relief pattern was studied using an STM in [20]. It was shown that surface irregularities as high as 15–20 nm can be smoothed to a height of 1.5–3.0 nm by bombardment with 1-keV ions of nitrogen, oxygen, and argon. This results in a significant reduction in the DLC-film friction coefficient, which is important for applications of this film as a wear-resistant coating.

The quality of STM images in relation to the film resistivity has been analyzed previously [21]. It was shown that the DLC films with the largest amount of sp^3-hybridized atoms give rise to artifacts in the STM images; these artifacts are caused by collisions of the tip with nonconducting sp^3 clusters that extend above the surface.

The attractiveness of the STM technique for studying the amorphous carbon is enhanced by the fact that the STM tip can be also used simultaneously as a tool for modifying the DLC structure. To this end, a negative voltage is applied to the tip and an electron flux from the tip modifies the film structure. An example of nanometer-scale modification of the DLC-film surface may be found elsewhere [22]. The so-called tetrahedral amorphous carbon *ta*-C:H (amorphous carbon with a content of sp^3-hybridized carbon as high as 85%) was modified [22]. It was found that it is possible to attain the stable structure variations in regions ~100 nm in size. The studies using scanning tunneling microscopy, atomic-force microscopy, and electron-loss spectroscopy showed that local graphitization (the transition to the sp^2-hybridized state) occurred in the modified region.

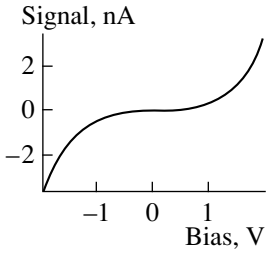

Fig. 5. A typical current–voltage characteristic of a tunneling contact between a DLC film and the STM tip [13].

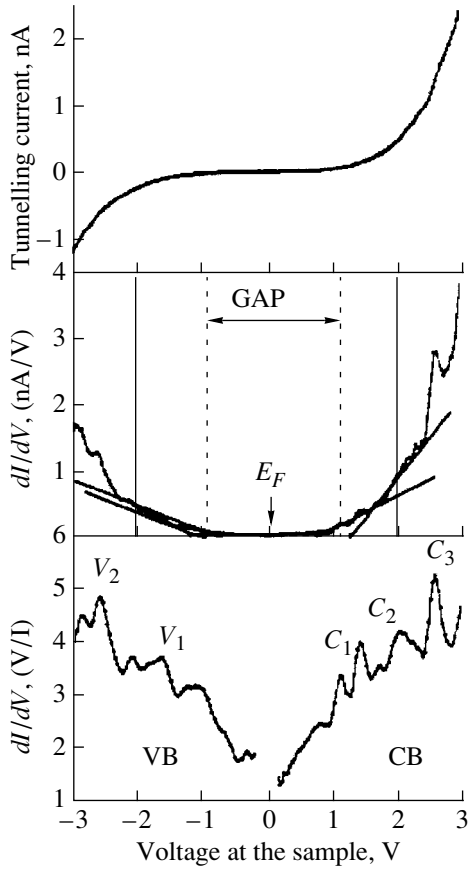

Fig. 6. Conventional (the top panel), differential (the middle panel), and normalized (the bottom panel) current–voltage characteristics of an *a*-C film grown with the ion energy of 50 eV [26].

Another example of nanometer-scale modification of the *a*-C:H surface was reported in [23]. Adsorbed trichloroethane was polymerized in an ac electric field of the STM tip. The adsorbate was transformed into a graphitized outgrowth on the film's surface. The possibility of inducing the controlled nanoscopic changes in the *a*-C and *a*-C:H films using a tunneling microscope holds much promise for applications of amorphous-carbon films in microelectronics and nanoelectronics.

3. SCANNING TUNNELING SPECTROSCOPY OF AMORPHOUS CARBON

The uniqueness of scanning tunneling spectroscopy (STS) when applied to amorphous diamond-like carbon is related to the fact that the STS makes it possible to study the local electronic structure of this material in the regions smaller than the characteristic size of the sp^2- and sp^3-hybridized clusters. However, there are a number of drawbacks inherent in the STS method. The first of these is related to the design features of a tunneling microscope. In an STM, there is a feedback loop that maintains the gap between the tip and the sample constant in the dc mode. The simplest method for obtaining the current–voltage characteristic (the tunneling spectrum) of a structure consisting of the sample, the tunneling gap, and the tip in a fixed position is to open this loop. However, with the feedback loop open, the STM tip is found in the state of unstable equilibrium [24]. Transient processes in the STM circuits at the instant the feedback loop is opened, electrostatic interaction between the tip and the substrate, and other interferences may result in uncontrolled changes in the distance between the tip and the sample. An alternative method for measuring the tunneling current consists in narrowing the passband of the STM feedback loop in such a way that the loop-response time would be longer than the voltage-modulation time (in this case the tunneling spectrum is measured in the ac mode). In addition, the modulation time should be fairly large to eliminate the contribution of the capacitive component to the total current. Methodological problems of the STS measurements performed in the atmospheric-air medium were reviewed in detail in [24].

The second disadvantage of the STS method is the difficulty of analyzing the obtained results. Depending on the conditions of measurements, the tunneling current may be proportional to either the density of electron states at the sample surface or to the corresponding convolution with the density of states in the STM tip. A detailed theory of scanning tunneling spectroscopy applied to semiconductors was developed by Y. Goldstein *et al.* [25].

The first STS studies of amorphous-carbon films were performed simultaneously with STM studies [13, 14]. The quality of the obtained spectra (Fig. 5) made it possible to estimate the band gap at the surface; however, it was impossible to determine the shape of the distribution of the local density of states.

C. Arena *et al.* [26] succeeded in obtaining higher quality spectra. The surfaces of the films of both (i) pure tetrahedral amorphous carbon with differing ratios between the amount of the sp^2- and sp^3-hybridized bonds and (ii) amorphous carbon implanted with nitrogen ions to various concentrations were studied [26]. The $[sp^2]/[sp^3]$ ratio was controlled by filtering the ion energy. The samples containing the largest fraction of sp^3 bonds (about 85%) were obtained with the ion energy of 100 eV. These samples featured the smooth

energy dependence of the density of states and a 2.55 eV band gap. Furthermore, the Fermi level was found to be somewhat closer to the top of the valence band than to the bottom of the conduction band, which indicated that the *p*-type conductivity was to a certain extent prevalent in the DLC.

As the amount of the graphite-like component increases, a number of features appear in the curve of the density of states (Fig. 6). It was especially emphasized [26] that these features were stable; they were assigned [26] to the localized π bonds with various surroundings. As would be expected, an increase in the content of the sp^2-hybridized phase causes the band gap to narrow (it was narrowed to ~1.8 eV in [26]). The dependence of the band gap on the ion energy during film growth is consistent with the optical measurement data reported in [27].

Doping of DLC with nitrogen shifts the Fermi level and narrows the band gap. In the sample with the highest nitrogen concentration, the band gap is 1.5 eV and the Fermi level is shifted by +0.25 eV with respect to the midgap (in a pure *ta*-C, this shift amounts to −0.05 eV).

The results [26] of studying the distinctions between the *ta*-C structure at the surface and in the bulk are of much interest. Two technical methods were used [26]: (I) measurements of tunneling spectrum for various distances between the tip and the surface, and (II) etching of the surface with hydrogen plasma to a depth of 15 Å. In both cases, it was found that the content of sp^3-hybridized carbon in the bulk of the carbon film is higher (and the band gap is wider) than on the surface. This result is confirmed by the fact that the shape of the tunneling spectrum for the etched film is virtually independent of the distance between the tip and the surface (Fig. 7). Thus, there is experimental verification of the subplantation model; this is one of the most popular models of DLC growth [28]. According to this model, tetrahedral bonds are formed in the near-surface layer of the growing film, and local pressure in this layer is shifted to the diamond-stability domain by the propagating ions.

Special features in the tunneling spectrum of the *ta*-C and *ta*-C:H containing up to 87% of sp^3-hybridized carbon have been reported recently [29]. These features were distinguishable both in the sp^3-hybridized clusters and at the boundaries between these clusters, but were less reproducible than those reported in [26].

An interpretation (alternative to [26]) of the features of the tunneling spectrum was suggested in [30]. The differential-conductivity peaks were related [30] to single-electron phenomena in the amorphous-carbon film itself rather than with localized π bonds. In fact, a graphite-like cluster that has small capacitance ($\leq 10^{-18}$ F), is embedded in the sp^3-hybridized medium, and is surrounded by two tunneling junctions can give rise to the effect known as the Coulomb staircase [31], and can

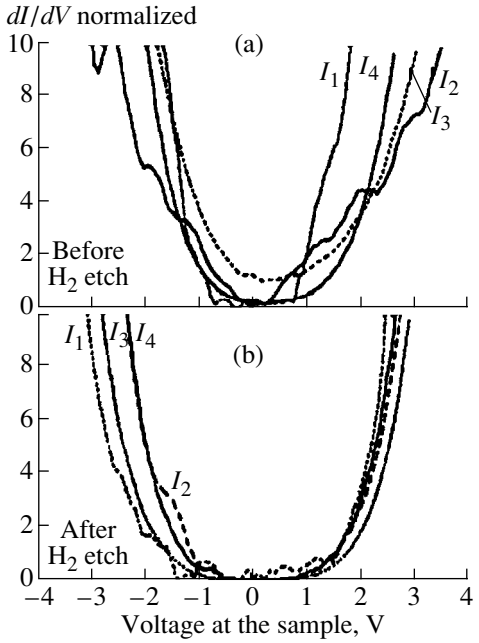

Fig. 7. A tunneling spectrum of *ta*-C (85% of sp^3-hybridized carbon); the spectrum was normalized to the value of the current under a bias of +3 V and was measured for various distances of the STM tip from the surface (a) before ion etching and (b) after etching to a depth of 15 Å [26].

generate regular spikes in differential conductivity if this cluster happens to be in the electric-current channel. This theory is corroborated by a similarity between the tunneling spectra of *ta*-C [26] and those of metal–carbon nanocomposites that contain the separate nanometer-sized metal clusters. We dwell on this specifically in Section 5.

4. STM STUDIES OF EMISSION FROM AMORPHOUS CARBON

Currently, it is difficult to overestimate the topicality of the development of industrial technology for the production of cold field emitters for flat displays. In connection with this, the discovery of a low threshold for electron emission in the films of polycrystalline diamond (even negative electron affinity was observed in this material [32]) naturally enhanced interest in the emissive properties of DLC films. The negative electron affinity and low thresholds for field emission (<30 V/μm) [33] were also observed in the films of amorphous diamond-like carbon. However, as in the case of polycrystalline diamond, the mechanism of emission is not well understood yet. The basic distinction between the DLC films and the polycrystalline-diamond films, from the standpoint of emissive properties, is related to the fact that the main potential barrier in the DLC exists at the outer surface, whereas, in diamond, this barrier is located at the surface adjacent to the rear contact [34].

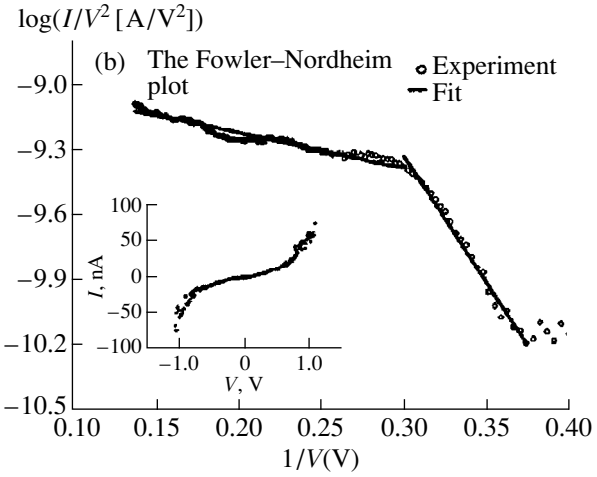

Fig. 8. The intensity of cold field emission from DLC; the emission was measured in the probe configuration, and the plot is represented in the Fowler–Nordheim coordinates [35]. The tunneling DLC spectrum is shown in the insert.

Since a DLC film has an inhomogeneous surface structure, microprobe study of the field emission with a spatial resolution comparable to the size of surface irregularities is extremely important. Such a study has been carried out previously [35]. Emission that originated in DLC films and was measured by the conventional diode method was compared with emission measured by the microprobe method; in the latter case, the STM tip is used as the anode, which makes it possible to study local emissive characteristics of the material. In the second method, the STM tip removed from the film surface to the distance that excluded tunneling was used. Preliminary AFM studies showed that clusters ~20 nm in size were present at the film surface.

The field electron emission, measured in the vacuum-diode configuration [35], set in at an electric-field strength of 13.2 V/μm, with a current density of ~160 μA/cm^2 for a field strength of 20 V/μm (the distance between the cathode and anode was 50 μm). Such values of the current density are characteristic of the emission from DLC in the diode configuration [36]. The emission was adequately described by the Fowler–Nordheim curve; the experimentally determined work function was equal to ~0.052 eV. This indicates that there is geometric enhancement of emission related to the concentration of the field around the emitting clusters. On the assumption that the true work function is equal to the value of 1.5 eV [37] characteristic of DLC, the enhancement factor α was equal to ~30. It is worth noting that, in the diode mode [38], larger values of α (as high as 10^2) were observed; however, attempts to identify the emission centers [37] using the STM/AFM methods were not successful.

In the course of the measurements in the microprobe mode, the tip was positioned at such a distance from the film that the tunneling current was not detected by the sensor for a bias voltage of 0.1 V. The field emission set in when the voltage applied to the film was equal to –2.67 V, which yields a tip–film distance of 200 nm, if the emission threshold is taken equal to 13.2 V/μm. For the applied voltage of 7 V, the emission-current density was 5 A/cm^2 (much higher than for the diode configuration). This indicates that, in the diode mode, many of the clusters are not involved in the emission process. The shape of the corresponding Fowler–Nordheim curve (Fig. 8) is also of interest. The curve could be separated into two portions that corresponded to the work functions of 1.32 and 1.86 eV. There is no explanation of this so far.

The STM studies of the field-emission centers at the DLC surface were also reported in [39]. On the basis of the results of simultaneous measurements of electrical conductivity and the surface relief pattern (the combined STM/AFM methods), it was reasoned [39] that the sp^2-hybridized clusters are the emission centers. A discrepancy with the results reported in [29] where the emission was attributed to sp^3 clusters can be apparently explained by the fact that films with a higher content of sp^2 clusters were used in [39].

5. STUDIES OF METAL–CARBON NANOCOMPOSITES BY THE SCANNING TUNNELING MICROSCOPY AND SCANNING TUNNELING SPECTROSCOPY

If an *a*-C film is doped with a metal (Me) that does not form carbides, a metal–carbon nanocomposite is formed for large metal concentrations (amounting to about 3–30 at. %). For example, the (*a*-C:H):Cu and (*a*-C:H):Pt nanocomposites are of such a type. Depending on the conditions of preparation, these composites feature a number of properties that are not inherent in the pure DLC films. These specific properties include good adhesion to almost any surface, a low level of internal stresses, resistivity in the range of 10^{14}–10^{-3} Ω cm, optical properties controlled within a wide range, etc. [40, 41].

The STM studies of an (*a*-C:H):Me nanocomposite that contained various metals (Me = Cr, W, Pd, and Pt) in addition to silicon oxide were studied previously [42, 43]. The clusters 15–25 nm in size (characteristic of DLC) can be seen in the three-dimensional STM images (Fig. 9). Annealing for 2 h at 450°C appreciably modified the film structure: large clusters became separated, and low-conductivity regions (appearing as irregularities in the STM image) emerged between the clusters. In addition, it was ascertained that the fraction of sp^2-hybridized atoms increased. In contrast, the structure of undoped DLC film that was annealed under identical conditions remained virtually unchanged. Thus, the introduction of metal reduces the thermal stability of the sp^3-hybridized matrix and diminishes the potential barrier for graphitization. By properly choosing both the initial composite composition and the

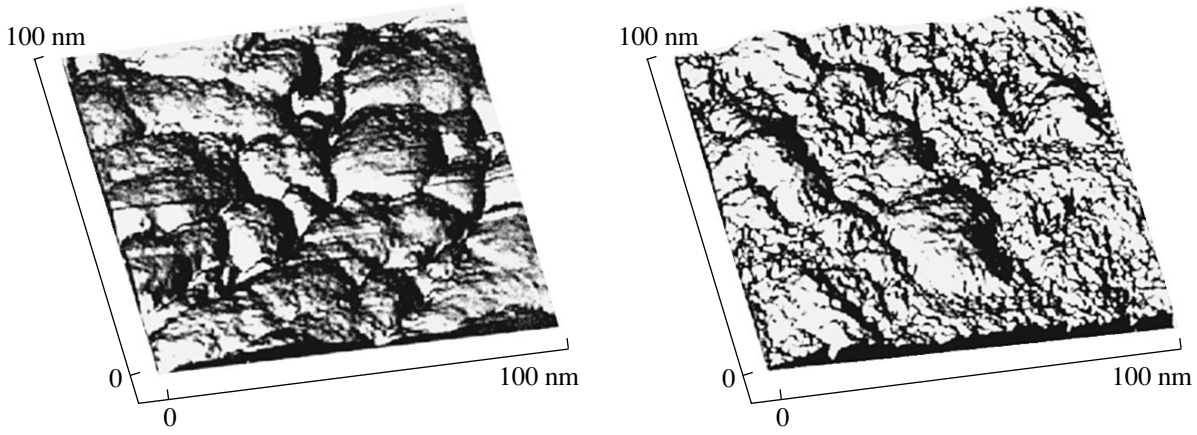

Fig. 9. An STM image of the surface of a carbon–platinum nanocomposite film before (the left-hand panel) and after (the right-hand panel) a 2-h annealing at 450°C [41].

treatment conditions, one can controllably modify the (*a*-C:H):Me structure.

The size distribution of metallic clusters in a nanocomposite was studied by K. Shiffmann *et al.* with the STM [44]. The size-distribution functions for Au and Pt clusters in amorphous hydrogenated carbon have also been derived [44]. Characteristically, the clusters were several nanometers in size. In addition, a statistical method was developed to correct the distortions related to the finiteness of the size of the STM tip and to inhomogeneous electrical conductivity of the composite film [44].

The combined STM/STS studies of an (*a*-C:H):Cu nanocomposite were reported elsewhere [18, 44]. The film surface was covered with clusters ~20 nm in size, and the magnitude of the surface roughness was no larger than 10–15 nm. The tunneling spectrum [18] indicated that the dominant electrical conductivity changed from *p*- to *n*-type when 9 at. % of Cu was introduced. Thus the metal acts as a donor of electrons for the carbon matrix. The tunneling spectrum has been studied in more detail in [45]. Oscillations of differential tunneling conductivity were observed in this spectrum (Fig. 10). These oscillations were related [45] to single-electron phenomena that occurred in localized copper clusters. An estimation of the cluster size from the width of the tunneling-current step yields ~4 nm; this is somewhat smaller than the characteristic copper-cluster size. This may be explained by the fact that the most pronounced single-electron effect originates from the smallest isolated clusters which happen to be in the current-flowing channel. Thus, the question as to interpreting the tunneling spectra for the metal–carbon nanocomposites and the *a*-C:H spectra that exhibit similar features remains open at present.

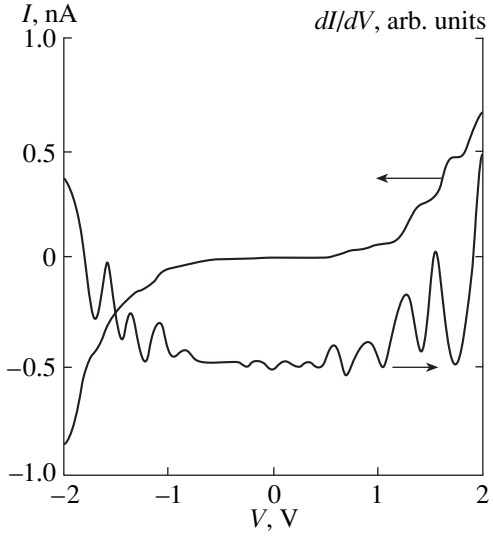

Fig. 10. A current–voltage characteristic $I(V)$ and the first derivative dI/dV for an *a*-C:H film that was doped with Cu (9 at. %) and was 100 nm thick [44].

6. CONCLUSION

A large body of data on amorphous carbon studied by the scanning tunneling microscopy and scanning tunneling spectroscopy has been obtained. On the basis of these data, the models of the structure and cold field emission have been developed for this material. Serious problems with interpretation of the STM/STS data still exist; however, there have been attempts to solve these problems. The development of the STM/STS methodology for studies of amorphous-carbon films may also bring substantial benefits to studies of other materials, especially unordered semiconductors.

ACKNOWLEDGMENTS

This review was supported by the Russian Foundation for Basic Research, project no. 00-02-17004.

All of the figures were reproduced with the consent and permission of the authors of the publications and the corresponding publishers. We thank M.B. Salmeron, J.W. Ager, E. Ben-Jacob, J. Robertson, and T.T. Chen for making the relevant figures available.

REFERENCES

1. J. C. Angus and C. C. Hayman, Science **241**, 913 (1998).
2. A. Hart, B. S. Satyanarayana, W. I. Milne, and J. Robertson, Appl. Phys. Lett. **74** (11), 1594 (1999).
3. M.-L. Theye, V. Paret, and A. Sadki, Condens. Matter News **7** (1), 4 (1998).
4. J. Robertson and E. P. O'Reilly, Phys. Rev. B **35**, 2946 (1987).
5. V. I. Ivanov-Omskiĭ, A. B. Lodygin, A. A. Sitnikova, *et al.*, J. Chem. Vap. Deposition **5**, 198 (1997).
6. B. Marchon, M. Salmeron, and W. Siekhaus, Phys. Rev. B **39** (17), 12 907 (1989).
7. J. A. van Vechten and D. A. Keszler, Phys. Rev. B **36**, 4570 (1987).
8. A. Selloni, P. Carnevali, E. Tosatti, and C. D. Chen, Phys. Rev. B **31**, 2602 (1985).
9. R. E. Stallcup, A. F. Áviles, and J. M. Pérez, Appl. Phys. Lett. **66** (18), 2331 (1995).
10. N. H. Cho, D. K. Veirs, J. W. Ager III, *et al.*, J. Appl. Phys. **71** (5), 2243 (1992).
11. M. S. Dresselhaus, G. Dresselhaus, K. Sugihara, I. L. Spain, and H. A. Goldberg, in *Springer Series in Materials Science*, Ed. by M. Cardona (Springer-Verlag, Berlin, 1988), Vol. 5, Chap. 3.
12. J. Besold, R. Thielsch, N. Matz, *et al.*, Thin Solid Films **293** (1/2), 96 (1997).
13. I. Rusman, L. Klibanov, E. Ben-Jacob, and N. Croitoru, in *Proceedings of the Third International Conference on Applications of Diamond Films, 1995*, Ed. by A. Feldman, p. 797.
14. I. Rusman, L. Klibanov, L. Burstein, *et al.*, Thin Solid Films **287** (1/2), 36 (1996).
15. H. Park, Y.-K. Hong, J. S. Kim, *et al.*, Appl. Phys. Lett. **69** (6), 779 (1996).
16. J. M. Yanez-Limon, F. Ruíz, J. González-Hernández, *et al.*, J. Appl. Phys. **76**, 3443 (1994).
17. P. Prioli, S. I. Zanette, A. O. Caride, *et al.*, J. Vac. Sci. Technol. A **14** (4), 2351 (1996).
18. V. I. Ivanov-Omskiĭ, S. G. Yastrebov, A. O. Golubok, *et al.*, Pis'ma Zh. Tekh. Fiz. **24** (20), 28 (1998) [Tech. Phys. Lett. **24**, 800 (1998)].
19. S. Shelz, T. Richmond, P. Kania, *et al.*, Surf. Sci. **359** (1–3), 227 (1996).
20. V. L. Arbuzov, V. B. Vykhodets, I. Sh. Trakhtenberg, *et al.*, J. Phys. IV **6** (5), 185 (1996).
21. A. A. Gorbunov, S. M. Pimenov, A. A. Smolin, *et al.*, Phys. Status Solidi A **145**, 393 (1994).
22. T. W. Mercer, N. J. DiNardo, J. P. Sullivan, J. P. Friedmann, M. P. Siegal, and L. J. Martínez-Miranda, *Diamond for Electronic Applications*, Ed. by D. L. Dreifus (Materials Research Society, Pittsburg, 1996), p. 175.
23. P. N. Luskinovich, V. D. Frolov, A. E. Shavykin, *et al.*, Pis'ma Zh. Éksp. Teor. Fiz. **62** (11), 868 (1995) [JETP Lett. **62**, 881 (1995)].
24. S. Yu. Vasil'ev and A. V. Denisov, Zh. Tekh. Fiz. **70** (1), 100 (2000) [Tech. Phys. **45**, 99 (2000)].
25. Y. Goldstein, L. F. Fonseca, and F. R. Zypman, Phys. Rev. B **49** (3), 1981 (1994).
26. C. Arena, B. Kleinsorge, J. Robertson, *et al.*, J. Appl. Phys. **85** (3), 1609 (1999).
27. M. Chhowalla, J. Robertson, C. W. Chen, *et al.*, J. Appl. Phys. **81**, 139 (1997).
28. Y. Lifshitz, S. R. Kasi, and J. W. Rabalais, Phys. Rev. Lett. **62**, 1290 (1989).
29. L. K. Cheah, X. Shi, E. Liu, and B. K. Tay, J. Appl. Phys. **85** (9), 6816 (1999).
30. V. I. Ivanov-Omskiĭ, A. B. Lodygin, and S. G. Yastrebov, Pis'ma Zh. Tekh. Fiz. **25** (24), 66 (1999) [Tech. Phys. Lett. **25**, 999 (1999)].
31. D. V. Likharev and K. K. Averin, Zh. Éksp. Teor. Fiz. **90**, 733 (1986) [Sov. Phys. JETP **63**, 427 (1986)].
32. W. N. Wang, N. A. Fox, J. W. Steeds, *et al.*, J. Appl. Phys. **80** (12), 6809 (1996).
33. E. I. Givargizov, V. V. Zhirnov, and A. N. Stepanova, Appl. Surf. Sci. **87**, 24 (1995).
34. J. Robertson, *Flat Panel Display Meterials III*, Ed. by R. T. Fulks (Materials Research Society, Pittsburgh, 1997), p. 217.
35. F. Y. Chuang, C. Y. Sun, T. T. Chen, and I. N. Lin, Appl. Phys. Lett. **69** (23), 3504 (1996).
36. A. Hart, B. S. Satyanarayana, W. I. Milne, and J. Robertson, Appl. Phys. Lett. **74** (11), 1594 (1999).
37. F. Y. Chuang, C. Y. Sun, and I. N. Lin, Appl. Phys. Lett. **68**, 1666 (1996).
38. O. M. Kuttel, O. Groning, L. Nilsson, *et al.*, in *Proceedings of the 1st International Specialist Meeting on Amorphous Carbon (SMAC'97)*, Ed. by S. R. P. Silva (World Scientific, Singapore, 1998), p. 338.
39. O. Groning, O. M. Kuttel, P. Groning, and L. Schlapbach, Appl. Surf. Sci. **111**, 135 (1997).
40. V. F. Dorfman, Thin Solid Films **212**, 267 (1992).
41. V. F. Dorfman, A. Bozhko, B. N. Pypkin, *et al.*, Thin Solid Films **212**, 274 (1992).
42. B. Dorfman, M. Abraizov, F. H. Pollak, *et al.*, in *Proceedings of the Third International Conference on Applications of Diamond Films and Related Materials, Gaithersburg, 1995*, Ed. by A. Feldman *et al.*, p. 769.
43. Z. Y. Rong, M. Abraizov, B. Dorfman, *et al.*, Appl. Phys. Lett. **65** (11), 1379 (1994).
44. K. I. Shiffmann, M. Fryda, G. Goerigk, *et al.*, Ultramicroscopy **66** (3/4), 183 (1996).
45. A. O. Golubok, O. M. Gorbenko, T. K. Zvonareva, *et al.*, Fiz. Tekh. Poluprovodn. (St. Petersburg) **34** (2), 223 (2000) [Semiconductors **34**, 217 (2000)].

Translated by A. Spitsyn

Semiconductors, Vol. 34, No. 12, 2000, pp. 1363–1364. Translated from Fizika i Tekhnika Poluprovodnikov, Vol. 34, No. 12, 2000, pp. 1417–1419.

ELECTRONIC AND OPTICAL PROPERTIES OF SEMICONDUCTORS

Influence of Sn Resonance States on the Electrical Homogeneity of Bi_2Te_3 Single Crystals

M. K. Zhitinskaya*, S. A. Nemov*, T. E. Svechnikova, P. Reinshaus***, and E. Müller******

** St. Petersburg State Technical University, Politekhnicheskaya ul. 29, St. Petersburg, 195251 Russia*
*** Baĭkov Institute of Metallurgy, Russian Academy of Sciences, Leninskiĭ pr. 49, Moscow, 117334 Russia*
**** Martin Luther Universität, Halle-Wittenberg, Fachgruppe Angewandte Physik, Halle (Saale), Germany*
***** German Aerospace Center (DLR), Institute of Materials Research, D-51170 Köln, Germany*

Submitted May 25, 2000; accepted for publication June 1, 2000

Abstract—An unusually high homogeneity of electrical properties was found in Sn-doped Bi_2Te_3 single crystals. The Seebeck coefficient, which is sensitive to fluctuations in charge carrier concentration, remains unchanged even when the amount of introduced Sn impurity is increased. This fact is explained in terms of the model of resonance impurity states. © *2000 MAIK "Nauka/Interperiodica".*

1. INTRODUCTION

Bismuth telluride is known to be an efficient material for thermoelectric energy converters [1]. Studies of Sn-doped Bi_2Te_3 single crystals [2–4] have revealed a number of anomalies in the behavior of kinetic coefficients; these anomalies can be explained in terms of a model that assumes the existence of Sn resonance states against the background of the allowed valence-band spectrum. The presence of these states can exert a beneficial effect on the electrical homogeneity of crystals. This is particularly important for trigonal system crystals that exhibit a pronounced anisotropy. Under actual growth conditions, even the best single crystals of this compound contain a great amount of inhomogeneities.

The Seebeck coefficient is known to be sensitive to fluctuations in charge carrier concentration. Consequently, micro-thermoelectric power values measured at numerous points on the crystal surface can characterize the spatial distribution of the carriers. This paper presents the results of the Seebeck coefficient distribution over the surface of undoped and tin-doped Bi_2Te_3 single crystals using a hot microprobe technique.

2. SAMPLE PREPARATION AND EXPERIMENTAL PROCEDURE

Single crystals were grown by the Czochralski method with an additional liquid phase feeding from a floating crucible [5]. Since Bi_2Te_3 is a compound with complex crystal structure, special procedures were developed for choosing the growth parameters (pulling rate, seed and crucible, rotation speed, temperature gradient at the crystallization front) that provide perfect crystals. The single crystals were grown in the [1010] direction, perpendicular to the principal crystallographic *c*-axis, in a He atmosphere at a pressure of 0.5×10^5 Pa. Pure (99.9999%) Bi, Te, and Sn were used in the synthesis. The charge for crystal growth was prepared by the fusion of preliminarily synthesized Bi_2Te_3 with Sn in the required proportions. The crystals had the form of platelets ~90 mm long, ~25 mm wide, and 14–16 mm thick. The sample composition is described by the chemical formula $Bi_{2-x}Sn_xTe_3$, where $x = 0$, 0.002, 0.005, 0.007, and 0.01 (for Bi_2Te_3, $x = 0.01$ corresponds to an atomic concentration of 6×10^{19} cm^{-3}). The Sn content was determined by plasma atomic-absorption spectroscopy [5]. The effective segregation coefficient obtained from these data is $K_{\text{eff}} = 0.6$. Samples for electrical measurements were cut at a distance of 70–90 mm from the end of the ingot. The perfection of the single crystals was assessed by X-ray diffraction topography [6]. The thermoelectric-power distribution over the Bi_2Te_3:Sn sample surface was studied with a microprobe by the method described in [7]. The temperature difference of 3–5 K is used in this technique. The error in thermoelectric-power measurements was $\Delta S/S < 1\%$. The method of locally measuring the Seebeck coefficient with a hot scanning probe has been developed as a procedure for the detection and characterization of the distribution of electrically active components in V_2VI_3 semiconductor compounds. The main advantages of this method are the simplicity of measurement and high resolution.

3. EXPERIMENTAL RESULTS AND DISCUSSION

The results obtained by studying the thermoelectric power of an undoped Bi_2Te_3 single crystal are shown in Fig. 1a. It can be seen that the crystals grown are of high quality and are characterized by relatively small

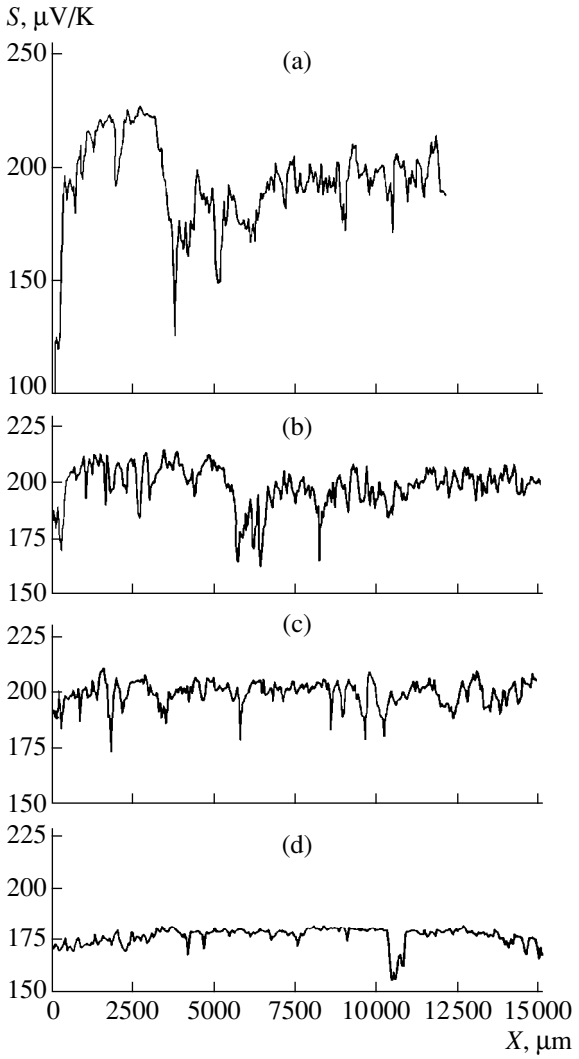

Fig. 1. Variation of the Seebeck coefficient measured across the (0001) surface along the longer sides of $Bi_{2-x}Sn_xTe_3$ single-crystal samples with Sn content x = (a) 0, (b) 0.002, (c) 0.005, and (d) 0.01.

(for bismuth telluride) fluctuations of the carrier concentration.

Usually, the introduction of doping impurities significantly enhances the thermoelectric power fluctuations, which are due to the stochastic nature of impurity distribution through the crystal. However, the reverse situation is observed for the case of Sn-doped Bi_2Te_3. With an increasing amount of the Sn impurity, the fluctuations of thermoelectric power and, correspondingly, of the hole concentration decreased significantly (see Figs. 1b–1d), thus indicating a noticeably improved electrical homogeneity of the crystals.

The unusual behavior of impurities in Sn-doped Bi_2Te_3 is readily explained by the model of resonance impurity states. Indeed, according to [4], doping of Bi_2Te_3 crystals with Sn leads to the formation of a density-of-states peak proportional to the introduced impurity concentration near the top of the additional extremum of the valence band. It may be suggested from the data regarding Bi_2Te_3:Sn doping with additional electrically active impurity [3, 4] that the resonance states are partially filled with electrons. In addition, no noticeable dependence of the resonance-state peak position on the Sn impurity concentration was observed. The existence of such a peak in the density of states, partially filled with electrons, leads to pinning of the hole Fermi level.

Introduction of additional impurities or formation of electrically active intrinsic donor- or acceptor-type defects in the crystal lattice in concentrations lower than that of the introduced Sn do not lead to any noticeable shift of the Fermi level. The Fermi level is only shifted in the vicinity of the density-of-states peak whose width is on the order of several hundredths of an electronvolt (~0.02–0.03 eV) [4].

With an increase in Sn content (for $N_{Sn} > 0.5$ at. %), only the height of the density-of-states peak grows, and the Fermi level remains pinned at this peak. The Bi_2Te_3 composition fluctuations and variation in the concentration of different types of defects inherent in this material shift the Fermi level only slightly, since the defect concentration is relatively low compared with the number of introduced Sn atoms. It is this effect that determines the high spatial homogeneity of the electrical properties of the crystals under study.

4. CONCLUSION

We identified an impurity that noticeably improves the spatial homogeneity of the electrical properties of Bi_2Te_3 single crystals.

REFERENCES

1. V. A. Semenyuk, T. E. Svechnikova, and L. D. Ivanova, Adv. Mater. **5**, 428 (1994).
2. V. A. Kulbachinskii, N. B. Brandt, P. A. Cheremnykh, *et al.*, Phys. Status Solidi B **150**, 237 (1988).
3. G. T. Alekseeva, P. P. Konstantinov, V. A. Kutasov, *et al.*, Fiz. Tverd. Tela (St. Petersburg) **38**, 2998 (1996) [Phys. Solid State **38**, 1639 (1996)].
4. M. K. Zhitinskaya, S. A. Nemov, and T. E. Svechnikova, Fiz. Tverd. Tela (St. Petersburg) **40**, 1428 (1998) [Phys. Solid State **40**, 1297 (1998)].
5. T. E. Svechnikova, S. N. Chizhevskaya, and N. M. Maksimova, Neorg. Mater. **30**, 161 (1994).
6. T. E. Svechnikova, I. D. Ivanova, and S. N. Chizhevskaya, *Doped Semiconducting Materials*, Ed. by V. S. Zemskow (Nova Science, New York, 1993), p. 247.
7. P. Reinchaus, H. Sussmann, M. Bohm, *et al.*, in *Proceedings of the 2nd Symposium on Thermoelectric Materials, Proc. Techniques and Applications, Dresden, 1994*, p. 90.

Translated by D. Mashovets

Semiconductors, Vol. 34, No. 12, 2000, pp. 1365–1369. Translated from Fizika i Tekhnika Poluprovodnikov, Vol. 34, No. 12, 2000, pp. 1420–1425.

ELECTRONIC AND OPTICAL PROPERTIES OF SEMICONDUCTORS

The In/PbTe Barrier Structures with a Thin Intermediate Insulating Layer

O. A. Aleksandrova*, A. T. Akhmedzhanov*, R. Ts. Bondokov*, V. A. Moshnikov*, I. V. Saunin*, Yu. M. Tairov*, V. I. Shtanov, and L. V. Yashina****

** Ul'yanov (Lenin) University of Electrical Engineering, St. Petersburg, 197376 Russia*
e-mail: ME@eltech.ru
*** Moscow State University, Vorob'evy gory, Moscow, 119899 Russia*
Submitted June 1, 2000; accepted for publication June 1, 2000

Abstract—Epitaxial *n*-PbTe layers were grown on BaF_2 {111} single-crystal substrates by hot-wall epitaxy from the gaseous phase. These layers were kept in atmospheric air for 15–30 days, after which In and protective BaF_2 layers were deposited. Current–voltage characteristics and photoelectric sensitivity spectra of the In/*n*-PbTe barrier structures were measured in the temperature range T = 80–300 K. Based on the experimental results, a model of charge transport is suggested and the effective barrier height φ_b^{eff}, the insulator layer thickness δ, and the surface-state density D_S are determined. © *2000 MAIK "Nauka/Interperiodica".*

INTRODUCTION

Metal–lead-chalcogenide structures hold much promise for the application to near and medium infrared (IR) photodetectors and have been studied intensively for the last 30 years [1]. By now, a large body of experimental current–voltage characteristics and photoelectric spectra have been accumulated, yet no model exists that accounts for these data.

Most experimental data are interpreted in terms of the simplest models of classical barriers suggested by Schottky and Bardeen. These models disregard the diffusion of dopants and lattice defects, as well as the oxidation of the surface layers. However, these processes can considerably affect the surface-state density at interfaces and also other characteristics due to the formation of new phases or inversion of conductivity type in the surface layer [2, 3]. The dependences of current–voltage and other electrical characteristics of metal–semiconductor barriers on insulator thickness and surface-state density were studied in [4]. Oxide phase formation at the metal–semiconductor interface and the chemical interaction of indium with lead chalcogenides were observed in [5, 6]. The models accounting for the physical properties of metal–semiconductor structures with thin insulators were systematized in [7]. Considering the structures based on lead chalcogenides, the possible formation of an inversion layer in the *n*-region due to oxygen diffusion, as observed in [8] with *n*-PbSe, should be taken into account. A higher electronegativity of tellurium enables the formation of inversion *p*-type layer on the *n*-PbTe surface even at room temperature [9]. The composition of the oxide layer (PbO and TeO_2) varies for the structures that are kept in air for different periods of time [10]. The above-mentioned features of metal–lead-chalcogenide structures account for the fact that their current–voltage and photoelectric characteristics critically depend on the technology of fabrication.

In this paper, we report the results of studying the effect of an intermediate insulator and inversion layers on the characteristics of In/*n*-PbTe structures.

EXPERIMENTAL

The epitaxial layers of lead telluride were grown from the gaseous phase by hot-wall epitaxy described in detail elsewhere [11]. A freshly cleaved BaF_2 single crystal was used as a substrate. The condensation rate was 2.7 μm/h at the substrate temperature between 600 and 630 K. The charge was preannealed under conditions minimizing the total vapor pressure [12]. In thus-prepared *n*-PbTe layers, the electron mobility was 640 $cm^2/(V\ s)$ at 300 K and 850 $cm^2/(V\ s)$ at 80 K. The carrier density was 5×10^{17} cm^{-3}. At the next stage, bismuth, lead, or indium was evaporated through a mask on the *n*-PbTe surface. The resulting (Bi, Pb, In)/*n*-PbTe structures qualitatively had the same current–voltage

Parameters of In/*n*-PbTe structures at T = 80 K

Structure type	φ_b^{eff}, eV	n_0	δ, nm	R_0A, $\Omega\ cm^2$	S_{max}, V/W
1	0.114	1.29	44.9	4.2	1
2	0.121	2.61	59.3	22.8	47
3	0.134	4.58	70.5	64.2	256

Note: n_0 is an ideality factor of current–voltage characteristic.

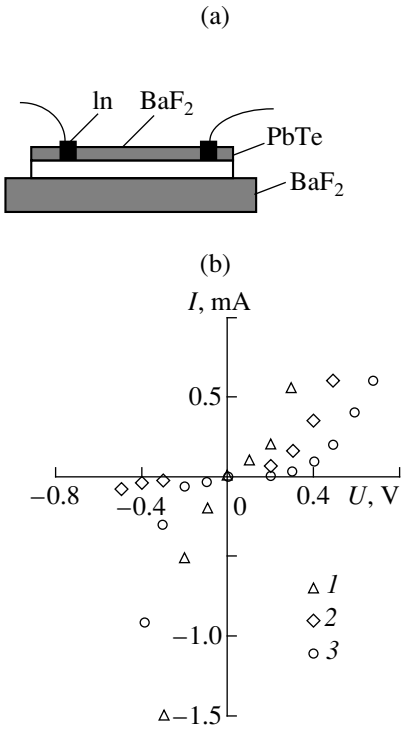

Fig. 1. (a) Cross section of a typical In/*n*-PbTe structure; (b) current–voltage characteristics of the studied structures kept in air for (*1*) 15 min, (*2*) 360 h, and (*3*) 720 h at $T = 80$ K.

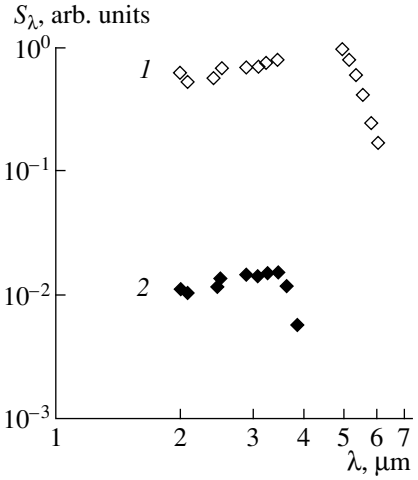

Fig. 2. Photosensitivity spectra of In/*n*-PbTe structure (kept in air for 360 h) measured at (*1*) 80 and (*2*) 300 K.

characteristics; specifically, they were linear at room temperature and cooling gave rise to a barrier.

We have studied in detail the current–voltage and photoelectric characteristics of the In/*n*-PbTe structures that are schematically shown in Fig. 1a. All of the *n*-type PbTe layers were grown by using a single procedure. The grown layers were kept in air for varying periods of time (from 15 min to 1 month) at room temperature. The structures were finished with the deposition of indium and protective BaF_2 layers. It was found that the duration of air exposure affected the current–voltage characteristics considerably. Figure 1b shows the current–voltage characteristics of the typical structures of *n*-PbTe with different durations of *n*-BbTe air exposure before indium deposition. Henceforth (see table), we use the indices *1*, *2*, and *3* for parameters of the structures exposed to air for $t_1 = 15$ min, $t_2 \simeq 360$ h, and $t_3 \simeq 720$ h, respectively. Differential resistance of these structures at room temperature was $R_1 = 50\ \Omega$, $R_2 = 70\ \Omega$, and $R_3 = 90\ \Omega$. For all of the studied structures, the reverse current–voltage characteristics lack saturation.

Photoelectric characteristics were measured in open-circuit photovoltage mode. The voltage photosensitivities S_λ differ considerably for the three types of structures. The largest values of S_λ at 4.83 μm and R_0A are listed in the table. The photosensitivity spectra of the structure of type 2 are plotted in Fig. 2 for $T = 80$ and 300 K. The detectivity calculated for the structures of the type 3 indicates that these structures can operate in the mode of detectivity limited by fluctuations of background light (the BLIP mode).

RESULTS AND DISCUSSION

To interpret the results obtained in the experiment, let us consider an energy diagram of a metal–semiconductor junction with a thin insulating layer formed as the result of surface oxidation (Fig. 3a). Since the diffusion of oxygen in the In/*n*-PbTe structure leads to formation of the surface inversion layer *p*-PbTe, the possible formation of In/δ-layer/*p*-PbTe/*n*-PbTe structure should be taken into account (Fig. 3b). In Fig. 3, the following designations are used: $q\varphi_M$ is the work function for the metal; φ_b is the potential barrier height; φ_{b0} is the asymptotic value of φ_b at zero bias; φ_0 is the level corresponding to electric neutrality; ΔU_δ is the voltage drop at the insulator; δ is the insulator thickness; $\Delta\varphi$ is the lowering of the induced barrier by image forces; χ is the electron affinity of the semiconductor; D_S is the surface-state charge density; E_F is the Fermi level; and ε_D and ε_S are the permittivities of the insulator and semiconductor, respectively.

The role of the insulator and the inversion layers at the In/*n*-PbTe interface can be assessed from analysis of the current–voltage and photoelectric characteristics. In all calculations, the insulator layer δ was considered to be tunneling-transparent; i.e., a fraction of applied voltage ΔU_δ dropped across this layer. The condition for the diode-theory applicability is the Bethe criterion: $l \gg d$, where l is the mean free path, and $d = kT/qE_{max}$ denotes the distance across which the barrier height decreases by kT/q [2]. We estimated l as

$$l = \mu(3nh^3/8\pi q^3)^{1/3} \simeq 34\ \text{nm}.$$

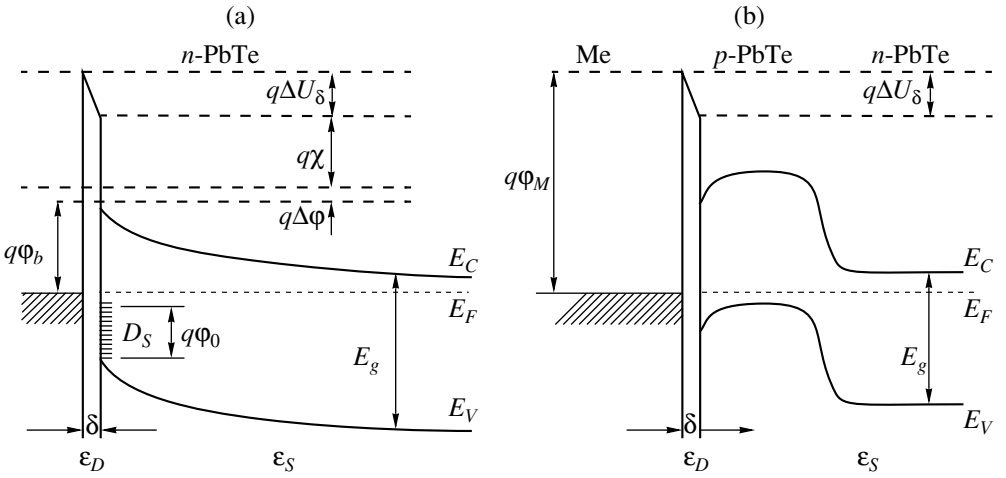

Fig. 3. Energy diagram of In/*n*-PbTe structure (a) with insulator and (b) in case of *p*-PbTe inversion-layer formation.

The maximum electric field within the barrier region was determined to be

$$E_{\max} = [2qN_D(\varphi_b - U - E_F)/\varepsilon_S]^{1/2}.$$

Here, k is the Boltzmann constant, T is temperature, q is the elementary charge, $E_{\max}$ is the maximum electric-field strength in the Schottky barrier, μ is the charge-carrier mobility, n is the electron concentration, N_D is the donor concentration, U is the applied voltage, and φ_b is the Schottky barrier height with respect to the Fermi level in the metal. From the above formulas, it follows that the maximum $d \simeq 3.5$ nm $< l \simeq 34$ nm and the application of the diode theory to In/*n*-PbTe structure is justified.

Among the different current components contributing to the charge transport across the indium–lead-telluride interface, thermionic emission over the barrier was dominant. Another important mechanism is the carrier recombination due to hole injection in the neutral region. Tunneling through the junction and recombination in the space charge region can be disregarded.

In this approximation, the current–voltage characteristic can be expressed by

$$J = J_0 \exp(qU/kT - 1),$$

where

$$J_0 = A^*T^2 \exp(-q\varphi_b/kT),$$

$$A^* = (4\pi m^* qk^2/h^3)$$

is the Richardson constant for thermionic emission and m^* is the effective electron mass.

Generally, the barrier height φ_b is a function of the bias voltage U and image forces $\Delta\varphi$; therefore, the measurements of current–voltage characteristics yield an effective value of barrier height φ_b^{eff}. The same conclusion is suggested by the complex structure of the In/*n*-PbTe interface. In this study, a decrease in the barrier height caused by image forces $\Delta\varphi$ was disregarded because of its negligibly small value. By extrapolating the current–voltage characteristics to zero bias, we determined the barrier height at zero bias $\varphi_{b0} \simeq \varphi_b^{\text{eff}}$ and the ideality factor n_0. The values corresponding to the structures of the three selected types are listed in the table. The effective barrier height φ_b^{eff} obtained in this study agrees well with the results reported in [13], where φ_b^{eff} determined for In/*p*-$Pb_{1-x}Sn_xTe$ amounted to 0.09 eV.

The table also shows the estimated layer thickness δ calculated by the numerically solving the system of two nonlinear transcendental equations $\varphi_b^{\text{eff}} = f(U)$ and $n_0 = f(U)$ by Newton's method using Microsoft Excel 7.0 software. The surface-state density D_S was found to be 10^{16} eV^{-1} m^{-2}. This value is calculated on the assumption of closeness of the neutrality level φ_0 to the Fermi level that coincides with the bottom of the *n*-PbTe conduction band. Permittivity ε_D is taken equal to $40\varepsilon_0$, which corresponds to ε_D in PbO [14].

The hole injection factor was calculated as

$$\gamma_p = J_p/(J_p + J_n),$$

where J_n and J_p are the electron and hole current densities, respectively. For the all types of the structures, the injection factor was close to unity. This is attributed to the formation of an inversion layer, which can provide for an effective hole injection into the neutral region. We account for the inversion layer by introducing an additional resistance R that depends on the voltage bias U and is connected in series. An increase in the bias voltage leads to a decrease in R according to the formula

$$R\ [\text{k}\Omega] = 48.9 \exp(-6.1U\ [\text{V}]),$$

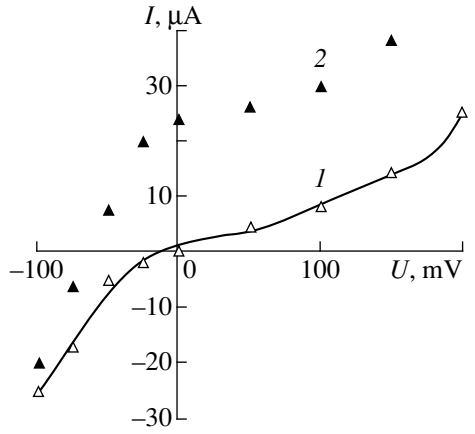

Fig. 4. Current–voltage characteristics of In/*n*-PbTe structures exposed to air for 360 h, measured (*1*) in the dark and (*2*) under illumination.

which results from the approximation of the experimental current–voltage characteristic by the expression

$$I = I_0 \exp[(U - IR)/kT],$$

where I_0 is the saturation current obtained in the experiment. Using R as an adjustable parameter, we managed to fit the experimental curves with an accuracy of $\Delta I = 5 \times 10^{-4}$ mA.

The partial voltage drop ΔU_δ at the tunneling insulating layer δ is one of the main reasons why an insulator can affect the current–voltage characteristics. As far as the photoelectric properties are concerned, the special role of insulator is related to the surface-state density D_S, since a decrease in D_S causes an increase in photosensitivity S_λ [13].

According to the data listed in the table, S_λ increases with insulator layer thickness δ. However, in spite of satisfactory photoelectric characteristics, these structures still have a high surface-state density D_S. In this case, the barrier height is governed by the surface states and approaches the Bardeen limit [2]

$$q\varphi_b \approx E_g - q\varphi_0,$$

where E_g is the semiconductor band gap and φ_0 is the highest level at which the surface states are still occupied (or, the electroneutrality level). Such a barrier can exist for the obtained values of $\delta \simeq 60$–70 nm and $D_S = 10^{16}$ eV^{-1} m^{-2}. Since surface-state density is determined by surface properties alone, a weak dependence of the current–voltage characteristic on the deposited metal (Bi, Pb, In) is easily understood.

Large values of D_S can be caused both by classical surface states and the states associated with chemisorbed molecules of oxygen. As an oxidant, oxygen draws electrons from the bulk of the semiconductor and thus forms additional current channels on the surface [15]. The PbTe surface is then rapidly covered with oxygen [9]. Recall that the samples of type 1 were kept in air for 15 min. During this period of time, formation of the insulator layer is unlikely. Within this time, however, chemisorbing oxygen can invert the PbTe surface layer, even under the protective BaF_2 film. This is the reason why both a barrier and an appreciable photovoltage are observed in In/*n*-PbTe structures. Illumination of a sample causes sign inversion for the open-circuit voltage U_{oc} and for the short-circuit current I_{sc} (see Fig. 4), which points to the surface *p*–*n* junction as the main contributor to photovoltage generation.

A voltage drop across the insulator layer ΔU_δ results in the barrier height at zero bias φ_{b0} being lower than that for an ideal diode [3]. As the layer thickness δ increases, the barrier height φ_b should decrease. However, this contradicts the experimental evidence (see table). The value measured in the experiment φ_b^{eff} is actually the difference between the heights of the *p*–*n* junction barrier and the In/*n*-PbTe contact barrier φ_b (Fig. 3b). As the duration of air exposure of the structure increases, the *p*-region becomes thicker and the contribution from the junction barrier grows.

A consequence of the increase in insulator thickness δ should be a decrease in the current for the same forward bias. This is understandable, since electrons must pass through the barrier formed in the insulating layer, since this is observed in the experiment. The same effect causes the ideality factor n_0 to increase with increasing thickness δ, which is also consistent with the experimental data (see table). The obtained n_0 values are anomalously large, and the dependence of $\ln J$ on the bias U is nonlinear. These results can be attributed to the presence of a fairly thick insulating layer or to recombination in the space-charge region. Analysis of the current-flow mechanisms shows that recombination may be disregarded in In/*n*-PbTe structures. Consequently, the n_0 values ranging from 1.3 to 4.6 can be associated with the insulating layer ($\delta \approx 70$ nm).

Another effect of the insulating layer is an increase in the minority-carrier injection factor at forward bias. According to [2], an increase in the insulator thickness can enhance the injection factor γ to 0.1 at most. In this study, with In/*n*-PbTe, we have $\gamma \approx 1$. Such a large factor of minority-carrier injection can be a result of *p*–*n* junction formation in the surface layer.

Several mechanisms can account for the lack of saturation current at a reverse bias. The tunneling insulator layer provides for a decrease in the effective barrier height φ_b^{eff} with increasing bias U. The resulting increase in current can compensate (for a thin barrier) for an increase in current associated with tunneling through the barrier formed by an insulator. As a result of inversion-layer formation, two opposing-junctions appear. It is seen from Fig. 3b that a forward bias for In/*n*-PbTe is a reverse bias for the other *p*–*n* junction.

CONCLUSION

The analysis of the current–voltage and photoelectric characteristics of In/*n*-PbTe structures with different durations of exposure to air showed that the interface insulating layer accounts for the following: (1) a similarity in current–voltage characteristics for all types of metals used; (2) the effective barrier height at zero bias is lower than that of an ideal *p–n* junction; (3) an increase in air exposure leads to a decrease in the current at constant bias and an increase in the current–voltage-characteristic ideality factor; (4) the barrier height depends on bias; and (5) the reverse portions of the current–voltage characteristics do not exhibit saturation.

On the other hand, the presence of the *p–n* junction in the surface layer results in the following: (1) the barrier height grows with increasing duration of air exposure; (2) barrier effects manifest themselves even in the structures exposed to air for a short time, when the formation of the insulating layer is unlikely; (3) the hole-injection factor is calculated to be close to unity; (4) the reverse portions of the current–voltage characteristics do not exhibit saturation; and (5) with illumination, sign inversion of the open-circuit voltage is observed.

ACKNOWLEDGMENTS

This study is supported by the Russian Foundation for Basic Research, project no. 97-03-33334a.

REFERENCES

1. N. N. Berchenko, D. Sh. Zaridze, and A. V. Matveenko, Zarubezh. Élektron. Tekh., No. 4, 34 (1979).
2. E. H. Rhoderick, *Metal-Semiconductor Contacts* (Clarendon, Oxford, 1988, 2nd ed.; Radio i Svyaz', Moscow, 1982).
3. *Thin Films: Interdiffusion and Reactions*, Ed. by J. M. Poate, K. Tu, and J. Meier (Wiley, New York, 1978; Mir, Moscow, 1982).
4. V. I. Strikha, E. V. Buzaneva, and I. A. Radzievskiĭ, in *Semiconductor Devices with Schottky Barriers (Physics, Technology, Application)*, Ed. by V. I. Strikha (Sov. Radio, Moscow, 1974).
5. T. A. Grishina, I. A. Drabkin, Yu. P. Kostikov, *et al.*, Izv. Akad. Nauk SSSR, Neorg. Mater. **18** (10), 1709 (1982).
6. T. A. Grishina, I. A. Drabkin, Yu. P. Kostikov, *et al.*, Izv. Akad. Nauk SSSR, Neorg. Mater. **23** (11), 1839 (1987).
7. E. V. Buzaneva, *Microstructures of Integrated Electronics* (Radio i Svyaz', Moscow, 1990).
8. V. T. Trofimov, Yu. G. Selivanov, and E. G. Chizhevskiĭ, Fiz. Tekh. Poluprovodn. (St. Petersburg) **30**, 755 (1996) [Semiconductors **30**, 405 (1996)].
9. A. L. Hagstrom and A. Fahlman, Appl. Surf. Sci. **1**, 455 (1978).
10. R. Bettini and H. J. Richter, Surf. Sci. **80**, 334 (1979).
11. O. A. Aleksandrova, R. Ts. Bondokov, I. V. Saunin, and Yu. M. Tairov, Fiz. Tekh. Poluprovodn. (St. Petersburg) **32**, 1064 (1998) [Semiconductors **32**, 953 (1998)].
12. V. P. Zlomanov and A. V. Novoselova, *The P–T–x Diagrams for Metal-Chalogen Systems* (Nauka, Moscow, 1987).
13. T. A. Grishina, N. N. Berchenko, G. I. Goderdziashvili, *et al.*, Zh. Tekh. Fiz. **57**, 2355 (1987) [Sov. Phys. Tech. Phys. **32**, 1424 (1987)].
14. G. A. Bordovskiĭ and V. A. Izvozchikov, *Naturally Unordered Semiconductor Crystal* (Obrazovanie, St. Petersburg, 1997).
15. R. Tz. Bondokov, D. Tz. Dimitrov, V. A. Moshnikov, *et al.*, in *Proceedings of the 5th International Conference on Material Science and Material Properties for Infrared Optoelectronics, Kiev*, Proc. SPIE **3890**, 241 (1999).

Translated by A. Sidorova-Biryukova

Semiconductors, Vol. 34, No. 12, 2000, pp. 1370–1375. Translated from Fizika i Tekhnika Poluprovodnikov, Vol. 34, No. 12, 2000, pp. 1426–1431.

ELECTRONIC AND OPTICAL PROPERTIES OF SEMICONDUCTORS

The Formation Kinetics of a Strongly Absorbing State in a Bistable Excitonic Noncavity System

Yu. V. Gudyma

Fed'kovich State University, ul. Kotsyubinskogo 2, Chernovtsy, 58012 Ukraine

Submitted July 23, 1999; accepted for publication June 18, 2000

Abstract—A unified approach allowing the description of all formation stages of a strongly absorbing state in a bistable excitonic noncavity system as a nonequilibrium first-order phase transition is proposed. In the fast-switching-wave approximation, the switching-wave front velocity is determined, and the thickness of the phase discontinuity interface is estimated. The size distributions of subcritical and supercritical nuclei and an asymptotic expression for the nucleus radius are obtained. © *2000 MAIK "Nauka/Interperiodica".*

1. INTRODUCTION

The presence of an external or internal feedback and a nonlinear intensity dependence of the light-absorption coefficient at the exciton resonance frequency give rise to the luminous-flux self-action effect. This means that laser radiation passing through the medium is a multivalued function of the incident-light intensity [1]. A nonlinear mechanism of the optical bistability in exciton transition can be related to the renormalization of the band gap or to the screening of exciton states by high-density electron–hole plasma (noncavity bistability), and also to the two-photon generation of biexcitons (Fabry–Pérot resonators are necessary in this case). It is important that optical nonlinear effects occur in a resonance formation of excitons at a significantly lower incident-light intensity, compared with excitation of isolated atoms. Therefore, the experimental observation of the noncavity optical bistability in the exciton-resonance range at a relatively low exciton density ($n_{ex} \approx 10^{15}$ cm^{-3}) and intensity of 1 kW/cm^2 at room temperature [2, 3] opened up fresh opportunities for the development of practical optical devices [4, 5]. Despite the intensive studies of this effect in recent decades, the problem of the noncavity optical bistability in the resonance generation of excitons remains topical [6, 7]. A detailed study of the kinetics of optical bistability as a nonequilibrium phase transition is undoubtedly one of the fundamental tasks in this line of research; some of its aspects are considered in this paper.

2. BASIC EQUATIONS

Let us assume that the surface $z = 0$ of a semiconductor wafer is illuminated with a broad, laterally inhomogeneous light beam of intensity $I_0(x, y)$. The wafer has the thickness l. Transport equations for the laser radiation with the intensity $I(z)$ and quasiparticle density $n(x, y, z, t)$ can be written in the form [8, 9]

$$\frac{\partial I}{\partial z} = -\alpha(\omega, n)I(z), \tag{1}$$

$$\frac{\partial n}{\partial t} = D_\perp\left(\frac{\partial^2 n}{\partial x^2} + \frac{\partial^2 n}{\partial y^2}\right) - D_z\frac{\partial^2 n}{\partial z^2} + \alpha(\omega, n)I(z) - \frac{n}{\tau}, \tag{2}$$

where $\alpha(\omega, n)$, $D_\perp$, and D_z are the light absorption and quasiparticle diffusion coefficients (in-plane and across the plate thickness), respectively, and τ is the quasiparticle lifetime.

The frequency dependence of the light-absorption coefficient $\alpha(\omega, n)$ in the case of resonance light absorption is given by

$$\alpha(\omega, n) = \alpha_0\left[1 + \left(\frac{\omega_r' - \omega}{\Delta\omega}\right)^2\right]^{-1}. \tag{3}$$

Collective interactions in the exciton system at high excitation level cause the resonance frequency ω_r' to become a function of the excitation density, decreasing with n: $\omega_r' = \omega_r - an$. In other words, the exciton level approaches the electron–hole pair continuum spectrum and the exciton binding energy decreases. The reason is that the ground state energy per electron–hole pair in the electron–hole plasma decreases and the semiconductor band gap becomes effectively narrower at concentrations $n_{ex}a_{ex} < 1$. In our case, $\Delta\omega$ and an are, respectively, the width and shift (in an approximation linear in particle concentration) of the exciton level ω_r.

Assuming that the diffusion length exceeds the wafer thickness and introducing a light intensity aver-

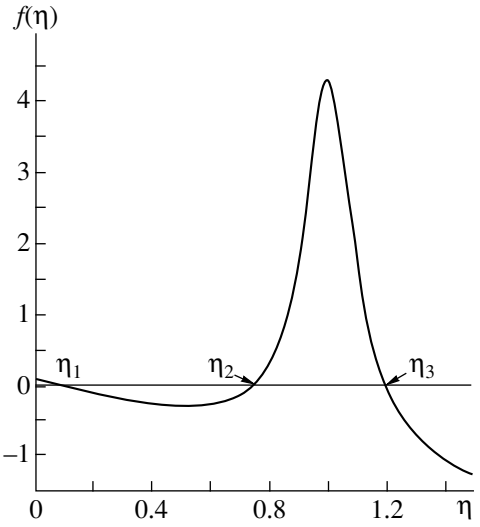

Fig. 1. Shape of the function $f(\eta)$ for fixed parameters $\beta = 99$, $\lambda = 0.055$, and $\Omega = 100$.

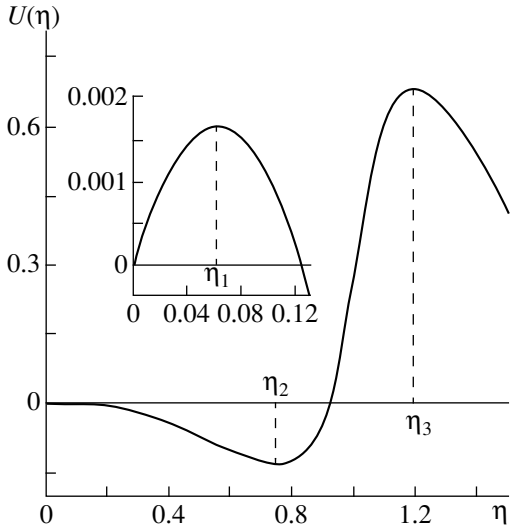

Fig. 2. The force function (6) in relation to the phase variable η ($\beta = 99$, $\lambda = 0.055$, and $\Omega = 100$).

aged over the wafer thickness, we obtain a nonlinear concentration balance equation

$$\frac{dn}{dt} = D_\perp\left(\frac{\partial^2 n}{\partial x^2} + \frac{\partial^2 n}{\partial y^2}\right) + I_0 l^{-1}\{1 - \exp[-\alpha(\omega, n)l]\} - \frac{n}{\tau}. \quad (4)$$

Maintaining a fixed incident light frequency, we can pass to dimensionless variables in Eq. (4):

$$\frac{d\eta}{d\theta} = \frac{\partial^2 \eta}{\partial \bar{x}^2} + \frac{\partial^2 \eta}{\partial \bar{y}^2} + \beta\left\{1 - \exp\left[-\frac{\lambda}{1 + \Omega(1-\eta)^2}\right]\right\} - \eta \equiv \frac{\partial^2 \eta}{\partial r_\perp^2} + f(\eta), \quad (5)$$

where $\theta = t/\tau$, $\lambda = \alpha_0 l$,

$$\Omega = \left(\frac{\omega_r - \omega}{\Delta\omega}\right)^2, \quad \eta = an/(\omega_r - \omega),$$

$$\beta = \alpha\tau I_0(\omega_r - \omega)^{-1} l^{-1},$$

$$\frac{\partial^2}{\partial r_\perp^2} = \frac{\partial^2}{\partial \bar{x}^2} + \frac{\partial^2}{\partial \bar{y}^2}, \quad \bar{x} = x/(D_\perp\tau)^{1/2},$$

$$\bar{y} = y/(D_\perp\tau)^{1/2}.$$

Let us consider time-independent axially symmetric solutions to Eq. (5), which may be from one to three in number, depending on the control parameter value (Fig. 1). In the last case, the system has two stable stationary homogeneous states (weakly and strongly absorbing) with characteristic exciton densities η_1 and η_3, and an unstable state with intermediate density η_2. This leads to a hysteresis in the quasiparticle distribution; the hysteresis is determined by the laser-radiation intensity. This bistability scenario can be classified as purely optical, absorptive, with an internal feedback. Physically, a phase can be ascribed to any stable state, whereas a transition point can be assigned to an unstable state, which makes it possible to invoke ideas developed in the phase transition theory. Below the transition point, the weakly absorbing state η_1 is stable, and the strongly absorbing state η_3 is metastable; the reverse situation is observed above this point.

3. MECHANICAL APPROACH TO THE PROBLEM

It suffices to know the shape of the function

$$U(\eta) = \int_0^\eta f(u)du \quad (6)$$

for a qualitative investigation of Eq. (5). The force function (see Fig. 2) (6) determines the phase portrait that represents all the possible states of the system (Fig. 3). As can be seen from Fig. 3, two main kinds of phase trajectories for Eq. (5) are important in the domain under study. Type-1 trajectories (curves 1) correspond to solutions with a periodic spatial dependence of the density, unstable for the system in question. Type-3 trajectories (curves *3*) correspond to the free motion of particles. The thick line (*2*) represents separatrix loops whose closed portion corresponds to a limiting type-1 trajectory (limit cycle).

The main structural type characteristic of simple bistable media is the switching wave (shown by the

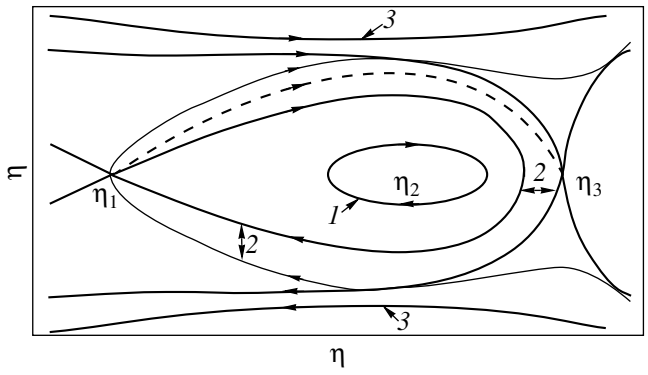

Fig. 3. Phase trajectories representing solutions to Eq. (5). Significance of curves *1–3* is explained in the text.

dashed line in Fig. 3); elements of the medium switch from one stable state to another with its passage. Since the nonlinear function $f(\eta)$ assumes large positive values in a narrow range of η values and is negative (albeit with small absolute value) in a wide range of η, the switching-wave front velocity can be defined in the fast-switching-wave approximation [8, 9] as

$$V = \frac{(2A)^{1/2}}{\eta_3 - \eta_1}, \tag{7}$$

where η_1 and η_3 are arguments for which the $u(\eta)$ function has extrema (see Fig. 2), and

$$A = \int_{\eta_1}^{\eta_3} f(\eta)d\eta$$

is a quantity characterizing the degree of supersaturation of the metastable phase of the bistable system in the two-phase region. A formal similarity to the well-known Lifshits–Slezov [10] expression for decomposition of a supersaturated solid solution will be demonstrated below. Indeed, for $A > 0$, we have switching from the weakly absorbing state η_1 to the strongly absorbing state η_3. For $A < 0$, inverse processes occur in the medium.

The state space (phase space) for this system is a straight line; displacement of the representative point $\eta(\theta)$ along this line corresponds to the system's motion. In the range of the kinetic phase transition (in the vicinity of point *2*), both weakly *1* and strongly *3* absorbing exciton phases coexist on the illuminated surface. Using (7), we can estimate the thickness of the phase-discontinuity interface at

$$(2A)^{1/2}(\eta_3 - \eta_1)^{-1}\left(\frac{\partial f}{\partial \eta}\bigg|_{\eta = \eta_3}\right)^{-1} \le \Delta\rho \le (2A)^{1/2} \times (\eta_3 - \eta_1)^{-1}\left(\frac{\partial f}{\partial \eta}\bigg|_{\eta = \eta_1}\right)^{-1}, \tag{8}$$

where the quantities

$$\left(\frac{\partial f}{\partial \eta}\bigg|_{\eta = \eta_1}\right)^{-1}, \quad \left(\frac{\partial f}{\partial \eta}\bigg|_{\eta = \eta_3}\right)^{-1}$$

signify characteristic times of processes occurring in each of the competing phases.

4. NUCLEATION

Transition from metastable phase η_2 to stable phase η_3 occurs via the fluctuational origination of small clusters of new phase nuclei in the homogeneous medium. The probability of a single-nucleus state appearing in the system is governed by the minimum work necessary to form a nucleus of a given size on the plane [11]:

$$A_{\min} = n_3 l(\mu_3 - \mu_2)S + \alpha P, \tag{9}$$

where $S = 4\pi R^2$ and $P = 2\pi R$ are the area and the perimeter of the nucleus, respectively; α is the energy per unit phase-boundary length; and μ_2 and μ_3 are the chemical potentials within and outside the nucleus, respectively.

For a nucleus in equilibrium with the surrounding medium, we have

$$\frac{dA_{\min}}{dR}\bigg|_{R_c} \equiv 0; \tag{10}$$

therefore,

$$\mu_2 - \mu_3 = \frac{\alpha}{4n_3 l R_c}. \tag{11}$$

Taking into account (11), we obtain

$$A_{\min} = -\frac{\pi\alpha}{R_c}R^2 + 2\pi\alpha R. \tag{12}$$

If the displacement of a nucleus as a whole is disregarded and the nucleus is assumed to be stable with respect to changes in its shape, the locally equilibrium size-distribution function for a nucleus is determined by the maximum of the function $A_{\min}(R)$:

$$f_0(R) = f_0(R_c)\exp\left[\frac{\pi\alpha}{TR_c}(R - R_c)^2\right], \tag{13}$$

$$f_0(R_c) = C\exp\left(-\frac{\pi\alpha}{T}R_c\right). \tag{13a}$$

As is known, the preexponential factor in $f_0(R_c)$ cannot be expressed only in terms of the macroscopic characteristics of phases [12]. A fluctuational evolution of nuclei in the critical nucleus-size range of width $\delta R \approx (TR_c/\pi\alpha)^{1/2}$ around the critical point $R = R_c$ can transfer them back into the subcritical region, while nuclei with supercritical sizes will necessarily develop into a new phase. However, the thermodynamic approach fails to account for the processes occurring in transition to a new state. A kinetic approach to the nucleus evolution is necessary in this case.

5. INDEPENDENT GROWTH OF NEW PHASE NUCLEI

Let us find the law of propagation for a circular front whose radius R is larger than the transition-layer thickness $\Delta\rho$.[1] In polar coordinates, with account taken of the axial symmetry, Eq. (5) can be rewritten as

$$\frac{\partial\eta}{\partial\theta} = f(\eta) + \frac{1}{\rho}\frac{\partial\eta}{\partial\rho} + \frac{\partial^2\eta}{\partial\rho^2}. \quad (14)$$

In fact, the derivative $\partial\eta/\partial\rho$ is nonzero only within a narrow transition layer near the point $\rho = R$. Therefore, we can approximately set $\rho = R$ in the second term in the right-hand side of Eq. (14). We note that any convex domain tends to become ideally circular on the plane [13, 14].

Let $V(R)$ be the instantaneous speed of propagation of a circular front with radius R. With account taken of the approximations made above, such a front corresponds to a self-similar solution

$$\eta = \eta(\xi), \quad \xi = \rho - V(R)\theta \quad (15)$$

to the differential equation

$$-V(R)\eta' = f(\eta) + R^{-1}\eta' + \eta'' \quad (16)$$

with the boundary conditions

$$\eta \longrightarrow \eta_1 \quad \text{for} \quad \xi \longrightarrow +\infty \quad \text{and} \quad \eta \longrightarrow \eta_3 \quad \text{for} \quad \xi \longrightarrow -\infty. \quad (17)$$

We call attention to the fact that Eq. (16) coincides with the equation for a plane switching wave moving with a velocity V related to the velocity $V(R)$ of propagation of a circular front with radius R by

$$V(R) = V - R^{-1}. \quad (18)$$

On the other hand, if we multiply both sides of Eq. (16) by the derivative $d\eta/d\xi$ and integrate with respect to ξ from $-\infty$ to $+\infty$ taking into account the boundary conditions, we obtain

$$V = V(R) + R^{-1} \equiv A\left[\int_{-\infty}^{+\infty}\left(\frac{d\eta}{d\xi}\right)^2 d\xi\right]^{-1}. \quad (19)$$

If we still consider a nucleus at rest, $V(R) = dR/d\theta$. This, taken together with (18), implies that

$$\frac{dR}{d\theta} = V - R^{-1}. \quad (20)$$

Equation (20) in fact means that we assumed the processes at the phase boundary to be fast enough, so that a local equilibrium is established at any point of the boundary. From the stability condition for the wave front contour R it follows that

$$R_c = V^{-1} \equiv A^{-1}\int_{-\infty}^{+\infty}\left(\frac{d\eta}{d\xi}\right)^2 d\xi, \quad (21)$$

whence it can be seen that the quantity A also has a formal significance of the degree of supersaturation of the metastable phase of the bistable system [10]. Thus,

$$\frac{dR}{d\theta} = \frac{1}{R_c} - \frac{1}{R}. \quad (22)$$

For $R < R_c$, we have $dR/d\theta < 0$ and two-dimensional (2D) droplets of radius R dissolve in the metastable environment; for $R > R_c$, $dR/d\theta > 0$ and the 2D droplets grow. Nuclei of critical radius R_c, at equilibrium with the surrounding medium, neither grow nor dissolve.

In the stage of independent growth of supercritical nuclei, their mean size significantly exceeds R_c. In addition, a decrease in supersaturation can be neglected while determining the nucleus growth rate for the initial stage of growth. Then we use Eq. (22) to determine the time dependence of nucleus radius significantly exceeding the critical value:

$$R(\theta) = R(0) + R_c^{-1}\theta. \quad (23)$$

The essential difference between (23) and the result obtained in [15] can be explained as follows. In our case, the kinetics of nucleus growth is determined by particles attachment to and detachment from the 2D interface, rather than by their diffusion in solution.

The maximum possible size R_m of droplets in the stage of their independent growth can be found from the equation for the relative growth rate [16]:

$$\frac{d}{dR}\left(\frac{\dot{R}}{R}\right)\Bigg|_{R = R_m} = 0, \quad (24)$$

whence follows $R_m = 2R_c$. We note that the Lifshits–Slezov theory [10] yields $R_m = (3/2)R_c$ for the growth of new phase nuclei via volume diffusion.

6. THE FINAL STAGE OF FORMATION OF A STRONGLY ABSORBING STATE

In the late stages of the first-order phase transition, larger droplets of the new phase grow at the expense of the dissolution of smaller droplets [10, 17]. Ostwald ripening (the term that is commonly accepted for the final stage of the first-order phase transition) begins when the degree of supersaturation A tends to zero. This condition resembles the well-known Maxwell rule that is related to the possibility of spatial coexistence of liquid and gaseous phases [18] and suggests in our case the possibility that there exists a static front of the wave of switching between different states. In other words, a highly developed phase-boundary surface appears in

[1] Hereinafter, R stands for the value normalized to the diffusion length $L \approx (D_\perp\tau)^{1/2}$.

the nonequilibrium system, to which the Ostwald ripening stage is commonly related [14]. We note that fluctuational nucleation is impossible in this stage because the critical size is large.

Equation (22) is identical to the expression describing the final stage of formation of an island film from a supersaturated solid solution of atoms adsorbed by a substrate [19]. The growth is governed by the rate of quasiparticle attachment to the perimeter of a growing droplet of the new phase; this rate is equal to unity in our case (in dimensionless units).

Regarding $dR/d\theta$ as the velocity of nucleus motion in the size space, we write the continuity equation in this space as

$$\frac{\partial f}{\partial \theta} + \frac{\partial}{\partial R}\left(f\frac{\partial R}{\partial \theta}\right) = 0. \quad (25)$$

The nucleus size-distribution function is normalized in such a way that the quantity

$$N(\theta) = \int_0^\infty f(\theta, R)dR \quad (26)$$

is the number of nuclei per unit volume. Finally, the conservation of the total number of quasiparticles is expressed by the equation

$$A(\theta) + \pi\int_0^\infty R^2 f(\theta, R)dR = A_0, \quad (27)$$

where A_0 is the total initial supersaturation.

Equations (22), (25), and (27) constitute a complete set of equations for the problem under consideration. Substituting Eq. (22) into Eq. (25), we obtain the distribution function in the form in which it was derived previously for island films [19]:

$$f(u) = Cu(2-u)^{-4}\exp\left(-\frac{4}{2-u}\right), \quad (28)$$

where $u = R/R_c$. The normalizing constant C can be determined from Eq. (27).

Evidently, this size-distribution function for the nucleus does not exhaust all the possible mechanisms of new-phase nucleus coarsening. However, to take these mechanisms (e.g., diffusion from the surrounding medium) into account, it would be necessary to make assumptions that do not follow directly from the physical model described in Section 2. We note also that the approach used in this section has been developed for describing the final stage of the phase transition from a high-density exciton gas to an electron–hole liquid [20].

7. CONCLUSION

Thus, the formation kinetics for a strongly absorbing state in the bistable exciton noncavity system can be described in terms of first-order phase-transition kinetics. This can be explained by the fact that the combined action of high-intensity laser radiation and exciton density fluctuations can transfer the system across the separatrix from an attraction domain of one attractor to that of another (Fig. 3). Such a response of the observable quantity resembles the first-order phase transition in the equilibrium thermodynamics. External noise (light intensity fluctuations) leads to widening of the bistability range for the system under consideration [21], without, however, (and this is important) any significant change in the formation kinetics for the strongly absorbing state.

In contrast with the equilibrium thermodynamics, where a phase transition links stable states, in the formation of a strongly absorbing exciton state in a semiconductor, the transition connects two nonequilibrium states of the system, the existence of these states being maintained by high-power external laser radiation. As is known, advances in the theory of self-organizing systems are in the first place due to the fact that thermodynamically nonequilibrium systems in a steady state with detailed balance are formally indistinguishable from equilibrium systems [19], for whose analysis the efficient mathematical tools have been developed [18]. The physical state of such a thermodynamic system exhibiting strong deviation from the equilibrium is determined by its characteristic function, i.e., by its generalized thermodynamic potential. The kinetics of phase transitions in the aforementioned systems is represented by the Landau–Khalatnikov equation that describes the relaxation of the phase variable to a new, energetically more favorable state.

However, such a procedure is inapplicable to most physically important situations in the nonequilibrium kinetics [e.g., for the model described by Eq. (4)], because of difficulties encountered in constructing the generalized thermodynamic potential. The approach developed above describes the evolution of a highly nonequilibrium system by formal analogy with the decomposition of a supersaturated solid solution without using the concept of the generalized thermodynamic potential. The proposed description method makes it possible to study the kinetics of a wide range of nonequilibrium systems in different stages of a phase transition without any additional conjectures concerning the basic kinetic equation of the model.

REFERENCES

1. H. Gibbs, *Optical Bistability: Controlling Light with Light* (Academic, New York, 1985; Mir, Moscow, 1988).
2. A. M. Bakiev, V. S. Dneprovskiĭ, Z. D. Kovalyuk, and V. P. Stadnik, Pis'ma Zh. Éksp. Teor. Fiz. **38**, 493 (1983) [JETP Lett. **38**, 596 (1983)].
3. V. S. Dneprovskiĭ, V. I. Klimov, E. V. Nezvanova, and A. I. Rurtichev, Pis'ma Zh. Éksp. Teor. Fiz. **45**, 580 (1987) [JETP Lett. **45**, 740 (1987)].

4. *Optical Computing: Digital and Symbolic*, Ed. by R. Arratoon (Marcel Dekker, New York, 1989; Mir, Moscow, 1993).
5. *Self-Organization in Optical Systems and Application in Information Technology*, Ed. by M. A. Vorontsov and N. B. Miller (Springer-Verlag, Berlin, 1995).
6. P. I. Khadzhi and S. L. Gaĭvan, Kvantovaya Élektron. (Moscow) **24**, 546 (1997).
7. P. I. Khadzhi and S. L. Gaĭvan, Fiz. Tverd. Tela (St. Petersburg) **40**, 932 (1998) [Phys. Solid State **40**, 858 (1998)].
8. Ya. B. Zel'dovich and D. A. Frank-Kamenetskiĭ, Zh. Fiz. Khim. **12**, 100 (1938).
9. Al. S. Mikhailov, *Foundation of Synergetics: I. Distributed Active Systems* (Springer-Verlag, Berlin, 1994).
10. I. M. Lifshits and V. V. Slezov, Zh. Éksp. Teor. Fiz. **35**, 479 (1958) [Sov. Phys. JETP **8**, 331 (1959)].
11. E. A. Brener, V. I. Marchenko, and S. V. Meshkov, Zh. Éksp. Teor. Fiz. **85**, 2107 (1983) [Sov. Phys. JETP **58**, 1223 (1983)].
12. E. M. Lifshitz and L. P. Pitaevskiĭ, *Physical Kinetics* (Nauka, Moscow, 1979; Pergamon, Oxford, 1981).
13. Yu. E. Kuzovlev, T. K. Soboleva, and A. É. Philippov, Zh. Éksp. Teor. Fiz. **103**, 1742 (1993) [JETP **76**, 858 (1993)].
14. B. Meerson and P. V. Sasorov, Phys. Rev. E **53**, 3491 (1996).
15. V. I. Marchenko, Pis'ma Zh. Éksp. Teor. Fiz. **64**, 61 (1996) [JETP Lett. **64**, 66 (1996)].
16. R. D. Vengrenovich, Acta Metall. **20**, 1079 (1982).
17. C. Wagner, Z. Elektrochem. **65**, 581 (1961).
18. L. D. Landau and E. M. Lifshits, *Statistical Physics* (Nauka, Moscow, 1995; Pergamon, Oxford, 1980), Part 1.
19. R. D. Vengrenovich, Ukr. Fiz. Zh. (Russ. Ed.) **22**, 219 (1977).
20. J. H. Yao, H. Guo, and M. Grant, Phys. Rev. B **47**, 1270 (1993).
21. Yu. V. Gudyma, Izv. Vyssh. Uchebn. Zaved., Fiz., No. 12, 94 (1998).

Translated by S. Ktitorov

Semiconductors, Vol. 34, No. 12, 2000, pp. 1376–1380. Translated from Fizika i Tekhnika Poluprovodnikov, Vol. 34, No. 12, 2000, pp. 1432–1437.

ELECTRONIC AND OPTICAL PROPERTIES OF SEMICONDUCTORS

Photoluminescence of $Ga_{1-x}In_xAs_ySb_{1-y}$ Solid Solutions Lattice-Matched to InAs

K. D. Moiseev, A. A. Toropov, Ya. V. Terent'ev, M. P. Mikhaĭlova, and Yu. P. Yakovlev

Ioffe Physicotechnical Institute, Russian Academy of Sciences, Politekhnicheskaya ul. 26, St. Petersburg, 194021 Russia

Submitted June 16, 2000; accepted for publication June 21, 2000

Abstract—Photoluminescence of $Ga_{1-x}In_xAs_ySb_{1-y}$ ($0.08 < x < 0.22$) epilayers lattice-matched to InAs substrate was investigated for the first time at 80 K, and the band gap of solid solutions was evaluated experimentally. It was demonstrated that the intensity of the band-to-band radiative recombination for *p*-GaInAsSb undoped layers depends on the composition of the quaternary solid solution and is governed by the concentration of intrinsic structural defects. For an *n*-GaInAsSb:Te donor-doped layer, the band-to-band recombination band and an additional emission band were observed. The latter band is related to the radiative recombination via the deep acceptor level formed by an intrinsic complex V_{Ga}Te with the activation energy E_{DA} = 122 meV.

In recent years, narrow-gap heterostructures based on solid solutions of the GaSb–InAs system have been widely used as promising materials in the design of optoelectronic devices for a spectral range of 3–5 μm [1–3]. The best known applications of these devices are diode-laser high-resolution spectroscopy, gas analysis, and ecology monitoring [4]. Solid solutions of the Ga–In–As–Sb system can form both steplike and separated type II heterojunctions (HJs) with InAs and GaSb [5]. The spatial separation and localization of electrons and holes on both sides of the type II heterointerface ensure a high probability of indirect radiative recombination transitions. This is of interest for the design of highly efficient light-emitting diodes and photodiodes as well as new types of tunneling–injection lasers operating in the middle infrared region [6, 7]. The existence of a two-dimensional high-conductivity channel at the interface of a broken-gap type II HJ offers many possibilities for the design of GaInAsSb/InAs-based Hall sensors.

Currently, the properties of $Ga_{1-x}In_xAs_ySb_{1-y}$/GaSb type II steplike heterostructures with layers of GaSb-enriched quaternary solid solutions lattice-matched to GaSb substrate have been studied in great detail [8]. The list of publications devoted to the $Ga_{1-x}In_xAs_ySb_{1-y}$/InAs broken-gap type II heterostructures with layers of In-depleted solid solutions lattice-matched to InAs substrate is much shorter. We have demonstrated previously that a single $Ga_{1-x}In_xAs_ySb_{1-y}$/InAs heterostructure with $x < 0.22$ comprises a broken-gap type-II HJ, in which the semimetal channel containing high-mobility electrons exists at the heterointerface [9]. For isotype single *p*-$Ga_{0.84}In_{0.16}As_{0.22}Sb_{0.78}$/*p*-InAs type II heterostructures, an intense electroluminescence (EL) caused by the indirect tunneling radiative recombination of electrons and holes localized at the heterointerface was observed at 77 K [10]. However, no investigations of photoluminescent properties of these $Ga_{1-x}In_xAs_ySb_{1-y}$ epilayers have been carried out yet.

The purpose of this study was to investigate the photoluminescence (PL) of $Ga_{1-x}In_xAs_ySb_{1-y}$ solid solutions lattice-matched to the InAs substrate for the content range close to GaSb. The PL investigations allowed us to directly evaluate the band gap for the solid solution studied and to explain the nature of recombination transitions in the bulk of the epilayer.

The layers of $Ga_{1-x}In_xAs_ySb_{1-y}$ solid solutions with the In content of $0.08 < x < 0.22$ and As content of $y = x + 0.06$, which had an adequate growth morphology, were deposited using a liquid phase epitaxy on InAs(100) substrates. The solution–melt was prepared from pure components: elemental In and Sb with a purity of 99.9999% and 99.999%, respectively, and undoped binary compounds InAs and GaSb with the intrinsic carrier density of $n = 2 \times 10^{16}$ cm^{-3} and $p = 5 \times 10^{16}$ cm^{-3}, respectively. The lattice mismatch between the epilayer and the substrate was no larger than $\Delta a/a < 4 \times 10^{-4}$, where a is the unit-cell parameter. The layer thickness was ~1.5 μm.

The *p*-GaInAsSb undoped layers with the hole density of no higher than $p = 2 \times 10^{16}$ cm^{-3} and *n*-GaInAsSb Te-doped layers with an electron density of $n \approx 0.8 \times 10^{16}$ cm^{-3} were grown. The donor impurity was introduced during epitaxial growth from the solution–melt. For this purpose, the Czochralski-grown GaSb:Te binary single crystals with an electron density of $n = 4.2 \times 10^{17}$ cm^{-3} were used.

Photoluminescence was excited by a continuously operated InGaAs semiconductor laser (λ = 800 nm). The excitation power density at the sample surface was ~10 W/cm^2. The PL signal was analyzed by a single-

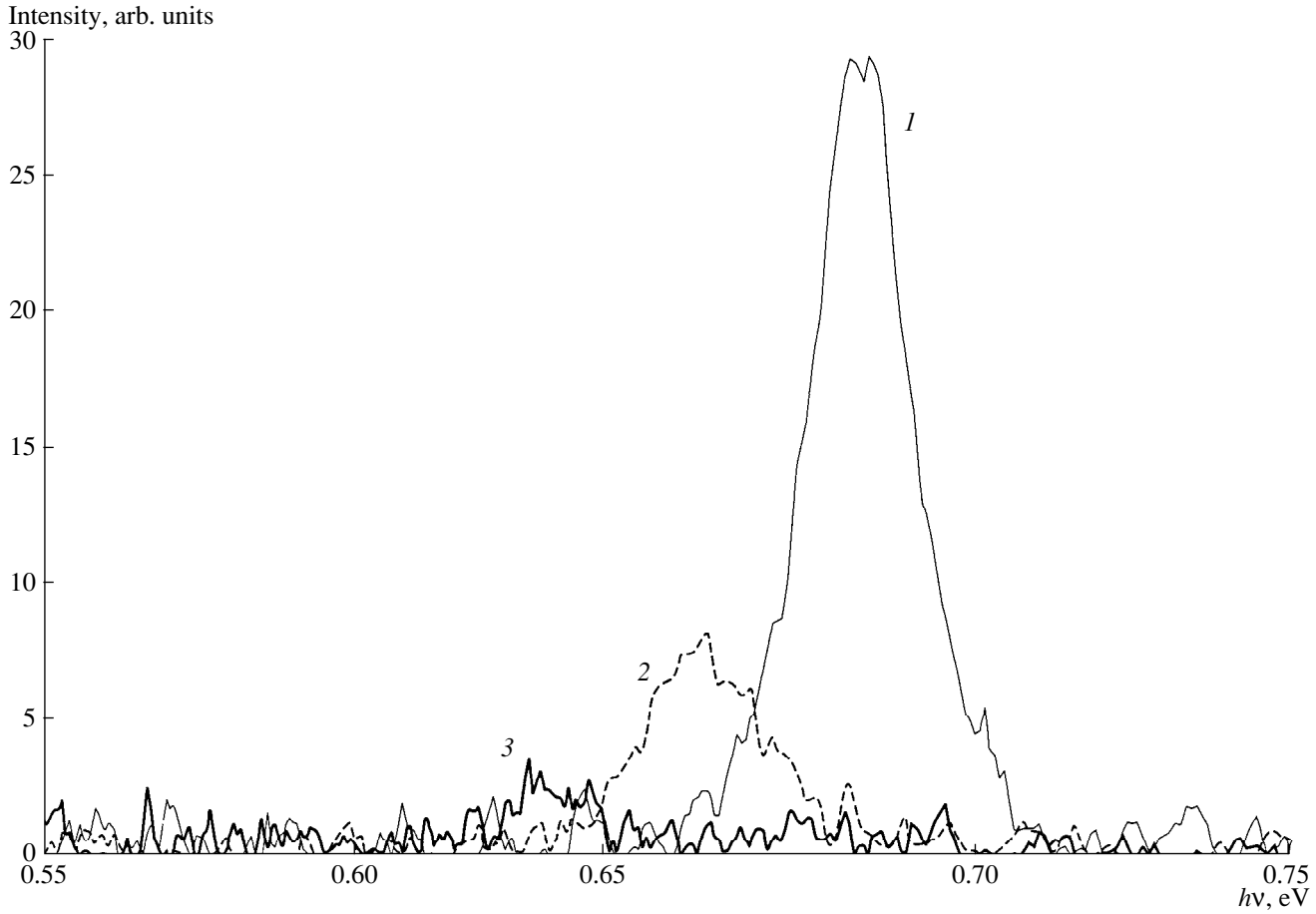

Fig. 1. PL of the *p*-$Ga_{1-x}In_xAs_ySb_{1-y}$ epilayers at $T = 82$ K for In content in the solid solution x = (*1*) 0.09, (*2*) 0.13, and (*3*) 0.17.

grating monochromator with 300 lines per mm and was detected by a thermoelectrically cooled PbS photoresistor in a synchronous mode. The PL spectra were measured at $T = 80$ K.

For single $Ga_{1-x}In_xAs_ySb_{1-y}$/InAs heterostructures with layers of solid solutions (x = 0.09, 0.13, 0.17, and 0.21), PL was observed in the wavelength range of 1.6–2.8 μm, which corresponded to the photon energy range for radiative recombination transitions $h\nu$ = 0.45–0.8 eV.

For $Ga_{1-x}In_xAs_ySb_{1-y}$ undoped layers with weakly pronounced *p*-type conduction, the PL spectra included a single clearly distinguishable emission band peaked at $h\nu_m$ = 680–584 meV. The full width at half-maximum (FWHM) of the peak was equal to 23 meV (Fig. 1). Hereafter, we refer to this emission band as the A_p band. It can be seen in Fig. 1 that the position of the spectral band peak A_p depends on the solid solution composition. The emission band peak shifts to lower photon energies with increasing In content in the epilayer. In addition, the PL intensity depended heavily on the quaternary layer composition at a constant level of an external excitation. When the In content in the solid solution increased from x = 0.09 to x = 0.16, the PL intensity decreased by an order of magnitude. For x = 0.21, the A_p band was barely perceptible against the detector background noise.

The PL spectra for the samples with the $Ga_{1-x}In_xAs_ySb_{1-y}$ doped layers featured two emission bands. There was a high intensity narrow short-wavelength band A_n with FWHM = 22 meV and a broad long-wavelength band B_n with lower intensity FWHM = 80 meV (Fig. 2). It is shown that the peak of the spectral emission bands A_n and B_n also depends on the composition of the GaInAsSb solid solution. If the In content in the epilayer were to increase similarly to the *p*-GaInAsSb layer, the peaks of both bands would be shifted to lower photon energies. However, the A_n band intensity remained unchanged over the total composition range under investigation, while the B_n band intensity decreased with an increase in In content in the solid phase. The B_n band disappeared for the layers with $x > 0.16$. It should be particularly emphasized that the energy separation of the B_n band from the A_n band remained the same for all compositions of the GaInAsSb solid solution: $h\nu_m(A_n) - h\nu_m(B_n) \approx 122$ meV.

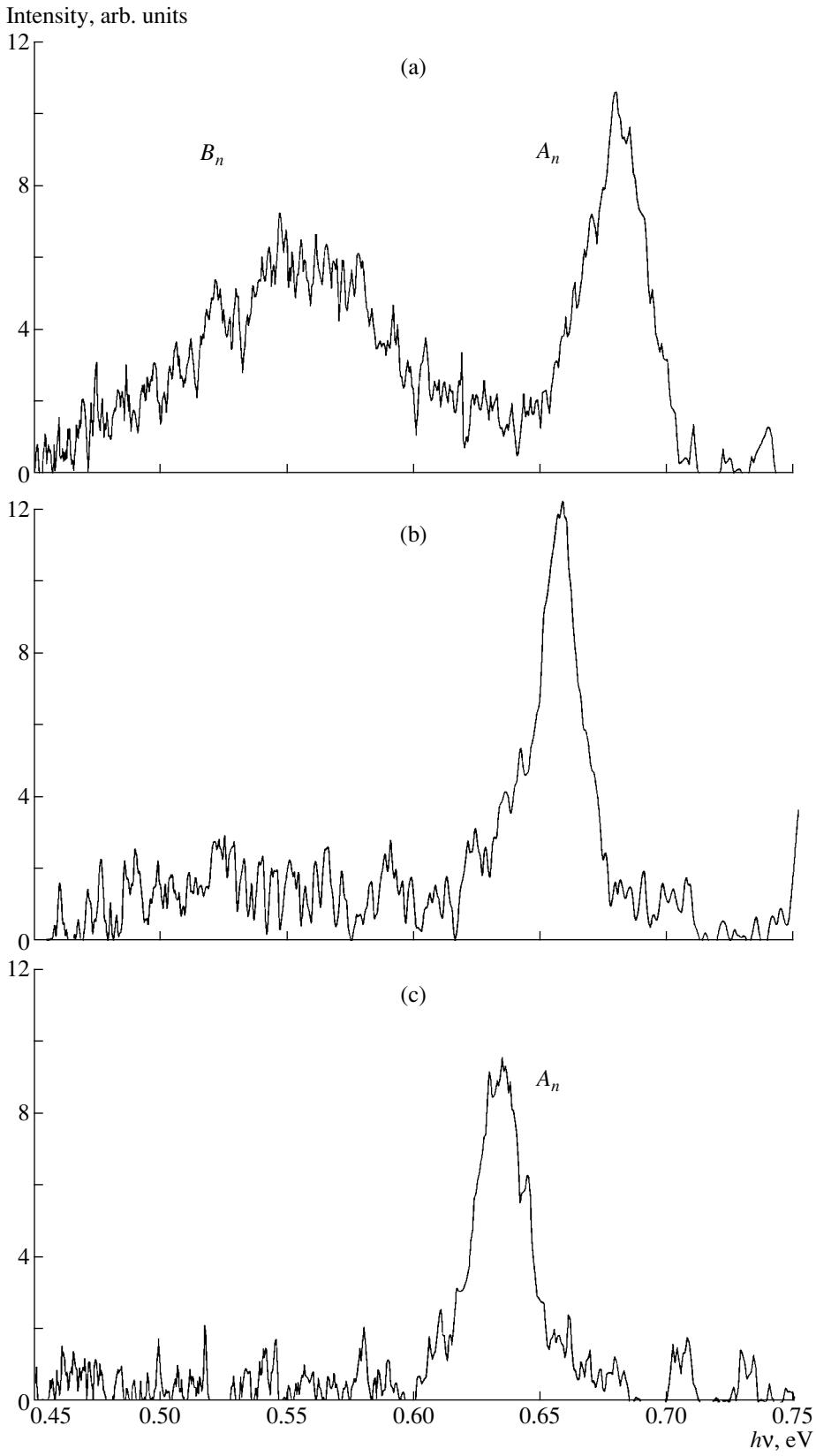

Fig. 2. PL of the n-$Ga_{1-x}In_xAs_ySb_{1-y}$ epilayers at T = 82 K for In content in the solid solution x = (a) 0.09, (b) 0.13, and (c) 0.17.

We also note that the dependences the PL peak intensity I on the solid solution composition are similar for the A_p and B_n emission bands (Fig. 3). The dependence of emission intensity on In content in the epilayer is almost exponential for these bands. We believe that the observed PL bands A_p and B_n correspond to radiative transitions with similar recombination mechanisms, i.e., via recombination centers determined by features of a solid solution formation.

The experimental PL data for the samples are given in the table. It is seen from the table that the photon energies corresponding to the peaks of the A_p and A_n emission bands are almost identical for p- and n-type epilayers with identical compositions of the GaInAsSb solid solution. The measurements were carried out for nondegenerate solid solutions at T = 80 K. All of the donor and acceptor shallow levels in the band gap are thereby ionized. In this case, the A_p and A_n bands can be related to the band-to-band radiative recombination transitions between the conduction and valence bands in the bulk of the GaInAsSb epilayer. Consequently, we can evaluate the band gap for the $Ga_{1-x}In_xAs_ySb_{1-y}$ solid solution at T = 80 K for each composition accurate to thermal band-edge tailing (kT = 7 meV). From the PL data, the band gap for the $Ga_{0.84}In_{0.16}As_{0.22}Sb_{0.78}$ solid solution is E_G = 635 meV. This value is in good agreement with the value of 633 meV obtained from the EL spectra for single p-$Ga_{0.84}In_{0.16}As_{0.22}Sb_{0.78}$/$p$-InAs type II heterostructures at T = 77 K [11].

The experimental points and theoretical curve for the band-gap dependence on the Ga content in the solid solution are shown in Fig. 4. The theoretical curve was calculated from the formula

$$\begin{aligned} E_G &= E_G(\mathrm{InAs})xy + E_G(\mathrm{GaSb})(1-x)(1-y) \\ &+ E_G(\mathrm{InSb})x(1-y) + E_G(\mathrm{GaAs})(1-x)y \\ &- C_{\mathrm{InAsSb}}xy(1-y) - C_{\mathrm{GaAsSb}}(1-x)y(1-y) \\ &- C_{\mathrm{InGaAs}}x(1-x)y - C_{\mathrm{InGaSb}}x(1-x)(1-y), \end{aligned}$$

where C_{InAsSb}, C_{GaAsSb}, C_{InGaAs}, and C_{InGaSb} are the bending parameters of the band-gap dependence on the concentration for ternary compounds [11, 12]. Our experimental data are in good agreement with the calculated band-gap curve and demonstrate that the band gap of the epilayer for $Ga_{1-x}In_xAs_ySb_{1-y}$ ($0.08 < x < 0.22$) quaternary solid solutions lattice-matched to InAs decreases with an increase in In content in a solid phase.

The distinctions in the dependences of the intensity for emission bands A_p and A_n on the solid solution composition (see Fig. 3) can be explained by the differences in recombination mechanisms. For p-type undoped layers, the radiative recombination proceeds via the acceptor recombination centers related to intrinsic structural defects [13]. However, for n-type solid solutions, we may assume that the conduction-band electrons recombine with the valence-band holes via Te shallow acceptor levels with an activation energy of E_D = 3 meV [14].

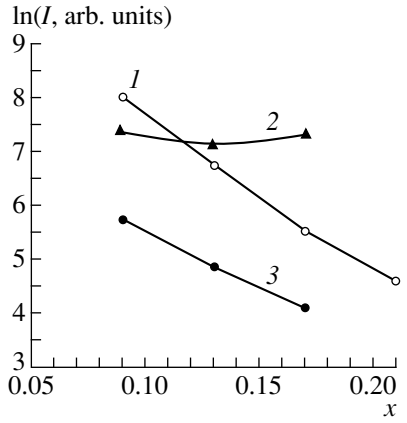

Fig. 3. Dependence of the PL intensity I on In content in the $Ga_{1-x}In_xAs_ySb_{1-y}$ solid solution: (*1*) the A_p band, (*2*) A_n band, and (*3*) B_n band.

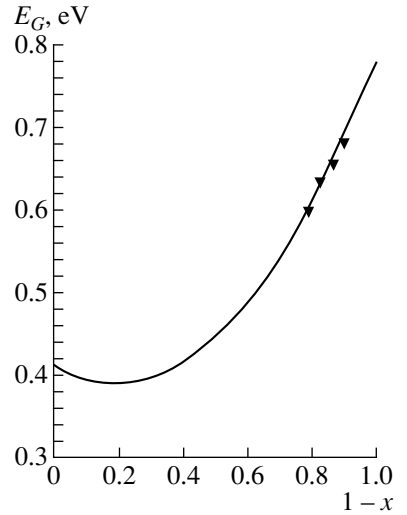

Fig. 4. Dependence of the band gap E_G for the quaternary solid solution $Ga_{1-x}In_xAs_ySb_{1-y}$ on the Ga content; points represent the experimental data, and the solid line corresponds to calculation [11].

For n-GaInAsSb doped layers, a weak dependence of the PL intensity on the solid solution composition can be explained by a slight variation of the carrier density in the epilayer. In particular, the electron density varied from $n = 8.0 \times 10^{16}$ cm^{-3} for x = 0.09 to $n = 6.0 \times 10^{16}$ cm^{-3} for x = 0.16. This may affect the PL intensity only slightly.

For the p-GaInAsSb layers, the PL intensity falls by almost an order of magnitude with increasing In content in solid solution from x = 0.09 to x = 0.21. This is probably caused by a decrease in the concentration of acceptors related to intrinsic defects. It has been previously demonstrated [15, 16] that the GaInAsSb

Parameters of the PL spectra

In content	$h\nu_m(A_p)$, meV	$h\nu_m(A_n)$, meV	$h\nu_m(B_n)$, meV	$h\nu_m(A_n) - h\nu_m(B_n)$, meV
0.09	680	678	556	122
0.13	567	565	533	122
0.16	635	637	–	–
0.21	584	–	–	–

undoped GaSb-enriched solid solutions feature the *p*-type conduction due to the intrinsic structural defects V_{Ga} or $V_{Ga}Ga_{Sb}$, which introduce double-charged acceptor levels in the band gap. In addition, an increase in In content in the epilayers of the $Ga_{1-x}In_xAs_ySb_{1-y}$ solid solutions leads to a decrease in the concentration of the V_{Ga} centers. This brings about the so-called healing of structural defects. In this case, the concentration of acceptor recombination centers decreases almost by an order of magnitude with increasing In content in solid solution from $x = 0.08$ to $x = 0.17$ [17]. Thus, we could expect a corresponding decrease in the PL intensity, which was observed in this experiment.

This supposition was also confirmed by the dependence of the B_n-band characteristics on the solid solution composition for *n*-GaInAsSb:Te doped layers. If the *p*-type semiconductor with multicharge acceptor levels is compensated by a donor impurity, the electrons from the donor levels occupy the shallow acceptor levels. This leads to the possibility of recombination via lower acceptor states [18]. Because of this, the B_n band can be related to the radiative recombination transition of the conduction-band electrons to a deep-level acceptor with an activation energy $E_{DA} = 122$ meV. Such deep-level acceptors can be attributed to the impurity complexes V_{Ga}Te [19]. Similar to the *p*-$Ga_{1-x}In_xAs_ySb_{1-y}$ undoped layers, a decrease in the concentration of V_{Ga} and, correspondingly, of V_{Ga}Te structural defects with increasing In content in the solid solution causes the PL intensity to decrease. For *p*-GaInAsSb In-enriched layers ($x > 0.15$), the B_n emission band is actually absent in the PL spectra.

Thus, the PL of $Ga_{1-x}In_xAs_ySb_{1-y}$ ($0.08 < x < 0.22$) solid solutions lattice-matched to InAs was investigated for the first time at $T = 80$ K, and the band gap E_G was evaluated experimentally. The compositional dependence of E_G was established for a Ga–In–As–Sb quaternary system with solid solutions lattice-matched to InAs. It was demonstrated that the intensity of the band-to-band radiative recombination for the *p*-GaInAsSb undoped layers depends on the composition of the quaternary solid solution and is governed by the concentration of the intrinsic structural defects. For *n*-GaInAsSb:Te layers, the emission band related to the radiative recombination transitions to the deep acceptor level was observed in the PL spectra along with the band-to-band recombination band. This level is attributed to the intrinsic complex V_{Ga}Te with the activation energy $E_{DA} = 122$ meV.

ACKNOWLEDGMENTS

This study was supported in part by the Russian Foundation for Basic Research, project no. 99-02-18330.

REFERENCES

1. K. D. Moiseev, M. P. Mikhaĭlova, O. G. Ershov, and Yu. P. Yakovlev, Fiz. Tekh. Poluprovodn. (St. Petersburg) **30** (3), 399 (1996) [Semiconductors **30**, 223 (1996)].
2. T. S. Hasenberg. R. H. Miles, A. R. Kost, and L. West, IEEE J. Quantum Electron. **33** (8), 1403 (1997).
3. M. P. Mikhailova, B. E. Zhurtanov, K. D. Moiseev, *et al.*, Mater. Res. Soc. Symp. Proc. **484**, 101 (1997).
4. A. I. Nadezhdinski and A. M. Prokhorov, Proc. SPIE **1724**, 2 (1992).
5. M. P. Mikhailova and A. N. Titkov, Semicond. Sci. Technol. **9** (7), 1279 (1994).
6. A. Andaspaeva, A. N. Baranov, A. Guseĭnov, *et al.*, Pis'ma Zh. Tekh. Fiz. **14**, 377 (1988) [Sov. Tech. Phys. Lett. **14**, 377 (1988)].
7. M. P. Mikhaĭlova, K. D. Moiseev, O. G. Ershov, and Yu. P. Yakovlev, Pis'ma Zh. Tekh. Fiz. **23** (4), 55 (1997) [Tech. Phys. Lett. **23**, 151 (1997)].
8. E. Hulicius, J. Oswald, J. Pangrac, *et al.*, J. Appl. Phys. **75** (8), 4189 (1994).
9. T. I. Voronina, T. S. Lagunova, M. P. Mikhaĭova, *et al.*, Fiz. Tekh. Poluprovodn. (St. Petersburg) **34** (2), 194 (2000) [Semiconductors **34**, 189 (2000)].
10. M. P. Mikhailova, K. D. Moiseev, G. G. Zegrya, and Yu. P. Yakovlev, Solid State Electron. **40** (8), 673 (1996).
11. H. Mani, A. Joullie, A. M. Joullie, *et al.*, J. Appl. Phys. **61** (5), 2101 (1987).
12. A. K. Srivastava, J. L. Zyskind, R. M. Lum, *et al.*, Appl. Phys. Lett. **49**, 41 (1986).
13. D. Effer and P. J. Etter, J. Phys. Chem. Solids **25**, 451 (1964).
14. A. N. Baranov, T. I. Voronina, N. S. Zimogorova, *et al.*, Fiz. Tekh. Poluprovodn. (Leningrad) **19** (9), 1676 (1985) [Sov. Phys. Semicond. **19**, 1030 (1985)].
15. K. F. Longenbach and W. I. Wang, Appl. Phys. Lett. **59**, 1117 (1991).
16. M. Ichimura, K. Higuchi, Y. Hattori, *et al.*, J. Appl. Phys. **68** (12), 6153 (1990).
17. A. N. Baranov, A. N. Dakhno, B. E. Dzhurtanov, *et al.*, Fiz. Tekh. Poluprovodn. (Leningrad) **24** (1), 98 (1990) [Sov. Phys. Semicond. **24**, 59 (1990)].
18. A. I. Lebedev and I. A. Strel'nikova, Fiz. Tekh. Poluprovodn. (Leningrad) **13**, 389 (1979) [Sov. Phys. Semicond. **13**, 229 (1979)].
19. A. S. Kyugeryan, I. K. Lazareva, V. M. Stuchebnikov, and A. É. Yunovich, Fiz. Tekh. Poluprovodn. (Leningrad) **6** (2), 242 (1972) [Sov. Phys. Semicond. **6**, 208 (1972)].

Translated by N. Korovin

Semiconductors, Vol. 34, No. 12, 2000, pp. 1381–1385. Translated from Fizika i Tekhnika Poluprovodnikov, Vol. 34, No. 12, 2000, pp. 1438–1442.

SEMICONDUCTOR STRUCTURES, INTERFACES, AND SURFACES

Type II Broken-Gap InAs/$GaIn_{0.17}As_{0.22}Sb$ Heterostructures with Abrupt Planar Interface

K. D. Moiseev*, A. A. Sitnikova*, N. N. Faleev, and Yu. P. Yakovlev***

** Ioffe Physicotechnical Institute, Russian Academy of Sciences, Politekhnicheskaya ul. 26, St. Petersburg, 194021 Russia*
e-mail: mkd@iropt2.ioffe.rssi.ru
*** Department of Electrical Engineering, Texas Tech University, Lubbock, TX 79409, USA*
e-mail: nfaleev@TTACS.TTU.EDU

Submitted June 23, 2000; accepted for publication June 26, 2000

Abstract—High-quality type II $Ga_{0.83}In_{0.17}As_{0.22}Sb_{0.78}$/InAs heterostructures based on GaSb-rich quaternary solid solutions were grown by liquid phase epitaxy on InAs(001) substrates. GaInAsSb epilayers were grown under planar two-dimensional growth conditions with abrupt and planar interfaces. The thickness of the transition layer on the $Ga_{0.83}In_{0.17}As_{0.22}Sb_{0.78}$/InAs interface enriched with In and Sb was 10–12 Å in perfect structures. The roughness of the upper boundary was entirely determined by the epitaxial-growth conditions and did not exceed 500 Å in structures with a layer thickness of about 2 μm. © *2000 MAIK "Nauka/Interperiodica".*

Narrow-gap heterostructures based on GaInAsSb solid solutions have attracted much attention in recent years as promising materials for the fabrication of light sources which operate in the midinfrared emission range of 3–5 μm topical for gas analysis and ecological monitoring [1, 2].

We showed previously that, in a single broken-gap type II *p*-InAs/*p*-$GaIn_{0.17}As_{0.22}Sb$ heterostructure, there is a semimetal channel on the interface with high carrier mobility (μ_H = 50000–70000 $cm^2/(V\ s)$ at T = 77 K). This channel is formed by spatial separation of electrons and holes on each side of the heteroboundary and by their localization in self-consistent quantum wells [3]. The Hall mobility in the channel depended only slightly on the temperature in the range of 4.2–80 K and it decreased by a factor of 1.5 as temperature decreased from 77 to 4 K [4]. Similar behavior of the Hall mobility was previously observed in a single quantum well in the GaSb/InAs/GaSb structures grown by molecular-beam epitaxy. The basic mechanism of the electron scattering in the well was scattering by the heteroboundary inhomogeneities [5]. Electroluminescence studies of single type II InAs/$GaIn_{0.17}As_{0.22}Sb$ heterostructures showed that an intense interface radiative recombination caused by the indirect (tunneling) transitions of electrons and holes from a semimetal channel through heteroboundary is possible in this structure [6]. A new tunnel-injection laser was proposed and fabricated for the first time on the basis of broken-gap type II $GaIn_{0.17}As_{0.22}Sb$/$GaIn_{0.17}As_{0.22}Sb$ heterojunctions. This laser operates in a 3.18- to 3.26-μm wavelength range at T = 77 K and employs the interface tunnel recombination effect involving a type II heteroboundary [7, 8]. In addition, broken-gap type II InAs/$GaIn_{0.17}As_{0.22}Sb$ heterostructures grown by liquid phase epitaxy (LPE) may be of particular interest as materials for Hall-effect sensors operating at room temperature.

Thus, problems concerning heteroboundary quality and possible mechanisms of the interface formation in type II InGa/$GaIn_{0.17}As_{0.22}Sb$ heterostructures requires closer examination. This paper is concerned with combined X-ray diffraction and electron microscopy studies of quality of the GaInAsSb solid solution epilayers, grown by LPE on the InAs substrates enriched with GaSb. We also studied the interfaces in broken-gap type II lattice-matched GaInAsSb/InAs heterostructures.

We estimated the crystal perfection and determined the mismatch parameters of single broken-gap $Ga_{0.83}In_{0.17}As_{0.22}Sb_{0.78}$/InAs heterostructures by the high-resolution double-crystal X-ray diffraction method using a TRS-1 diffractometer. We used a perfect Ge crystal with high asymmetry for collimation and monochromatization of the primary beam. The divergence of the primary beam for a (004) reflection of Cu$K_{\alpha 1}$ radiation was approximately 1.0″–1.2″. Spectral curves were measured in the $(n_1, -n_2)$ configuration. The angular dispersive broadening of basic peaks due to the difference between the lattice parameters of the crystal (monochromator) and investigated structures was 3.5″. The diffraction curves were measured in the ω-scanning mode with open detector window.

To study the samples by transmission electron microscopy (TEM), we used an EM-420 Philips electron microscope with an accelerating voltage of 100 kV. Samples were prepared using the conventional technique, which included mechanical thinning with subsequent ion etching [9].

Single $GaIn_{0.17}As_{0.22}Sb$/InAs heterostructures were obtained by LPE by growing the GaInAsSb solid-solu-

tion layers on the InAs(100) substrates. The epitaxial growth was performed in purified hydrogen atmosphere in the usual graphite container of a pencil-case type placed into a horizontal quartz reactor. The cooling rate of the system (v_T = 0.5 K/min) was the same for all samples. The growth temperature was measured by a Pt–Pt/Rh thermocouple with an accuracy of 0.2 K; the thermocouple was mounted directly under the growth cell. The layer thickness of $Ga_{0.83}In_{0.17}As_{0.22}Sb_{0.78}$ solid solution was about 1.6 μm.

Samples were grown at fixed initial growth temperature. For each batch of samples, only one of the liquid phase components was varied during epitaxial growth. Fractions of the remaining components of solution–melt were fixed. Components As and Ga in liquid phase were chosen for investigation. The preliminary evaluation of the growth quality was based on such parameters as half-width of the diffraction peaks of the substrate and layer. Comparing the experimental data, we took into account the difference between epilayer thicknesses (preliminary evaluations were performed by the optical method on the sample cleavage; for perfect structures, the layer thickness was refined from the diffraction-curve analysis on the basis of the period of the interference fringes).

As can be seen from Table 1, a significant increase in As fraction in the solution–melt (by 20%) at a fixed Ga content in the liquid phase (x_{Ga} = 0.317) causes a pronounced increase of epilayer thickness at a small variation of the mismatch parameter for the GaInAsSb solid-solution and substrate lattice constants. In this case the half-width (FWHM) of the peak from the substrate remains almost unchanged, but the half-width of the peak from the layer passes a minimum and then increases again. This can be explained by the deviation of liquid-phase composition of GaInAsSb solid solution from optimum conditions of epitaxial growth and, therefore, by disturbance of the crystal perfection of the layer as a whole. Determining in such a way the optimum content of As (x_{As} = 0.069) and fixing the As fraction in liquid phase, we compared the batches of samples with different content of Ga in the solution–melt.

It can be seen from Table 2 that a small variation of the Ga content in the liquid phase (up to 4%) gives rise to a significant variation in the mismatch parameter, and this appreciably influences both the half-widths of the peaks from the substrate and layer and the degree of crystal perfection of epitaxial structures as a whole. It should be noted that we observed the interference fringes in the diffraction curves for the samples with the mismatch parameters varied from $+8 \times 10^{-4}$ to -6×10^{-4}. A further increase in the mismatch parameter causes a decrease in the amplitude and number of the interference fringes. This indicates that the epilayer planarity and smoothness of interfaces deteriorate. Thus, preliminary results showed that there exists a rather wide lattice-mismatch range in which, by changing the microcomponent ratio in the liquid phase, we can obtain perfect solid-solution layers.

Diffraction curves for the two most perfect samples are shown in Fig. 1. Narrower peaks in the diffraction curves, the angular position of which corresponds to 0 on the θ–θ_{Br} axis, are related to the reflection from the InAs(400) substrate, whereas the wider peaks correspond to the reflection from the epilayer. Clear interference fringes about the peaks of reflection from the layer are caused by the interference of radiation diffracted by epitaxial film with planar top and bottom interfaces (between the direct and twice-reflected waves). The period of the interference fringes is inversely propor-

Table 1

Sample	Relative fraction As	$\Delta a/a$, 10^{-4}	Substrate FWHM	Layer FWHM	The layer thickness h, μm
418-1	0.064	+3.9	11.93″	17.4″	1.3
418-2	0.069	+2.8	11.9″	13.8″	2.0
418-3	0.075	+1.9	12.3″	13.9″	2.5
418-4	0.080	~0	–	16.2″	3.0

Table 2

Sample	Relative fraction Ga	$\Delta a/a$, 10^{-4}	Substrate FWHM	Layer FWHM	The layer thickness h, μm
399-2	0.304	–12.4	14.3″	17.2″	0.9
412-1	0.312	–3.7	10.9″	15.4″	1.1
527-1	0.315	+2.0	9.9″	14.2″	1.2
418-2	0.317	+2.8	11.9″	13.8″	2.0

Note: FWHM stands for the full width at half-maximum.

tional to epilayer thickness; variation in their intensity indicates that the transition (gradient) layers exist near the layer–substrate interface. The epitaxial-structure parameters obtained from the diffraction curves are listed in Table 3.

The parameters of epitaxial structures (half-widths of basic peaks and reflection coefficients which are close to the calculated values for the X-ray optical scheme) and also distinct interference fringes suggest that both the structures (Table 3) have a high degree of crystal perfection, and that the epilayers are elastically strained. The peak shape indicates that pronounced composition gradients or deformation exist in the layers (obviously due to the nonoptimal choice of cooling rate of substrates during growth). There is no relaxation of the elastic strains in the structures ($\Delta a/a_{\parallel} = 0$). The density of the point defects is negligible, linear defects of the misfit-dislocation type are also absent in the structures. A distinct extended interference pattern indicates that in both the structures the epilayers are grown in a mode similar to the two-dimensional layer-by-layer epitaxial growth, which allows one, for matched heterostructures, to grow thick perfect crystalline epilayers with compositionally abrupt and planar interfaces.

It is necessary to stress an important feature of the X-ray diffractometry of heterostructures: the apparent correlation between the interference pattern of diffraction and quality of epitaxial structures, first of all, planarity of epilayers. It was shown that the interference pattern of diffracted X-ray radiation occurs (due to fulfillment of precise phase conditions for diffraction, the most sensitive to minimum disturbance of crystal perfection arising at initial stage of elastic strain relaxation. The disturbance of planarity of epilayer due to an increase in the roughness of its top interface and the formation of the structure defects in the vicinity of it cause the spreading of the interference fringes. A further increase in the density and size of defects leads to the full extinction of these oscillations [10]. In this case half-widths of principal peaks and the reflection coefficients may still be close to the calculated values because, in this stage of relaxation of elastic strains, the density of structural defects in the layer is still low, and they are mostly concentrated near the top interface.

Therefore, disturbance of the epilayer planarity due to the broadening of its top (growth) boundary (bottom interface in epitaxial structures is, as a rule, planar) should be considered as the first stage of elastic strain relaxation in heterostructure. This causes disturbance of the layer-by-layer two-dimensional mechanism of the epitaxial growth and formation of defects in the epitaxial structure. The bottom interface at low density of defects (up to formation of the misfit dislocation) remains planar.

We estimated the total inhomogeneity of the epilayer thickness in diffracting volume from the total angular extent of the interference pattern (parameter

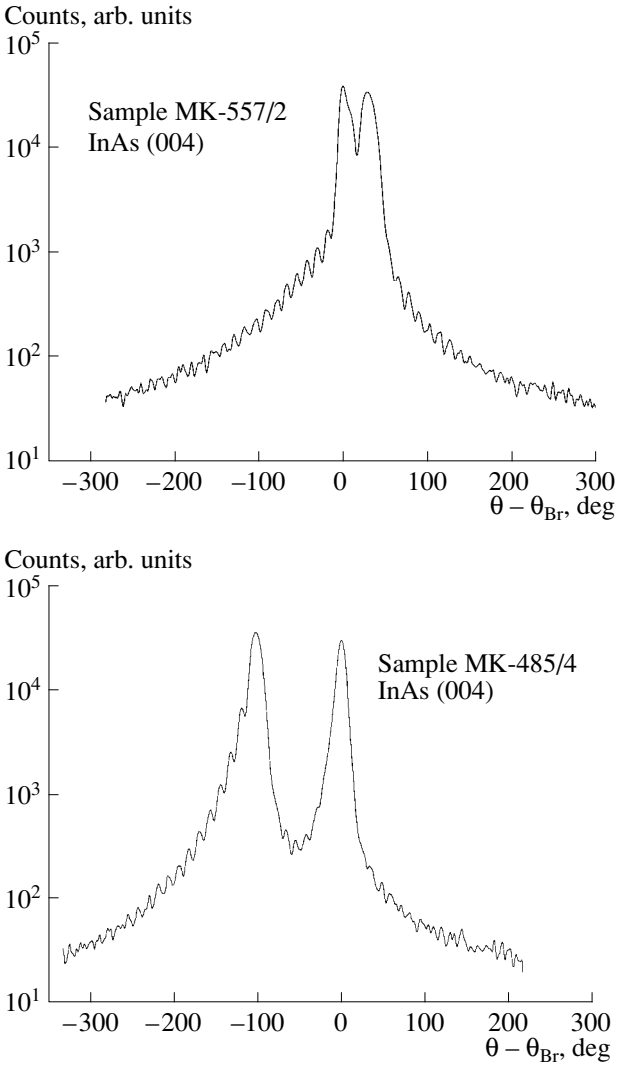

Fig. 1. The mismatch curves for single broken-gap $Ga_{0.83}In_{0.17}As_{0.22}Sb_{0.78}$/InAs heterostructures obtained by double-crystal X-ray diffraction for (004) reflection of Cu$K_{\alpha 1}$ radiation. The mismatch parameters are (a) $\Delta a/a = +8.38 \times 10^{-4}$, (b) $\Delta a/a = -2.38 \times 10^{-4}$.

$\Delta\Theta_{inter}$, see Table 3). It does not exceed 500 Å for investigated structures. This estimate is slightly high because the double-crystal curve is actually a superposition of the coherent and diffuse components of the diffracted X-ray radiation. The diffuse component is caused by the scattering of the X-ray radiation by various structural defects. In the double-crystal curves this causes the spreading of remote interference fringes, and, thus, a decrease in the total extent of the interference patterns.

It was shown above that the variation of the atomic fraction of Ga and As components in the solution–melt allows us to control certain parameters of the grown epilayer. In this case, we can obtain layers of good quality in a rather wide mismatch range for solid solution

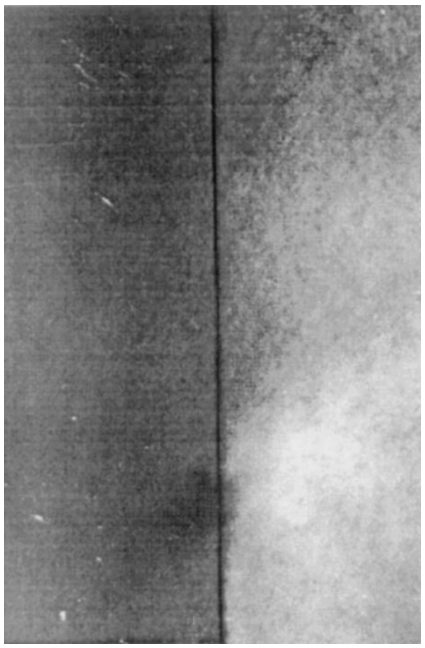

Fig. 2. The interface photograph obtained by the TEM of a single $Ga_{0.83}In_{0.17}As_{0.22}Sb_{0.78}$/InAs heterostructure in the cross-sectional mode with operating ⟨200⟩ reflection.

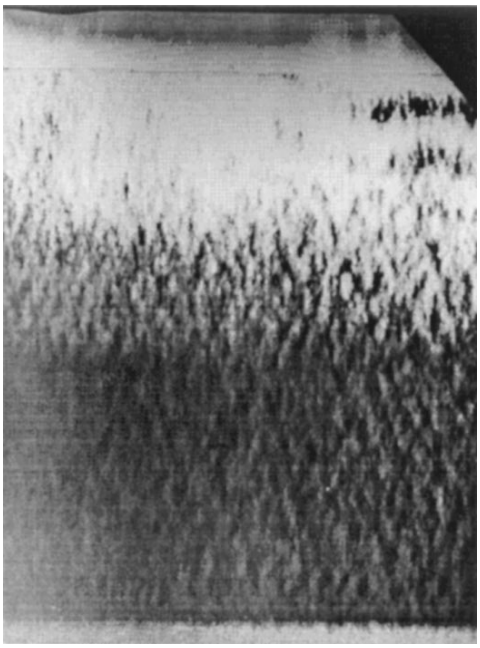

Fig. 3. The cross-sectional photograph obtained by the TEM of a single $Ga_{0.83}In_{0.17}As_{0.22}Sb_{0.78}$/InAs heterostructure with operating ⟨220⟩ reflection.

and substrate. We assume that, in the InAs–GaInAsSb system obtained by LPE, formation of the substrate–layer heteroboundary is governed by heavier solution–melt components, namely, by In and Sb. A similar phenomenon was previously observed in the InP–GaInAsP system [10]. To verify this assumption it was necessary to study the heteroboundary in more detail.

The typical layer–substrate interface image in the diffraction contrast obtained by the TEM is shown in Fig. 2. The image was obtained in a cross-section mode at ⟨200⟩ reflection. The visible dark band against the light background indicates the interface position. As can be seen from a microphotograph, the InAs–GaInAsSb interface is planar and has a thin transition layer 3–4 monolayers (10–12 Å) thick. This is within the limits of InAs(001) natural surface roughness and includes contrast from stresses in the strained boundary regions.

It is well known that ⟨200⟩ reflection is sensitive to the composition, namely, the atomic number *Z*. It follows from Fig. 2 that the composition of the transition layer at the heteroboundary differs from the composition of the materials on both sides of the interface, namely, the $GaIn_{0.17}As_{0.22}Sb$ solid solution and the InAs substrate. The dark–light contrast band at the substrate–layer interface of the solid solution indicates that, in the initial stage of LPE growth, the deposition of the heaviest components of the liquid phase (In and Sb) occurs; i.e., the boundary layer is enriched with indium and antimony (actually, an InSb-type heteroboundary is formed).

The typical cross-sectional image of a single $Ga_{0.83}In_{0.17}As_{0.22}Sb_{0.78}$/InAs heterostructure in the cross-view mode with operating ⟨220⟩ reflection is shown in Fig. 3. Such an orientation is used for detecting defects in the epilayer bulk. As can be seen from the microphotograph, both heteroboundaries are planar and there are no defects in the entire volume of the epilayer. One can also distinctly see that the dislocation loops are absent at the heteroboundary. A similar phenomenon was previously observed in the GaInAsP/InP

Table 3

Sample	Substrate FWHM	Substrate K_{refl}	Layer FWHM	Layer K_{refl}	$\Delta\Theta_{s1}$	$\Delta a_\perp$, Å	$\Delta a/a$, 10^{-4}	$\Delta\Theta_{osc}$	The layer thickness h, μm	$\Delta\Theta_{inter}$	Δh, μm
MK-485	10.30″	0.305	14.95″	0.355	–102″	$+5.05 \times 10^{-3}$	+8.38	12.20″	1.50	350″	±0.050
MK-557	10.1″	0.384	17.70″	0.331	+30″	-1.44×10^{-3}	–2.38	12.50″	1.48	420–450″	±0.045

Note: K_{refl} is the reflection coefficient, $\Delta\Theta_{osc}$ is period of the interference fringes, $\Delta\Theta_{inter}$ is total extent of the interference pattern, Δh is nonplanarity of interfaces, and $\Delta\Theta_{s1}$ is position of principal diffraction maximum for the layer.

structures, which are characterized by atomic ordering in solid solution [11]. The planarity of the top interface in the $Ga_{0.83}In_{0.17}As_{0.22}Sb_{0.78}$/InAs heterostructure amounted to about 500 Å (which is comparable with estimates obtained from X-ray diffraction). This is a very good result for a layer about 1.5 μm thick.

Thus, type II perfect-crystal $Ga_{0.83}In_{0.17}As_{0.22}Sb_{0.78}$/InAs heterostructures on the InAs substrate were obtained by LPE on the basis of quaternary solid solutions enriched with gallium antimonide. Epitaxial GaInAsSb layers were grown in conditions of planar two-dimensional growth with compositionally abrupt and planar interfaces. In such structures, the planarity of the bottom interface is governed by the roughness of the InAs(001) surface. The thickness of the transition layer on the $Ga_{0.83}In_{0.17}As_{0.22}Sb_{0.78}$/InAs interface enriched during the growth with heavy components (In and Sb) is 10–12 Å in perfect structures. The roughness of the top boundary is totally governed by the epitaxial growth conditions and does not exceed 500 Å for the most perfect structures with a layer thickness of 1.5–2 μm.

Broken-gap GaInAsSb/InAs heterostructures with a high perfection of the heteroboundary are promising for the development of various device structures. They also constitute a unique object for studying the quantum properties of semimetal channel at a single heteroboundary in a system with two types of carriers (electrons and holes) in the quantization conditions.

ACKNOWLEDGMENTS

This study was supported in part by the Russian Foundation for Basic Research, project no. 99-02-18330.

REFERENCES

1. H. K. Choi, G. W. Turner, and S. R. Kurtz, Appl. Phys. Lett. **65** (18), 2251 (1994).
2. Yu. P. Yakovlev, T. N. Danilova, A. N. Imenkov, *et al.*, in *Proceedings of the 23th International Symposium on Compound Semiconductors, St. Petersburg, 1996*, Ed. by M. S. Shur and R. A. Suris (Inst. of Physics, Bristol, 1997), p. 551.
3. T. I. Voronina, T. S. Lagunova, M. P. Mikhaĭlova, *et al.*, Fiz. Tekh. Poluprovodn. (St. Petersburg) **30** (6), 985 (1996) [Semiconductors **30**, 523 (1996)].
4. M. P. Mikhailova, K. D. Moiseev, R. V. Parfeniev, *et al.*, IEE Proc.: Optoelectron. **145** (5), 268 (1998).
5. P. S. Kop'ev, S. V. Ivanov, N. N. Ledentsov, *et al.*, Fiz. Tekh. Poluprovodn. (Leningrad) **24** (4), 717 (1990) [Sov. Phys. Semicond. **24**, 450 (1990)].
6. M. P. Mikhailova, K. D. Moiseev, G. G. Zegrya, and Yu. P. Yakovlev, Solid State Electron. **40** (8), 673 (1996).
7. K. D. Moiseev, M. P. Mikhaĭlova, O. G. Ershov, and Yu. P. Yakovlev, Fiz. Tekh. Poluprovodn. (St. Petersburg) **30** (3), 399 (1996) [Semiconductors **30**, 223 (1996)].
8. M. P. Mikhaĭlova, K. D. Moiseev, O. G. Ershov, and Yu. P. Yakovlev, Pis'ma Zh. Tekh. Fiz. **23** (4), 55 (1997) [Tech. Phys. Lett. **23**, 151 (1997)].
9. N. A. Bert, A. O. Kosogov, and Yu. G. Musikhin, Pis'ma Zh. Tekh. Fiz. **17** (19), 39 (1991) [Sov. Tech. Phys. Lett. **17**, 731 (1991)].
10. V. G. Gruzdev, A. O. Kosogov, and N. N. Faleev, Pis'ma Zh. Tekh. Fiz. **20** (14), 1 (1996) [Tech. Phys. Lett. **20**, 561 (1996)].
11. A. G. Norman and G. R. Booker, J. Appl. Phys. **57** (10), 4715 (1985).

Translated by I. Kucherenko

Semiconductors, Vol. 34, No. 12, 2000, pp. 1386–1390. Translated from Fizika i Tekhnika Poluprovodnikov, Vol. 34, No. 12, 2000, pp. 1443–1449.

SEMICONDUCTOR STRUCTURES, INTERFACES, AND SURFACES

Special Features of Alpha-Particle Detection with Thin Semi-Insulating 6*H*-SiC Films

N. B. Strokan*, A. A. Lebedev*, A. M. Ivanov*, D. V. Davydov*, and V. V. Kozlovskiĭ**

** Ioffe Physicotechnical Institute, Russian Academy of Sciences, Politekhnicheskaya ul. 26, St. Petersburg, 194021 Russia*

*** St. Petersburg State Technical University, Moskovskiĭ pr. 26, St. Petersburg, 198013 Russia*

Submitted June 22, 2000; accepted for publication June 22, 2000

Abstract—The p^+–n–n^+ structures based on 6*H*-SiC films grown by chemical vapor deposition on the n^+ substrate were irradiated with 8-MeV protons with a dose of 8×10^{15} cm^{-2}. In order to stabilize the material, it was annealed for 10 min at 450°C. As a result, the resistivity of the film was $\rho = 5 \times 10^9$ Ω cm. The effect of proton irradiation was studied by alpha spectrometry. The 5.77-MeV alpha particles were detected for both reverse and forward bias voltages applied to the structure. The results of the following two modes of detection were compared: (i) a particle traverses the structure without losing much of its energy, and (ii) a particle is stopped in the structure. It is shown that, in the former case and under a forward bias, a signal is formed by a mechanism involving a "through-conducting channel." This makes it possible to determine the product of lifetime of electrons by their mobility. The situation in which the particle range R does not exceed the film thickness was analyzed; this situation is typical of spectrometry. It is noted that a decrease in R results in different behavior of the signal for the bias voltages of opposite polarity. Thus, for forward bias, the signal amplitude decreases more rapidly and for larger values of R. © *2000 MAIK "Nauka/Interperiodica".*

INTRODUCTION

The effect of proton irradiation (with doses as high as $\sim 3 \times 10^{14}$ cm^{-2}) on SiC has been studied previously [1]. It was shown that the irradiation gave rise to a system of deep acceptor and donor levels in the *n*-6*H*-SiC band gap. This brings about a large increase in the resistivity ρ as a result of the capture of electrons by the deep-level centers. Measurements of the capacitance–voltage (*C*–*V*) characteristics at T = 700 K (at which temperature even the deepest levels feature the characteristic emission times shorter than 10 μs) yielded the difference concentration $N_D^+ - N_A^- = 9.1 \times 10^{16}$ cm^{-3} for the entire system of defects; this value exceeds the value before irradiation by two times. At the same time, at T = 300 K, a steady decrease in $N_D^+ - N_A^-$ was observed as the dose increased up to 4×10^{14} cm^{-2}; i.e., conductivity compensation occurred.

In this paper, we consider the effect of proton irradiation with doses equal to $\sim 10^{16}$ cm^{-2}. A rapid increase in ρ renders the measurements of *C*–*V* characteristics ineffective; therefore, we used a method related to observation of the nonequilibrium-charge transport and based on the amplitude analysis. The charge was generated by pulsed ionization produced by spontaneous-decay alpha particles.

The parameters of the p^+–n–n^+ structures made it possible to use various modes of particle detection; these modes included use of the forward and reverse bias voltages, the through transit of the particle over the p^+–n layers, and the complete stopping of the particle in the n base of the detector. Thus, the structures constituted a productive model for clarifying the special features of the above detection modes.

The samples were installed in a chamber with a ^{244}Cm alpha-particle source. The possibility of varying the source–sample distance and the angle of incidence of the particles on the detector was provided. By decreasing the particle energy owing to losses in the air and by deviating the angle of incidence from normal, the conditions for stopping the particles in the detector base were ensured. All the measurements were performed at room temperature.

The structures were connected in a conventional circuit, i.e., in series with the power supply and the load resistor. A system for measuring the signal from a separate particle included a preamplifier whose output signal was proportional to the charge at the input, an amplifier with the passband formed by the integrating–differentiating *RC* circuits, and an amplitude analyzer. As a rule, the *RC*-shaping constant amounted to Θ = 0.5 μs. The analyzer's channel was calibrated using the ^{228}Th alpha-decay lines and a reference silicon detector. The energy is related to the charge in terms of the number of electron–hole pairs N as $N = N_{Si}/\varepsilon_{Si} = E_{SiC}/\varepsilon_{SiC}$. Here, ε_{Si} and ε_{SiC} are the mean energies of electron–hole pair formation in Si and SiC, respectively. We used the values of ε_{Si} = 3.62 eV and ε_{SiC} = 9.5 eV.[1]

[1] In publication [2], a smaller value of ε_{SiC} was reported; after the error correction, this value became equal to 9.5 eV.

As mentioned above, we used bias voltages of both polarities. For the forward direction, we attempted to keep the measurement point within the linear portion of the current–voltage characteristic; the structure's resistivity was as high as $10^9\ \Omega$ cm, which indicated that the base conductivity was heavily compensated.

A PARTICLE TRAVERSES THE DETECTOR STRUCTURE

In measurements of this type, the detector was installed at a distance no greater than 15 mm from the source. The vacuum corresponding to ~10^{-2} Torr was provided in the chamber for large source–detector separations.

1. The mode with applied reverse voltage is commonly used for semiconductor detectors. The case of compensating the conductivity of the detector's operating region by deep levels has been studied previously in detail. It was noted (see, for example, [3]) that, for a reverse bias, the preliminarily attained compensation can be upset owing to thermal emission of charge carriers from the deep-level centers. Thus, electrons transferred from the deep-level donors to the conduction band drift to the n^+ electrode and leave behind an uncompensated positive charge in the bulk of the structure. The development of this process with time leads to the situation in which the applied voltage is not sufficiently high for complete depletion. As a result, a region of a neutral high-resistivity base emerges.

The structural transformation described above manifests itself by characteristic variation in the signal kinetics at the detector electrodes. A rapid increase in the signal amplitude (with increasing time of charge-carrier drift transport in the field region) transforms into the stage of response of a high-resistivity base to the appearance of an electron "in excess" with respect to neutrality in this region. The response time is controlled by the Maxwell relaxation constant τ_{Max} and may appreciably exceed the signal-shaping time in the measurement circuit. Since the charge induced at the electrodes is governed by the path w passed by the charge carrier in the interelectrode gap d, the fraction of this charge amounts to w/d (see the insert in Fig. 1).

In the films studied, we indeed observed an upset of compensation if the bias was applied. This means that the emission of electrons from deep levels is significant at room temperature. The time constant of emission is given by

$$\tau_e = [\sigma v N_C \exp(-\Delta E/kT)]^{-1},$$

where σ is the cross section of the charge-carrier capture by the center, ΔE is the depth of the level of the center, v is the thermal velocity, and N_C is the density of states in the conduction band. For example, for the level depth of 0.75 eV, $\sigma = 10^{-15}$ cm^2, and $v = 10^7$ cm/s, we have $\tau_e = 40$ s; thus, the state of compensation related to this level is short-lived.

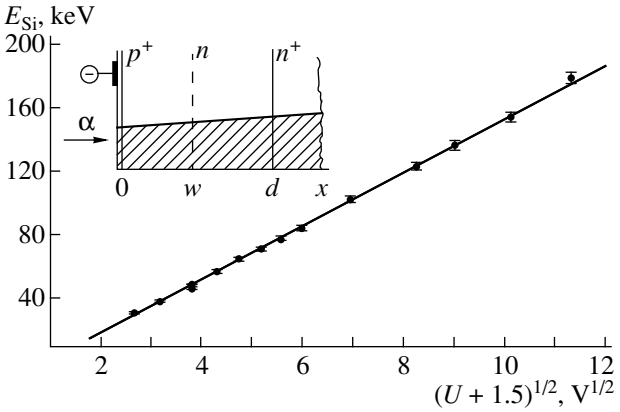

Fig. 1. The signal amplitude at detector D4 (E_{Si}) as a function of the reverse-bias voltage U. The signal amplitude is expressed in the units of energy and is proportional to the charge induced at the detector electrodes. The detector structure is illustrated in the insert. The trend in the specific energy losses of alpha particles with increasing distance x is shown as a cross-hatched area in the insert.

It is reasonable to assume that, in the course of generation of carriers by alpha particles, the transport of nonequilibrium charge occurs effectively only in the high-field region. Under the conditions of high capture-center concentration, the slow (compared to the drift) diffusion is negligible. It follows that the detected charge should be represented as

$$Q \propto (dE_\alpha/dx)w(w/d) \propto w^2,$$

where dE_α/dx is the specific energy loss of alpha particles in SiC.

We measured the dependence of the charge on the bias U applied to the detector. Since $w \propto \sqrt{U}$, it should be expected that $Q \propto U$. However, experimental data (see Fig. 1) were described accurately with the dependence $Q \propto (U + 1.5)^{1/2}$, where the addition term 1.5 V accounted for the contact potential difference at the p^+–n junction. The effective difference concentration $N_D^+ - N_A^- = 2.3 \times 10^{16}$ cm^{-3} was determined from the slope of the curve. In the calculations, we used the values $dE_\alpha/dx = 200$ keV/μm, which corresponded to the onset of stopping of the particle in the curve of specific energy losses. In fact, for the above concentration and a bias of 100 V, the field region extends to mere 2.2 μm, whereas the total range of the particle equals ~20 μm.

A discrepancy between the expected trend $Q \propto U$ and the observed dependence $Q \propto U^{1/2}$ leads to the question as to why, with our experimental conditions, the factor w/d does not manifest itself or, in other words, why the response of the base becomes much faster. In our opinion, this is related to ionization produced by the particle in the base; this ionization significantly modulates the conductivity. An estimation shows that, at the initial point in time, the concentration

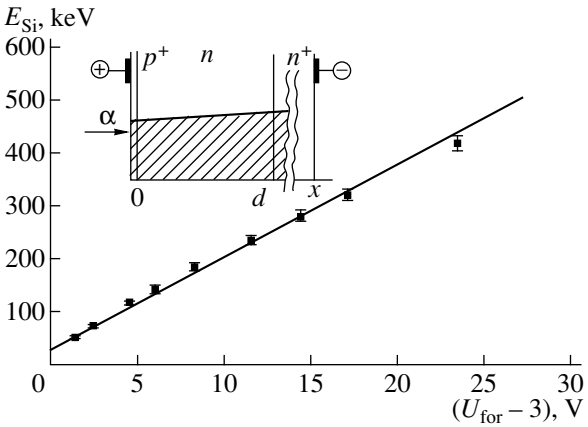

Fig. 2. The signal amplitude at detector D4 (E_{Si}) as a function of the forward-bias voltage U_{for}. The detector structure is illustrated in the insert. The run of specific energy losses of alpha particle is represented as a cross-hatched area.

of charge carriers is as high as $\sim 2 \times 10^{16}$ cm^{-3} in the volume of a track (cylinder) with a cross-sectional area of 1 μm^2. This corresponds to the electrical conductivity of less than 1 $(\Omega\ \text{cm})^{-1}$ and to a relaxation time τ_{Max} on the order of picoseconds; thus, τ_{Max} is six orders of magnitude smaller than the signal-formation time Θ. Undoubtedly, the concentration decreases and τ_{Max} increases as a result of track spreading. However, it should be kept in mind that the state of high conductivity in the base is upset by ambipolar diffusion in a time which is much longer than the characteristic time for the drift of charge carriers in the field. Thus, in our experiments (the average field is $100/2 \times 10^{-4}$ V/cm), the transport of carriers to 2 μm occurred in $\sim 2 \times 10^{-11}$ s. As a result, due to the high nonequilibrium electrical conductivity in the base, induction of the charge at the n^+ electrode corresponded to the charge transport for a distance of d.

2. The reverse-bias mode considered above is specific in that the p^+ and n^+ contacts completely block the arrival of charge carriers from the external circuit. Formation of the signal in the case where the contacts do not limit the arrival of charge carriers was analyzed by S.M. Ryvkin [4]. Later, the mode of "through-conducting channel" was implemented in thin (compared to the particle range) CdS crystals [5]. If we assume in addition that holes are instantaneously trapped (whereas electrons with a longer lifetime circulate in the sample), the transported charge may be represented as

$$Q = q(\mu F\tau/d). \qquad (1)$$

Here, q is the charge produced by ionization, μ and τ are the mobility and lifetime of the electrons, and F is the electric-field strength. It follows from formula (1) that it is possible to amplify the signal; the value of the coefficient $\mu F\tau/d$ is governed by the ratio between the drift length of the electron and the sample thickness.

As mentioned above, an extended linear portion related to high resistivity in the base was observed in the forward current–voltage characteristic of the studied p^+–n–n^+ structures. We may assume that the contact resistance did not restrict the current under these conditions. Furthermore, the lifetime of holes was shorter than that of electrons. As a result, the conditions were not much different from those in the model suggested previously [2, 5]. The experimentally observed dependences of the signal amplitude on the bias were linear (see Fig. 2) and corresponded to $\mu\tau = 7 \times 10^{-9}$ cm^2/V and to an increase in $\mu F\tau/d$ by a factor of 1.7. In the plot, the values of the voltage are diminished by 3 V to take into account the total contact potential difference at the p^+–n and n–n^+ junctions. For the mobility of $\mu \simeq 30$ cm^2/(V s), we obtain $\tau \simeq 2 \times 10^{-10}$ s for the electron's lifetime. It is notable that τ is independent of the forward current; i.e., the change occurring in the level occupation does not affect τ.

The next experiment involved a variation in the geometry of the track. This was achieved by varying the angle of incidence φ of the particles (the angle between the direction of penetration of a particle into the structure and the normal to the detector surface). Correspondingly, the track length increased as $1/\sin(90 - \varphi)$. Figure 3 shows the curve for the signal normalized to the normal incidence of particles for two values of bias differing by a factor of ~4.

According to formula (1), the charge Q is proportional to the quantity

$$Q \propto (dE_\alpha/dx)d(\mu F\tau/d) \propto (dE_\alpha/dx)F, \qquad (2)$$

with the response of cofactors to variation in the angles of incidence being opposite. Specific energy losses increase with the track length according to the Bragg curve, whereas the field strength in the conducting channel decreases. In our opinion, it is this competition that accounts for curve *1* in Fig. 3. As F increases (curve *2*), a steady increase in the signal amplitude is observed. We believe that, for the fields of $F \simeq 5 \times 10^4$ V/cm, the arrangement of the track in the plane of electrodes is conducive to the drift transport of charge carriers of both signs. The mechanism of involving a through-conducting channel is now not predominant, and thus we should not rely on formula (1).

Concluding this section, we report the values of parameters of the films studied; these parameters were determined from the dependences of the signal on the bias voltage according to Figs. 1 and 2 (see the table), where the values of $N_D^+ - N_A^-$ and μτ were determined for the reverse and forward bias applied to the structure, respectively.

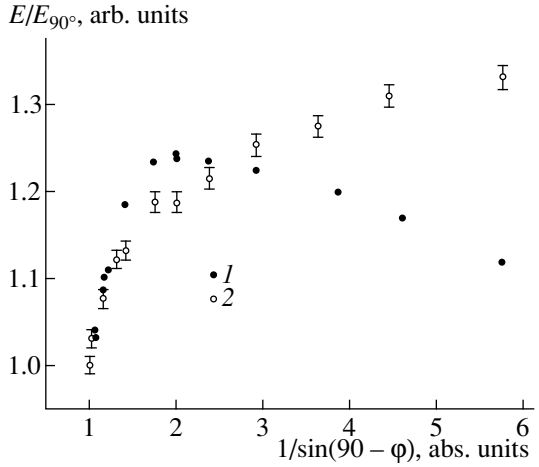

Fig. 3. Dependences of the signal amplitude in the forward-bias mode on the deviation of the angle of incidence of alpha particles from the normal to the detector surface. Detector C4 was used; φ is an angle between the direction of particle motion and the normal to the detector surface. The voltage applied to the detector *n*-base was equal to (*1*) 4.7 and (*2*) 18.7 V.

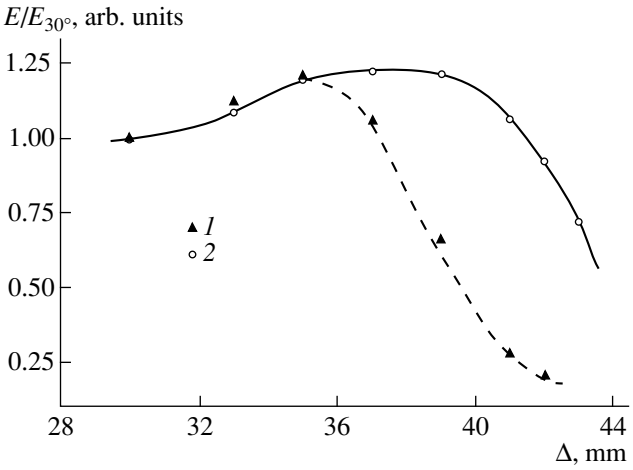

Fig. 4. The behavior of the signal amplitude at detector C4 with decreasing alpha-particle energy for the (*1*) forward- and (*2*) reverse-bias voltages. The source–detector distance is plotted on the horizontal axis. The magnitude of the voltage applied to the detector is (*1*) 20 and (*2*) 100 V.

THE SITUATION WHEN THE PARTICLE IS STOPPED IN THE DETECTOR

We now consider specific features of the charge collection in case where the particle is completely stopped in the detector structure. For the sake of comparison, Fig. 4 illustrates the behavior of the charge collection for the forward- and reverse-bias voltages under the conditions of a progressive decrease in the particle energy due to slowdown of the particles in air. In Fig. 4, the source–detector distance Δ is plotted on the horizontal axis. The signal is normalized to its magnitude at the beginning of the distance range (Δ = 30 mm).

It can be seen from Fig. 4 that a decrease in the signal amplitude occurs after an initial slight increase in the amplitude; the magnitude of this decrease is different for the two modes of biasing. For the forward bias, the charge begins to decrease at higher energies, and this decrease is steeper than that for the reverse-bias voltage. The first portion of the curve (an increase) is accounted for by an increase in the specific energy losses of the particle when it comes to the end of the range. In our opinion, the difference in the signal decrease substantiates the aforesaid about the signal formation.

(I) As soon as a part of the SiC bulk with unmodulated electrical conductivity comes into existence (the result of a decrease in the particle energy), the mode involving a through-conducting channel with free-electron circulation is upset. The through current is limited by the high resistance of the $d - R$ layer (where R is the electron path in SiC), and it is impossible to attain a charge amplification, although it is small in this case. Furthermore, the increment of current when the charge q appears at the sample capacitance C (if the sample resistance is r) is equal to

$$\Delta I = \Delta U/r = q/rC \ll q/t_{dr}.$$

Here, t_{dr} is the characteristic drift time of a charge carrier. Consequently, the induction of a signal at the electrodes of a high-resistivity sample occurs similarly to the case of blocking contacts. It is the path traversed by a nonequilibrium charge carrier in the interelectrode gap d that is important. In these conditions, a decrease in the signal amplitude with decreasing particle energy (Fig. 4, curve *1*) is enhanced by an increasing contribution of transport of holes with a small drift length.

(II) On the other hand, the appearance of the $d - R$ layer is less critical for the signal if a reverse bias is applied. We are reminded that, if electrical conductivity of the detector base is modulated to a depth of R, the signal amplitude is given by $Q = q_0(R/d)$, where q_0 is the charge introduced in the field region. It can be seen from Fig. 4 (curve *2*) that, up to Δ ≈ 40 mm, a decrease (with the rate of R/d) in the signal amplitude is counterbalanced by the fact that the ionization peak of the Bragg curve passes through the field region. Further, the signal amplitude decreases mainly owing to a

Table

The sample	$\mu\tau$, 10^{-9} cm^2/V	$N_D^+ - N_A^-$, 10^{16} cm^{-3}
D4	7.0	2.3
C4	6.0	4.0
B4	6.0	2.45
C3	–	2.2

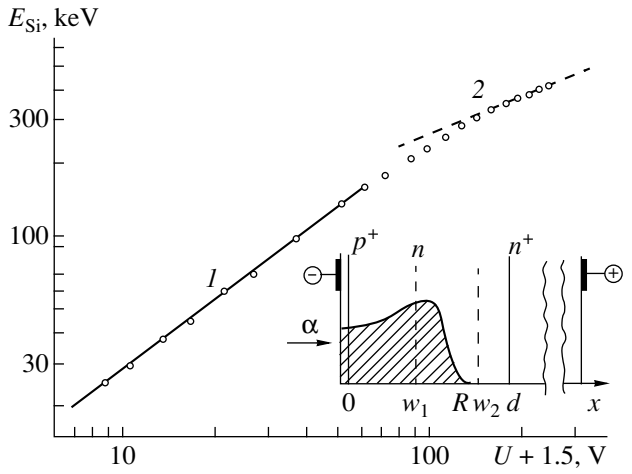

Fig. 5. The signal amplitude as a function of the reverse-bias voltage for complete slowing of alpha particles in the *n* base of detector C4. The inset illustrates the configuration used in the measurements. The profile of specific energy losses of alpha particle for the range R is represented by the cross-hatched area. The boundaries of the depletion region $w_1 < R$ and $w_2 > R$ are related to the linear (portion *1*) and root-square (portion *2*) dependences of the signal amplitude on the bias, respectively.

decrease in ionization efficiency because the value of the factor R/d is bounded below by the value of w/d.

In order to additionally verify the reasoning used in (I) and concerned with the role of the base-conductivity modulation, we measured the charge when the high-resistivity region of the base undoubtedly existed. In these measurements, the track was within the field region for the bias-voltage magnitudes of $U > 100$ V. This was attained by choosing the distance $\Delta \approx 42$ mm and also by rotating the detector and detecting the particles as they entered the detector at an angle of 65° with respect to the normal. The latter condition enhanced the path of the particles in the region of w by $1/\sin(25°)$ times. Under these conditions, the dependence of the signal amplitude on the bias clearly featured two portions. It follows from Fig. 5 that, for low bias voltages, the dependence is almost linear, whereas for larger bias voltages, it transforms into a square-root dependence. Such behavior is quite consistent with the reasoning in (I). Since the structure incorporates a layer of high-resistivity base with a long relaxation time τ_{Max}, the signal amplitude is expressed as $Q = q_0(w/d)$. For $w_1 < R$, the charge q_0 introduced into the base increases as w_1 to a first approximation. As a result, we have $Q \propto (w_1)^2 \propto U$. As U increases, the inequality $w_2 > R$ is fulfilled, in which case we have $q_0(U) = \text{const}$ and $Q \propto w_2 \propto U^{1/2}$.

CONCLUSION

The results are of interest from the an application viewpoint. It is important that the doped layers with large amounts of radiation defects introduced by irradiation (for a total defect concentration of ~10^{17} cm^{-3}) are nevertheless found capable of detecting the fast ions. The problem of operation of the p^+–n detectors based on such layers is related mostly to the decompensation of conductivity rather than to the smallness of the carrier-transport parameters.

It is shown that it is possible to apply the nonconventional forward bias to obtain the mode of through-conducting channel with signal amplification. In relation to this, we mention the results reported elsewhere [6] in which case the above voltage polarity was used for the p^+–π–n^+ detectors based on irradiated Si. Here, the conditions for circulation of electrons in the detector circuit were also met for weakly ionizing particles. However, the ratio between the drift length of electrons and the base width was such that we failed to observe the signal amplification.

In addition, we observed special features of the signal behavior, which are of interest in relation to the basics of the detector operation. This was possible due to the nontrivial combination of the film-structure characteristics and, correspondingly, to the use of four different detection modes. A new approach consists in shaping the signal under the conditions of enhanced conductivity relaxation of the semi-insulating detector base, which is ensured by a high nonequilibrium electrical conductivity in the ion track. Furthermore, we succeeded in observing the transformation of the signal amplitude when the through passage of the particle is replaced by its complete stopping in the detector.

ACKNOWLEDGMENTS

We thank V.K. Eremin for his fruitful participation in discussion of the results and for valuable comments.

REFERENCES

1. A. A. Lebedev, A. I. Veĭnger, D. V. Davydov, *et al.*, Fiz. Tekh. Poluprovodn. (St. Petersburg) **34** (9), 1058 (2000) [Semiconductors **34**, 1016 (2000)].
2. A. A. Lebedev, N. S. Savkina, A. M. Ivanov, *et al.*, Fiz. Tekh. Poluprovodn. (St. Petersburg) **34** (2), 249 (2000) [Semiconductors **34**, 243 (2000)].
3. V. K. Eremin, N. B. Strokan, and N. I. Tisnek, Fiz. Tekh. Poluprovodn. (Leningrad) **8** (6), 1157 (1974) [Sov. Phys. Semicond. **8**, 751 (1974)].
4. S. M. Ryvkin, Zh. Tekh. Fiz. **26** (12), 2667 (1956).
5. N. A. Vitovskiĭ, P. I. Maleev, and S. M. Ryvkin, Zh. Tekh. Fiz. **28** (3), 460 (1958) [Sov. Phys. Tech. Phys. **3**, 434 (1958)].
6. L. J. Beattie, A. Chilingarov, and T. Sloan, Nucl. Instrum. Methods Phys. Res. A **439** (2), 293 (2000).

Translated by A. Spitsyn

Semiconductors, Vol. 34, No. 12, 2000, pp. 1391–1396. Translated from Fizika i Tekhnika Poluprovodnikov, Vol. 34, No. 12, 2000, pp. 1450–1456.

AMORPHOUS, VITREOUS, AND POROUS SEMICONDUCTORS

Vibration Modes of Carbon in Hydrogenated Amorphous Carbon Modified with Copper

V. I. Ivanov-Omskiĭ*, T. K. Zvonareva, and G. S. Frolova

Ioffe Physicotechnical Institute, Russian Academy of Sciences, Politekhnicheskaya ul. 26, St. Petersburg, 194021 Russia

** e-mail: ivanov.ivom@pop.ioffe.rssi.ru*

Submitted June 1, 2000; accepted for publication June 1, 2000

Abstract—Activation in IR absorption of quasi-Raman vibration modes of graphene planes was studied in *a*-C:H modified with copper; these modes are forbidden in the absence of copper. Parameters of the quasi-Raman bands *G* and *D* in optical absorption in the region of carbon–carbon mode vibrational frequencies and the parameters of true Raman bands are compared in the Raman spectra of pure *a*-C:H and in that modified with copper. It is stated that the close coincidence of the frequencies of the true Raman bands in *a*-C:H and quasi-Raman bands in *a*-C:H(Cu) indicates that the interaction of copper atoms with the carbon matrix leaves the graphene rings practically intact and can be regarded as intercalation. To identify the observed quasi-Raman and the satellite bands, correlations between their parameters are considered. The sizes of graphite-like clusters and their dependence on the copper content in the film were evaluated from the ratios between the integrated intensities of *D* and *G* bands. © *2000 MAIK "Nauka/Interperiodica".*

1. INTRODUCTION

Owing to the ability of atoms in hydrogenated amorphous carbon (*a*-C:H) to be in different valence states, the microscopic structure of this material shows a unique capacity for adapting itself, by forming sp^3, sp^2, and sp^1 hybrids, to the introduction of various foreign inclusions. By virtue of this capacity, carbon is an ideal matrix for forming nanocomposites. Of particular interest for a number of recently developed applications is the possibility of introducing the metal nanoclusters into the carbon matrix. Mesoscopic-scale electronic phenomena in systems of this kind could be of interest for nanoelectronics. The research in this field will hopefully make it possible to develop media for information recording and storage, particularly the research into magnetic metal clusters. In connection with this, we should mention recent studies concerned with embedding the metal nanonclusters in carbon [1, 2]. Finally, this material may be of interest for developing low-voltage emitters.

To ensure the successful use of carbon-based nanocomposites, it seems necessary to study the mechanism of interaction between the metal and carbon. As shown previously, the interaction of copper with hexagonal graphene rings in graphite-like clusters manifests itself in the activation of vibrational modes of graphene rings in IR absorption; these modes are absent in the spectra of copper-free *a*-C:H for reasons of symmetry [3]. This phenomenon indicates that, while leaving practically intact the graphene rings, the interaction between copper atoms and the graphite-like constituent of *a*-C:H changes the symmetry of distribution of electron density in these rings [4]. As a result, pseudo-Raman bands *G* and *D* appear in the optical spectrum. The positions of these bands in true Raman spectra of graphite [5, 6] and amorphous carbon is well known [7, 8] and they can be used to characterize the interaction of metals with the carbon skeleton of *a*-C:H.

In this paper, we report the results obtained in a simultaneous study of Raman bands in the Raman spectra and pseudo-Raman bands in optical spectra in the frequency range of C–C bond vibrations in *a*-C:H modified with copper.

2. EXPERIMENTAL

a-C:H(Cu) films were grown by dc magnetron co-sputtering of planar graphite and copper targets in argon–hydrogen plasma (80% Ar + 20% H_2). The introduced copper concentration was varied by changing the area ratio of the targets. The atomic ratio of copper and carbon in the grown films was determined by Rutherford backscattering of 1 MeV protons [9].

The films were deposited on KDB-20 (*p*-Si, ρ = 20 Ω cm) single-crystal substrates with [100] orientation, and preheated to 200°C. The initial vacuum in the sputtering chamber was at the level of the residual pressure (10^{-6} Torr); the sputtering was carried out in a working gas flow at a pressure of 10^{-2} Torr and ion current density of 0.1 A/cm^2. Under these conditions, the growth rate of *a*-C:H(Cu) films varied within 5–7 nm/min, depending on the copper target area.

The Raman scattering was studied using a SPEX Ramolog spectrometer with excitation by an argon-ion laser (487.9 nm, 50 mW). The scattering was measured

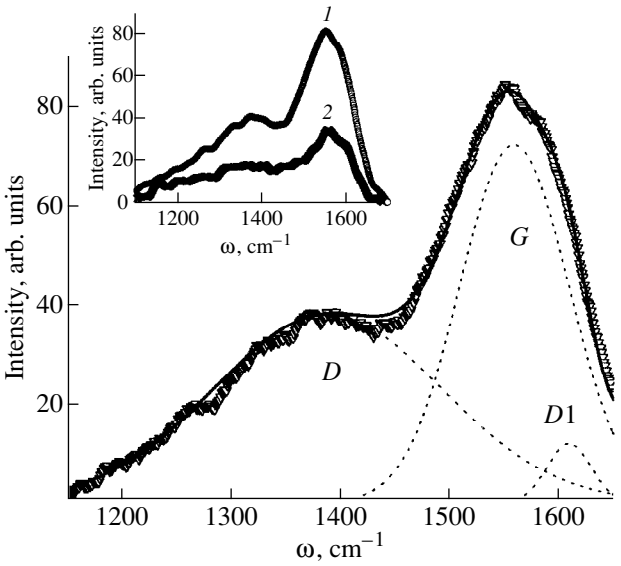

Fig. 1. Raman spectrum (points), its decomposition into Gaussian components (dashed lines), and the overall envelope of the Gaussian components (solid line) for an *a*-C:H(Cu) sample of composition [Cu]/[C] = 0.62. Insert: spectra of samples with [Cu]/[C] = (*1*) 0.62 and (*2*) 0.90.

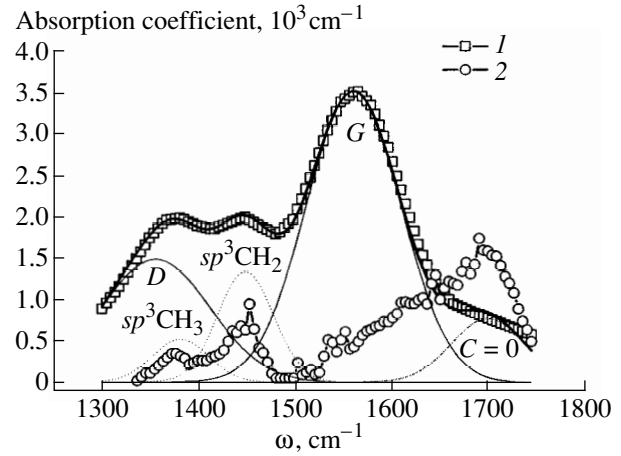

Fig. 2. Absorption spectra of (*2*) *a*-C:H and (*1*) *a*-C:H(Cu) ([Cu]/[C] = 0.62) films with decomposition into Gaussian components.

in reflection configuration with a spectral slit of 5.5 cm^{-1}.

The optical absorption was studied with a Specord 75IR double-beam IR spectrometer with a resolution of ~2 cm^{-1} in the region of the stretching vibrations of the carbon–carbon bonds and the bending vibrations of the carbon–hydrogen bonds in *a*-C:H.

3. RESULTS

3.1. Raman Scattering

Figure 1 shows a Raman spectrum after subtraction of the luminescent background for an *a*-C:H(Cu) sample with the atomic concentration ratio [Cu]/[C] = 0.62. High-intensity photoluminescence (PL) from the grown films gives no way of recording a Raman spectrum for an unmodified sample. The inset in Fig. 1 shows that an increase in the copper concentration by a factor of 1.5 does not affect the position and shape of the most intense high-frequency line, but the low-frequency line can no longer be distinguished against the background. Apparently, the introduction of copper into the carbon matrix not only suppresses the PL, but also enhances the loss of the scattering signal in the spectral range of interest. We can describe the experimental Raman spectrum for the *a*-C:H(Cu) sample with [Cu]/[C] = 0.62 by decomposing it into Gaussian components (Fig. 1, dashed lines). It can be seen that a reasonable agreement of the overall envelope of the components (solid line) with the experimental curve can be achieved upon decomposition into three Gaussian lines with the parameters (peak frequency ω, full width at half-maximum Δω, and area under the curve S^*) given in frequency units in the table.

The bands *G* and *D* in *a*-C:H(Cu) can be correlated with the Raman bands *G* and *D* for finely divided graphite [6], even though a shift of the band *G* by ~20–25 cm^{-1} to lower frequencies is noteworthy. However, such a strong shift of the *G* and *D* bands has been observed previously in amorphous carbon [7, 8] and, therefore, can hardly be ascribed to the effect of copper. The presence in the spectrum of another band (1620 cm^{-1}) characteristic of scattering by small fragments of graphene sheets [6] also follows, with a somewhat lower confidence level, from Fig. 1 (*D*1 band). The ratio of the integrated intensities of the *D* and *G* bands is 1.2, which corresponds, according to Tuinstra and Koenig [5], to an average graphene sheet size of ~3.5 nm.

3.2. IR Absorption

Figure 2 shows portions of absorption spectra of *a*-C:H and *a*-C:H(Cu) with [Cu]/[C] = 0.62 in the region of the stretching vibrations of C–C bonds and the bending vibrations of C–H bonds. It can be seen that the experimental spectrum of *a*-C:H(Cu) is well described by a curve (thick solid line) representing a superposition (thin lines) of five Gaussian components. Three bands in the *a*-C:H(Cu) spectrum corresponding to the vibrational modes of sp^3CH_2, sp^3CH_3, and C=O coincide in frequency with bands in the *a*-C:H spectrum, but the two most intense bands arise only upon modification with copper. These have frequencies close to the position of the *G* and *D* bands in the Raman spectra in Fig. 1 and, therefore, are designated similarly. Thus, the direct comparison of the spectra of *a*-C:H and *a*-C:H(Cu) in Fig. 2, and also the comparison of Figs. 1 and 2, show that modification of amorphous hydrogenated carbon films with copper activates Raman vibrational modes in IR spectra, as reported in our previous

publication [3]. These bands can be conveniently named quasi-Raman bands, in contrast with the true Raman bands *D* and *G* observed in Raman spectra of *a*-C:H which are identical to the Raman bands *D* and *G* of graphite. It is commonly believed that these bands are associated with the optically forbidden for symmetry reasons (albeit Raman-active) vibrational modes E_{2g} of graphene sheets (*G* band) and with the edge modes (*D* band) which owe their origin to the finite size of graphene sheets in graphite-like fragments [6–8].

In order to study the parameters of the quasi-Raman bands in relation to copper concentration, we measured the absorption spectra for *a*-C:H(Cu) films of several compositions in the range of atomic ratios [Cu]/[C] = 0.62–1.3. The composition range studied was limited from the low-concentration side by the experimental conditions. Since, at lower concentrations, the film growth rate decreases substantially, the film thickness necessary for sufficiently accurate spectral measurements (~2 μm) cannot be obtained during the maximum possible period of stable reactor operation (~5 h). With increasing copper content, the inhomogeneous structure of the quasi-Raman *G* band becomes more pronounced, as follows from the spectrum in Fig. 3 for a film with the composition [Cu]/[C] = 1.3. It can be seen that the shape of the broad quasi-Raman band is now well described by merely three Gaussian bands *D*1, *GG*, and *G*, with the position of the resolved Gaussian band *G* coinciding with the frequency of the true Raman band *G* in Fig. 1.

Despite the fact that the procedure for the decomposition of quasi-Raman spectra into Gaussian lines produces rather ambiguous results, some spectral features are observed for all the samples studied. This primarily refers to the bands *D* and *G* appearing in all the spectra without exception. Analysis also reveals in all cases the bands *GG* and *D*1. The *D*1 band coincides in frequency with the similar true Raman band in the spectrum in Fig. 1, which is also observed in finely dispersed graphite and, as suggested in [6], has its origin in edge phonon modes of nanosized fragments of graphene sheets, which are even smaller (<10 nm [6]) than those giving rise to the *D* band. The quasi-Raman band *GG* is close in frequency to the true Raman band *G* (1575–1583 cm^{-1}) characteristic of an ideal graphite [6]. At the same time, the frequency of the quasi-Raman band *G* is well within the range of true Raman frequencies of *a*-C:H [6, 7]. We believe that it is the appearance of the *GG* bands in the spectra that distinguishes *a*-C:H(Cu) from *a*-C:H and will discuss this difference below.

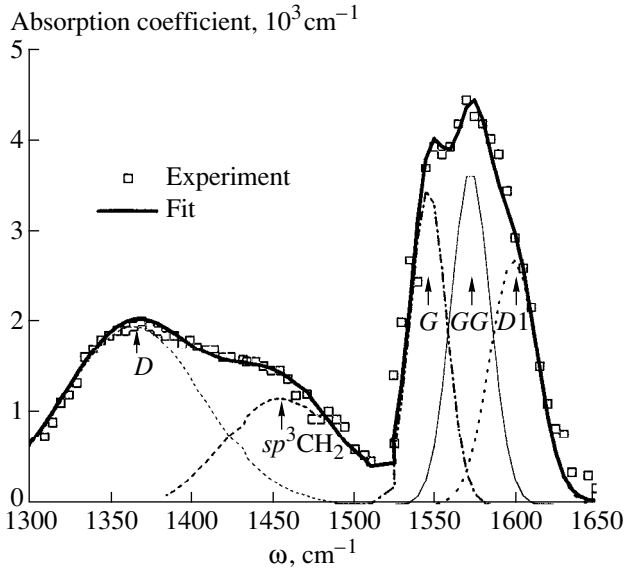

Fig. 3. Absorption spectrum of *a*-C:H(Cu) film with the composition [Cu]/[C] = 1.3; decomposition into Gaussian components is shown.

4. DISCUSSION

4.1. Activation of Quasi-Raman Bands

Quasi-Raman bands are activated as a result of *a*-C:H modification with copper at frequencies which are almost independent of the introduced copper concentration, as follows from the data in Fig. 4. Mention can be made of a tendency for the averaged frequency of the *G* band to increase with increasing copper concentration, even though this shift is on the order of the rms deviation of experimental points from the approximating straight line. The activation of the quasi-Raman bands can be attributed to the interaction of copper atoms with hexagonal graphene rings. At the same time, the noticeable rise in absorption by sp^3CH_2- and sp^3CH_3-groups in *a*-C:H(Cu), compared with that in *a*-C:H, may indicate a direct bonding of these groups to graphene rings. Another situation takes place in the case of C=O groups, as suggested by the comparison of the absorption coefficients associated with these groups in the *a*-C:H and *a*-C:H(Cu) spectra in Fig. 2. Presumably, these groups are not linked directly to graphite-like fragments, being attached to the olefin components of the *a*-C:H structure as a result of its reaction with residual oxygen. In addition, it is evidenced by the absorption coefficient in the C=O band that copper takes up oxygen from these groups. This interaction yields cuprous oxide Cu_2O whose characteristic vibrational frequency is observed in the IR spectrum, as shown in Fig. 5. Comparison of the quasi-Raman band frequencies in the absorption spectra of *a*-C:H(Cu)

Parameters of Gaussian lines into which the spectrum in Fig. 1 is decomposed

Band	ω, cm^{-1}	Δω, cm^{-1}	*S**, cm^{-1}
D	1370 ± 10	250	10000
G	1554 ± 5	105	8150
*D*1	1610 ± 10	45	600

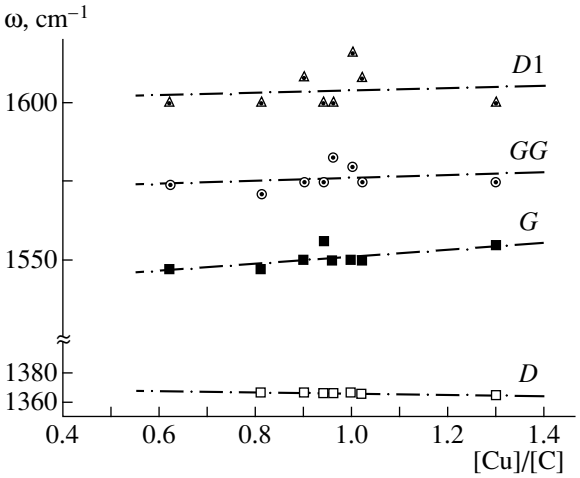

Fig. 4. Frequencies of quasi-Raman bands vs. copper content.

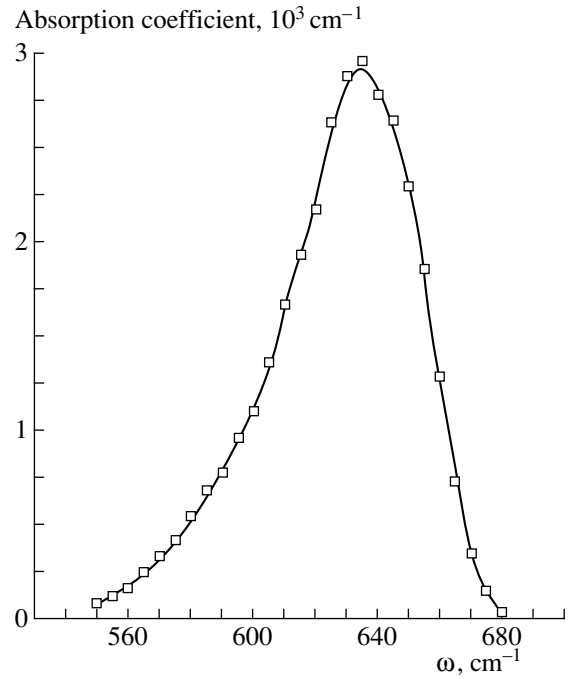

Fig. 5. Cu_2O-related absorption band for *a*-C:H(Cu) film with [Cu]/[C] = 1.3.

with true Raman bands in the scattering spectra (see Fig. 4 and table) reveals their coincidence. This means that the interaction of copper atoms with the graphite-like component does not destroy the graphene rings, but only changes the symmetry of the electron-density distribution [4]. This fact suggests that in one form or another, intercalation of graphite-like fragments with copper occurs. However, it should be noted that the boundary of graphite-like and copper nanoclusters could give rise to similar phenomena. Figure 3 also shows that the spectrum of quasi-Raman bands contains an additional *GG* band, compared with the Raman spectrum in Fig. 1. We note that the Raman band *G* is sufficiently broad to suppose that in this case, too, there is a contribution from the *GG* band. However, while the *D*1 band discernible in Fig. 1 appears in the films even at the lowest copper concentrations, the *GG* band (Fig. 3) characteristic of graphite [6] is more evident at higher copper concentrations, as indicated by the comparison of integrated intensities of the Gaussian components of *G* and *GG* in Fig. 6a. This fact can be understood as follows: when present in sufficiently high concentration, copper, when forming copper clusters, favors the formation of a nearly perfect graphite-like phase on their periphery, which is indicated by the close agreement between frequencies of the *GG* band and the true Raman band *G* of graphite. This conclusion is consistent with the data [1, 2] indicating that a graphite shell appears on the surface of metal nanoclusters, which means in this case that copper nanoclusters are embedded in a carbon shell. Thus, we tend to ascribe the *GG* band to the activation of quasi-Raman modes in the optical absorption by the graphite sheath of copper nanoclusters. The *G* band is related to graphite-like nanoclusters and exhibits in *a*-C:H [in *a*-C:H(Cu) in our case] a substantial shift to lower frequencies compared with the corresponding band in perfect graphite (up to 60 cm^{-1}) [7, 8]. As shown by calculations [10], the disruption of the long-range order in valence angles of amorphous carbon, compared with the crystalline carbon, may indeed cause the frequencies of the Raman bands *G* and *D* to become much lower.

4.2. The Shape of Quasi-Raman Bands

In all the cases encountered in this study, the Gaussian components were the best approximation for decomposing the experimental IR spectra. This seems to be quite natural since the Gaussian component corresponds to inhomogeneous line broadening, characteristic in our case of the amorphous structure of *a*-C:H. In what follows, we restrict ourselves to the analysis of only the *G* and *D* bands, i.e., to the absorption by the graphite component, even though the spectrum also contains a contribution from polymer-like components.

Analysis of the shape of the spectral bands in relation to the amount of introduced copper is strongly hindered by the poor accuracy with which all the parameters of the quasi-Raman bands, except their position, are determined. It is currently impossible to determine to what extent this can be attributed to inaccuracies of the procedure for their determination and to what extent to the uncertainty inherent in quasi-Raman bands by virtue of the complicated mechanism of their appearance in the amorphous structure. Nevertheless, to verify the assumptions concerning the nature of the observed bands even in the current stage of the study, an attempt was made to establish certain correlations between the band parameters. Let us consider the dependence of the intensity ratio of the *G* and *GG* bands on the concentra-

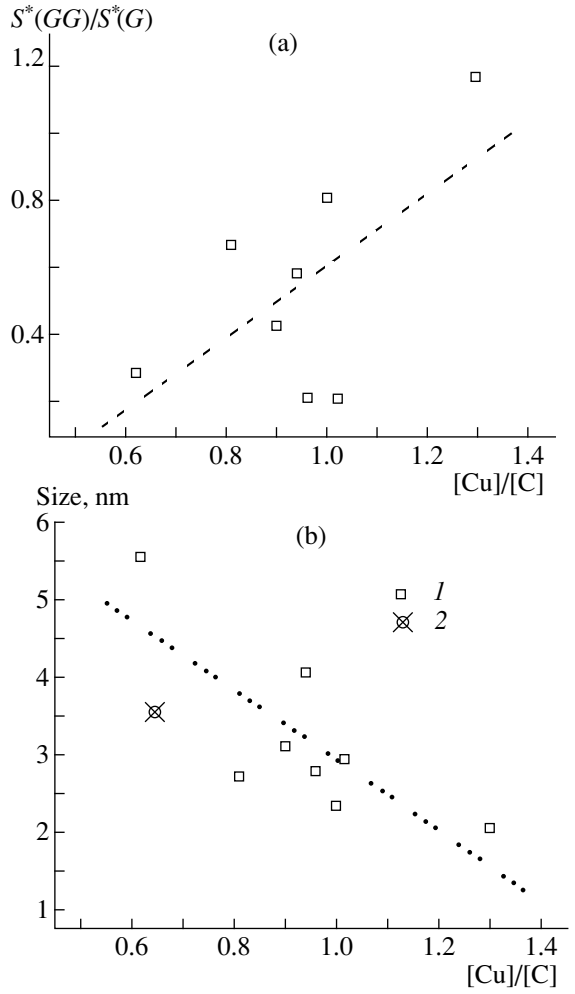

Fig. 6. (a) Ratio of integrated intensities of the *GG* and *G* bands $S^*(GG)/S^*(G)$ at varied content of copper and (b) size of graphite-like nanoclusters vs. copper content according to (*1*) IR absorption and (*2*) Raman scattering data.

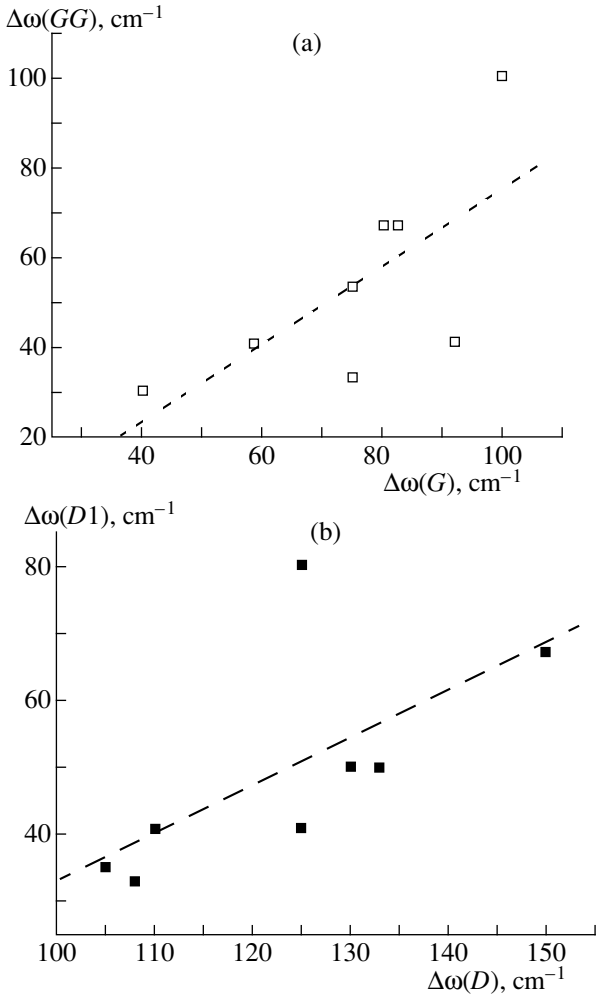

Fig. 7. Bandwidths $\Delta\omega$ of (a) *GG* and *G* bands and (b) *D*1 and *D* bands for varied copper content.

tion of copper introduced into a film (see Fig. 6a). It can be seen that, as the content of copper becomes higher, the relative intensity of the *GG* band tends to increase, which would be expected to occur with an increasing volume fraction of copper nanoclusters due to the above assumption about the nature of this band. The existence of a correlation between the widths of the Gaussian lines in the same bands is illustrated in Fig. 7a. This possibly reflects the commonness of their physical nature. Figure 7b demonstrates a similar relation between the widths of the Gaussian bands *D* and *D*1. Here, it is noteworthy that the width of the *D*1 band increases more rapidly than that of the *D* band, since the former is related, as assumed above, to finer graphene fragments. It seems of interest to compare the widths of the Raman and quasi-Raman bands in *a*-C:H(Cu) films of the composition [Cu]/[C] = 0.62 (see Figs. 1, 2). It is readily seen that the *G* band widths coincide quite satisfactorily, whereas the true Raman band *D* is approximately 2–2.5 times broader than the quasi-Raman band. It is of particular interest to establish a correlation between the intensities of the *G* and *D* bands. It is known that the intensity ratio can be used to evaluate the sizes of graphite-like structural units; therefore, let us consider it in more detail.

4.3 Size of Graphite-like Clusters

The size of graphite-like nanofragments can be evaluated using the Tuinstra and Koenig (TK) empirical relation between the nanofragment size and the intensity ratio of the *G* and *D* bands [5]. It is to be recognized that the relation was originally established for finely divided graphite and its validity for *a*-C:H remains problematic. However, we verify the applicability of the TK relation to quasi-Raman bands by comparing the results obtained in this case with independent estimates of the size of graphene sheet fragments and published data for *a*-C:H.

Figure 6b shows the results obtained by applying the TK procedure to the quasi-Raman bands *G* and *D* for films with varied copper content. Despite the considerable inaccuracy of the estimates, a tendency is distinguishable for the graphite-like clusters to become smaller with increasing copper content in the films. The difference between the sizes obtained for the Raman (point *2*) and quasi-Raman (point *1* at the same concentration of copper) bands is beyond the error limits. It is more important, however, that in both cases the sizes of graphite fragments exceed severalfold the average size of graphite-like nanoclusters, determined directly using electron microscopy [11] or optical measurements [12]. It should be noted here that the results shown in Fig. 6b are in reasonable agreement with the data [8] for *a*-C:H.

The unrealistically large cluster sizes obtained by the procedure described in [5] for the amorphous structure of *a*-C:H are presumably due to the fact that the *D* band in finely divided graphite (for which material the technique [5] was developed) is formed by edge vibration modes, while in *a*-C:H their density greatly decreases owing to passivation of graphene surfaces by hydrogen. Finally, the difference between estimates obtained by different methods may be due to the possible interaction in *a*-C:H(Cu) of photons with phonon modes of imperfect and, therefore, nonplanar graphene sheets having an effectively increased surface area compared with their plane projections observed with an electron microscope. It should be noted here that the cluster sizes determined using an electron microscope deviate from the values obtained by the TK method for *a*-C:H to the same extent as for some types of graphite, but in the opposite direction [8].

The dependence of the cluster size on copper concentration may be due to the preferential interaction of copper at low concentrations with larger graphene fragments for which the ratio between the intensities of the *D* to *G* bands is small. As the copper concentration increases, only smaller clusters, for which this ratio is larger, become available. To be sure, the destructive effect of copper atoms is also possible.

In discussing the above estimates of the sizes of graphene fragments in the *a*-C:H structure, a question arises as to whether the decomposition of quasi-Raman bands into the components *G*, *GG*, and *D*1 is correct. A certain ambiguity in this procedure has already been mentioned above. However, a possible argument in favor is that, without such decomposition, the quasi-Raman band *G* would be unreasonably broad from the standpoint of evaluating the graphene fragment sizes and in comparison with the true Raman band.

5. CONCLUSION

It is shown by the example of *a*-C:H(Cu), in more detail than has been previously achieved, that modification of *a*-C:H films with metal leads to the observation that quasi-Raman bands in many respects similar to the true Raman bands appear in IR absorption spectra. At a sufficiently high content of copper, when the intensity of the Raman bands decreases, a study of vibrational modes by IR absorption spectroscopy can be more versatile. Investigation of Raman bands in amorphous carbon modified with various metals will enable a quantitative study of the interaction of metal clusters embedded in a carbon matrix with their surroundings [13].

ACKNOWLEDGMENTS

We thank I.I. Novak for Raman scattering measurements in the framework of a program supported by the Russian Foundation for Basic Research (project no. 96-03-40010) and V.M. Lebedev for the Rutherford backscattering measurements.

This study was supported by the Russian Foundation for Basic Research (project nos. 00-02-17004 and 00-02-16994).

REFERENCES

1. J. Jiao and S. Seraphin, J. Appl. Phys. **83** (5), 2442 (1998).
2. T. Cabioc'h, A. Naudon, M. Jaouen, *et al.*, Philos. Mag. **79** (3), 501 (1999).
3. V. I. Ivanov-Omskiĭ and G. S. Frolova, Zh. Tekh. Fiz. **65** (9), 186 (1995) [Tech. Phys. **40**, 966 (1995)].
4. V. I. Ivanov-Omskiĭ and É. A. Smorgonskaya, Fiz. Tverd. Tela (St. Petersburg) **41** (5), 868 (1999) [Phys. Solid State **41**, 786 (1999)].
5. F. Tuinstra and J. L. Koenig, J. Chem. Phys. **53** (3), 1126 (1970).
6. H. Wilhelm, M. Lelaurain, E. McRae, and B. Humbert, J. Appl. Phys. **84** (12), 6552 (1998).
7. J. Schwan, S. Ulrich, V. Batori, *et al.*, J. Appl. Phys. **80** (1), 440 (1996).
8. M. A. Tamor and W. C. Vassell, J. Appl. Phys. **76** (6), 3823 (1994).
9. T. K. Zvonareva, V. M. Lebedev, T. A. Polyanskaya, *et al.*, Fiz. Tekh. Poluprovodn. (St. Petersburg) **34** (9), 135 (2000) [Semiconductors **34**, 1094 (2000)].
10. D. Beeman, J. Silverman, R. Lynds, and M. R. Anderson, Phys. Rev. B **30**, 870 (1984).
11. V. I. Ivanov-Omskii, A. B. Lodygin, A. A. Sitnikova *et al.*, in *Diamond and Diamond-like Film Applications*, Ed. by P. Gielisse, V. I. Ivanov-Omskii, G. Popovici, and M. Prelas (Technomic Publ., Lancaster, 1998), p. 486.
12. S. G. Yastrebov, V. I. Ivanov-Omskii, V. I. Siklitsky, and A. A. Sitnikova, J. Non-Cryst. Solids **227–230**, 622 (1998).
13. V. I. Ivanov-Omskiĭ and G. S. Frolova, Pis'ma Zh. Tekh. Fiz. **26** (14), 66 (2000) [Tech. Phys. Lett. **26**, 623 (2000)].

Translated by M. Tagirdzhanov

Semiconductors, Vol. 34, No. 12, 2000, pp. 1397–1401. Translated from Fizika i Tekhnika Poluprovodnikov, Vol. 34, No. 12, 2000, pp. 1457–1461.

PHYSICS OF SEMICONDUCTOR DEVICES

On the Internal Quantum Efficiency and Carrier Ejection in InGaAsP/InP-based Quantum-Well Lasers

A. Yu. Leshko, A. V. Lyutetskiĭ, N. A. Pikhtin, G. V. Skrynnikov, Z. N. Sokolova, I. S. Tarasov, and N. V. Fetisova

Ioffe Physicotechnical Institute, Russian Academy of Sciences, Politekhnicheskaya ul. 26, St. Petersburg, 194021 Russia

Submitted June 16, 2000; accepted for publication June 21, 2000

Abstract—The optimization of InGaAsP/InP quantum-well laser heterostructures that had various configurations and emitted in the wavelength range from 1.26 up to 1.55 μm was carried out with the aim of maximizing the internal quantum efficiency and output optical power. It was experimentally shown that the heterolasers based on the laser structure with a broadened three-step waveguide have the highest quantum efficiency of stimulated radiation. In heterolasers of the suggested configuration, a decrease in the electron ejection out of the active region into the waveguide was observed. The power of the optical radiation of 4.2 W in a continuous-wave lasing mode was obtained in laser diodes with a mesa-stripe width of 100 μm. The quantum efficiency was 85% for the internal optical losses of 3.6 cm^{-1}. © *2000 MAIK "Nauka/Interperiodica".*

INTRODUCTION

In the beginning of the 1990s, an interest in quantum-well (QW) InGaAsP/InP-based lasers emitting at the wavelength $\lambda = 1.3$ μm was aroused. This interest was caused by the efforts to lower the temperature sensitivity of such lasers [1–3]. These studies showed that an internal quantum efficiency close to 100% in the lasing mode [4, 5] could be attained in the QW InGaAsP/InP-based lasers, and that an increase in parameter T_0 above 90 K was impossible at room temperature [6, 7].

In recent years, an interest in high-power semiconductor lasers emitting at wavelengths λ in the range of 1.3–1.55 μm has been regenerated [8]. The peak power in wide mesa-stripe lasers depends on the internal optical losses [9] of the temperature dependence of a differential quantum efficiency [10, 11] and on the value of the internal quantum efficiency in the lasing mode [11]. Irrespective of the production technology and semiconductor materials used in the separate-confinement lasers, the introduction of a broadened waveguide results in the lowering of the internal quantum efficiency [8, 10, 11]. In the InGaAsP/InP-based lasers with a separate confinement and broadened waveguide, which possesses a high temperature sensitivity, the internal quantum efficiency does not exceed (70 ± 5)% [8, 10, 12]. Therefore, the achievement of an internal quantum efficiency close to 100% in such lasers is an extremely topical problem.

We studied the properties and characteristics of semiconductor quantum-well InGaAsP/InP-based lasers with a separate confinement and a wide mesa-stripe contact and report the results in this paper. The structures of various configurations were prepared by vapor-phase epitaxy from the metalorganic compounds (MOC-hydride epitaxy) [12]. The optimization of laser heterostructures was carried out with the aim of attaining the maximum values of internal quantum efficiency and output optical power in the continuous-wave lasing mode.

EXPERIMENTAL

The parameters of laser structures are given in the table, and a schematic representation of the energy band diagram of the heterostructures studied by us is shown in Fig. 1. The waveguide layer thicknesses (W, W_1, and W_2) and the corresponding band gaps (E_g^w, E_g^{w1}, and E_g^{w2}) were varied in the structures, as well as the barrier band gap (E_g^b) between the QWs. The number of QWs varied from 1 up to 4, and their width, from 35 to 70 Å. The barrier width between the QWs was 150–250 Å. The laser diodes with a mesa-stripe contact width of 100 μm were all made of laser heterostructures. The electroluminescence (EL) spectra were studied in the laser diodes in a spontaneous incoherent mode of radiation under continuous and pulsed current pumping. The spectra of spontaneous EL of laser diodes were studied in the direction perpendicular to the Fabry–Perot cavity axis. Such an experimental arrangement allowed us to lower the fraction of the coherent radiation in the spectrum to a considerable extent [13].

EXPERIMENTAL RESULTS

Four emission bands were observed in the spontaneous EL spectra of laser diodes made of the A and C type

1063-7826/00/3412-1397$20.00

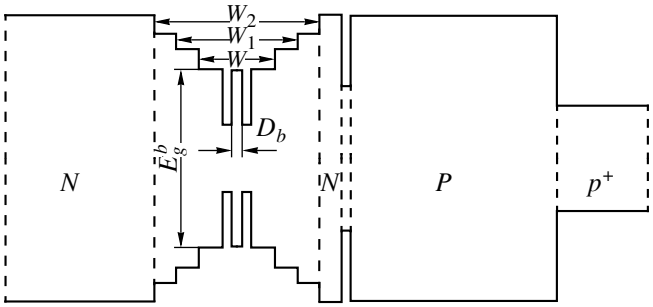

Fig. 1. Schematic representation of a laser heterostructure. W, W_1, and W_2 are the thicknesses of waveguide layers; D_b is the barrier thickness; and E_g^b is the band gap of the barrier between the QWs.

heterostructures (Fig. 2). Band *1* is related to the radiative recombination in the layer of an active region. The emission of band *4* is connected with the recombination of carriers in a waveguide layer. Band *2*, which is a short wavelength shoulder of band *1*, is related to the radiative transitions of electrons from the waveguide (w) to the first hole level (1h) (Fig. 3). Band *3* is connected with the radiative transitions of electrons from the waveguide to the second level of heavy holes (2h) and the first level of light holes (1l), and also with the transitions from the first electron level (1c) to 1l.

The laser heterostructures of A and C types had two strained QWs 50 Å thick, a waveguide layer with the thickness W = 0.75 μm (structure A) or W = 1 μm (structure C) with the constant band gap (E_g^w). The compression strain in the QW of structure C (λ = 1.55 μm), which is caused by the lattice-parameter mismatch, was 0.87%. In this structure, the splitting of the heavy- and light-hole band bottoms, that was evaluated according to the method suggested in [14], was equal to 48 meV. It was taken into consideration that, in InGaAsP compounds on the InP substrate, a 1/3 of the total offset of the band gap is accounted for by the conduction band, and 2/3 by the valence band [15] as opposed to the structures on the GaAs substrates, in which this relationship was considered to be inverse. The values of the transition energies calculated (from the transition energy (1c–1h) were (w–1h) 38 meV, (1c–2h) 68 meV, (w–2h) 106 meV, (1c–1l) 110 meV, (1c–3h) 141 meV, (w–1l) 148 meV, and (w–w) 337 meV. The scheme of the radiative transitions in a strained QW in the active region of structure C is shown in Fig. 3. Good agreement is observed between the calculated values of the transition energies (Fig. 3) and the experimentally observed radiative transitions (Fig. 2).

The dependences of radiation intensity (I) for bands *2* and *3* (curve *1*) and band *4* (curve *2*) on the pump-current density j are shown in Fig. 4. The significant feature of these dependences is the increase in the band intensity beyond the lasing threshold ($j > j_{th}$). The increase in the emission intensity above the lasing threshold is indicative of an increase in the injected carrier concentration in the waveguide of the laser heterostructure. This phenomenon was observed by us for the first time in the laser structures produced by a modified liquid-phase epitaxy (LPE) [13, 16]. Starting from the specificity of the laser heterostructures obtained by LPE, we have explained this phenomenon by the inhomogeneous broadening of the gain band width, which arises due to the inhomogeneity of the active region layer in thickness and to the spinodal decomposition of InGaAsP solid solutions, the latter being inherent in LPE [16, 17]. The structures of A and C types under study, which were prepared by the MOS-hydride epitaxy, in our opinion, are free of the short-comings mentioned above.

Parameters of laser structures

Type	Number of QWs	η_i	E_g^b, eV	E_g^w, eV	E_g^{w1}, eV	E_g^{w2}, eV	λ, μm	Substrate	Sample no.
A	2	0.68	1.19	1.19	–	–	1.26	InP	KP-938
C	2	0.67	1.13	1.13	–	–	1.55	InP	KP-853
D	1	0.95	–	1.44	–	–	1.03	GaAs	K-1457
F	1	0.98	–	1.65	–	–	0.975	GaAs	K-1340
G	2	0.71	1.03	1.17	–	–	1.53	InP	KP-916
H	4	0.68	1.03	1.17	–	–	1.53	InP	KP-914
J	2	0.85	1.03	1.03	1.13	1.24	1.53	InP	KP-1002

Note: A and C are InGaAsP heterostructures with two strained QWs emitting at wavelengths of 1.26 (A) and 1.55 μm (C). D and F are AlGaAs heterostructures with a single QW of various depths. G and H are InGaAsP heterostructures with two (G) and four (H) QWs emitting at a wavelength of 1.53 μm and having lowered barriers between QWs. J is an InGaAsP heterostructure with a three-step waveguide and two QWs; this heterostructure emits at a wavelength of 1.53 μm. The laser parameters given in the table are as follows: number of QWs; quantum efficiency of a stimulated emission (η_i); the barrier band gap between QWs E_g^b; the band gaps for waveguide layers E_g^w, E_g^{w1}, and E_g^{w2}; the basing wavelength λ; and type of the substrate used.

One should note that bands *2* and *3* were not observed under all pumping levels in the spectra of spontaneous EL of A and C heterostructures studied at liquid-nitrogen temperatures.

The internal quantum efficiency (η_i) was 68% in A and C structures. The value of η_i was defined according to a known formula [18]

$$\eta_d = \eta_i/[1 + \alpha_i L/\ln(1/R)],$$

where η_d are the experimental values of the differential quantum efficiency, α_i are the internal losses in a laser structure with length L, and R is the reflection coefficient for a cleaved cavity facet.

In AlGaAs/GaAs heterostructures (types D and F) formed on a GaAs substrate, the thickness of the waveguide layer was 0.6 μm. The active region consisted of a single QW 70 Å thick. The offset of energy between the active region and the waveguide was 160 meV (structure D) and 255 meV (structure F) in the conduction band of these heterostructures. Emission bands *2* and *3* in the spontaneous EL spectra were not observed in the laser diodes of D and F types under any level of pumping. The internal quantum efficiency of their stimulated radiation was 95% (structure B) and 98% (structure F).

In laser heterostructures with a uniformly broadened waveguide of type G (with two QWs, each 35 Å thick) and type H (with four similar QWs), which have a lowered barrier E_g^b, the emission spectra differed somewhat from those for A and C type structures. Only one emission band *2* was present in the former spectra (see Fig. 2), however, its intensity also increased beyond the lasing threshold. The magnitude of the stimulated internal efficiency in laser diodes made of such structures was 68% (type H) and 71% (type G). Hence, we came to the conclusion that an increase in the total thickness of the active region with barriers up to 650 Å (type G) and a decrease in barrier height by 47 meV (type G and H) do not reduce the carrier ejection out of the active region of a QW heterostructure.

The type J structure was a heterostructure of a separate confinement with a three-step waveguide and two strained QWs 60 Å wide. The band gap of the waveguide w_2 was enhanced up to 1.24 eV, which provided the energy offset in the conduction band between the bottom of the QW and wide-gap waveguide w_2 equal to 145 meV. The thickness of the waveguide layer w_2 was 0.9 μm, the thickness of the waveguide w_1 was 0.36 μm, and that of the waveguide w was 0.12 μm. The distinguishing feature of the spontaneous EL spectra of laser diodes consisting of the type J heterostructure is the absence of bands of emission originating in the waveguides w_1 and w_2 for all levels of pumping. In the laser diodes made of the type J heterostructure, an internal quantum efficiency of the stimulated radiation of 85% was achieved with internal optical losses retained at the level of 3.6 cm^{-1}.

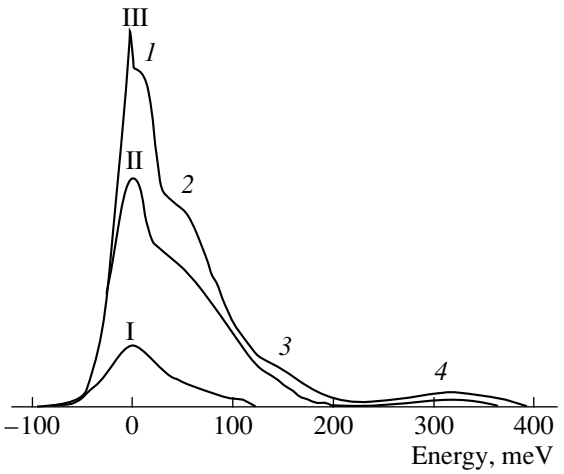

Fig. 2. EL spectra for type C heterostructures for the pump-current density j = (I) 50, (II) 400, and (III) 800A/cm^2. Heterostructures of type A had a similar shape of spectra.

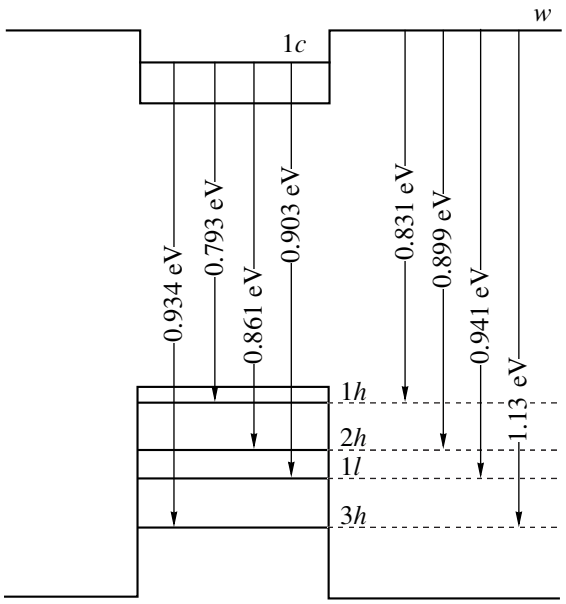

Fig. 3. The schematic of radiation transitions in an InGaAsP QW of the laser heterostructure of type C.

The optical-power–current characteristic $P(I)$ of a mesa-stripe laser diode made of type J heterostructure with a cavity length of 2700 μm is shown in Fig. 5. The reflectivity of the output mirror of the Fabry–Perot cavity was reduced to 5%, and a dielectric mirror with a reflection coefficient larger than 95% was deposited at the opposite end. The optical-power–current characteristics were measured at a constant temperature of 10°C of heat sink and laser-diode crystal. The highest power reached 4.2 W for a differential quantum efficiency of 35%, which is the best achievement for lasers that have a mesa-stripe of 100 μm and emit at the wavelength of 1.53 μm.

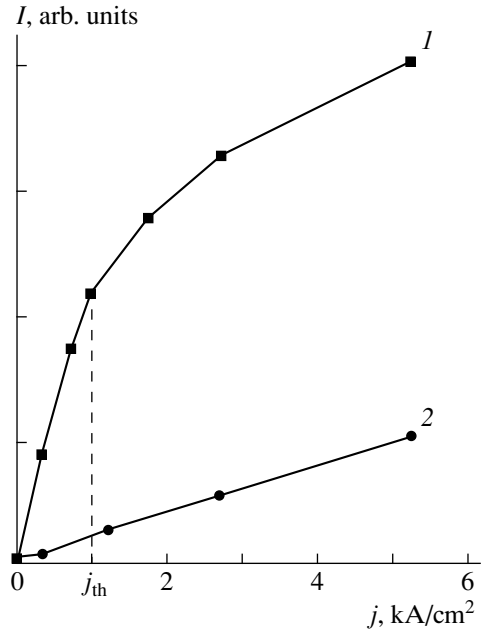

Fig. 4. Dependence of the intensities *I* of (*1*) bands *2* and *3* and (*2*) band *4* on the pump-current density *j*. (*1*) corresponds to the radiation transitions (*w*–1*h*), (*w*–2*h*), (1*c*–1*l*), and (*w*–1*l*); (*2*) corresponds to the radiative transitions in the waveguide. j_{th} is the threshold-current density.

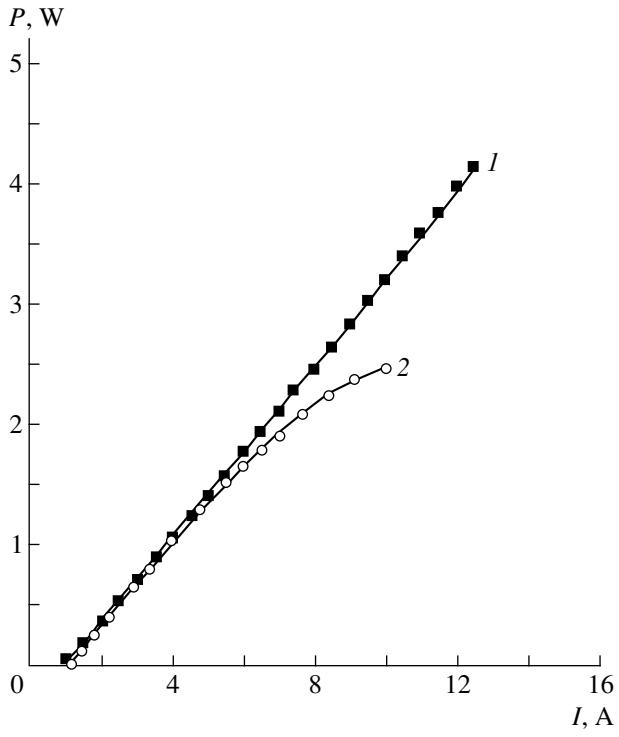

Fig. 5. Optical-power–current characteristic *P*(*I*) of the laser diode based on a heterostructure with a three-step broadened waveguide at the constant temperature 10 °C of (*1*) the laser crystal and (*2*) the heat sink.

DISCUSSION OF THE RESULTS

Structures A and C, which have bands *2* and *3* in the EL spectrum, differ from structures D and F by the energy offset within the conduction band. It was taken into account that, in InGaAsP solid solutions on the InP substrate (as opposed to the GaAs substrate), 1/3 of the total offset of the band gap is due to the conduction band and 2/3 is due to the valence band [15]. In the A and C type structures, the magnitude of the offset in the conduction band is 65–105 meV, and in the D and F type structures it is 160–255 meV. In addition to the difference in the depth of QWs for electrons, the epilayers of InGaAsP heterostructures have an electron density of states which is lower by a factor of 2 in comparison with AlGaAs epilayers. This causes the ejection of the carriers injected into waveguide layers in A and C structures. However, due to the strong localization of holes in the active region, an additional potential barrier appears in the conduction band, which produces a Coulomb potential well for electrons. The shape of the well is determined from the solution of the Poisson equation [19, 20]. The electrons ejected into a waveguide are partially localized in such a potential well; under the action of the space-charge field, the delocalized carriers move towards the emitter, where they recombine (mainly nonradiatively). A certain number of carriers recombine radiatively, which manifests itself in a linear dependence of the intensity of the waveguide-layer EL (Fig. 2, band *4*) on the pump current (Fig. 4).

In the structures with a three-step broadened waveguide of type J, the magnitude of the offset in the conduction band was enhanced up to 145 meV. Therefore, the fraction of charge carriers injected into the waveguide layer turned out to be significantly reduced. The magnitude of the stimulated quantum efficiency in laser diodes made of type J heterostructure increased up to 85%.

One should note that the extension of the emission spectra to shorter wavelengths under high levels of excitation was observed in [21] in the InGaAs/GaAs QW structures, though, in the system in [21], the ratio of the energy offsets in the conduction and valence bands was 0.57–0.43 [21].

CONCLUSION

In semiconductor QW InGaAsP/InP-based lasers with separate confinement and a broadened waveguide, a lowering of the stimulated quantum efficiency is usually observed. This is connected with the presence of additional loss of nonequilibrium carriers, which is retained beyond the lasing threshold. It was experimentally established that ejection of electrons from the active region into the waveguide is one of the causes of the above. The ejected electrons are localized in the Coulomb potential well, which appears due to the attraction of holes that are in a deep QW of the valence band. The delocalized carriers recombine partially radi-

atively in the waveguide layer and partially nonradiatively at the boundary with the emitter. It is shown that the ejection of the carriers can be reduced by using the broadening of the wide-gap part of the stepped waveguide. To reduce the penetration of the electromagnetic field into emitters, where losses are highest, it is necessary to broaden the narrow-gap parts of a waveguide. In the laser diodes based on the heterostructure of type J, a stimulated quantum efficiency of 85% was attained for internal optical losses of 3.6 cm^{-1}, which allowed an attainment of optical emission power of 4.2 W in a continuous-wave lasing mode.

ACKNOWLEDGMENTS

We are grateful to our colleagues E.G. Golikova, T.N. Drokina, N.F. Kadoshchuk, I.A. Kochnev, V.A. Kureshov, E.I. Kukhareva, and Yu.A. Ryaboshtan for their help with producing of heterostructures and laser diodes.

This study was supported by the Russian Foundation for Basic Research (project no. 98-02-18266) and by the Program of Ministry of Sciences of Russian Federation "Physics of Solid-State Nanostructures," code "Kvint."

REFERENCES

1. W. T. Tsang, F. S. Choa, M. C. Wu, *et al.*, Appl. Phys. Lett. **58**, 2610 (1991).
2. T. Yamamoto, H. Nobuhara, K. Tanaka, *et al.*, IEEE J. Quantum Electron. **QE-29**, 1560 (1993).
3. J. S. Osinski, P. Grodzinski, Y. Zou, *et al.*, IEEE Photonics Technol. Lett. **4**, 23 (1992).
4. A. Kasukava, I. J. Murgatroyd, I. Imadjo, *et al.*, Jpn. J. Appl. Phys. **28**, L661 (1989).
5. A. Kasukava, T. Namegaya, N. Iwai, *et al.*, IEEE Photonics Technol. Lett. **6**, 15 (1994).
6. H. Sugiura, Y. Noguchi, R. Iga, *et al.*, Appl. Phys. Lett. **61**, 318 (1992).
7. T. Kunii, Y. Matsui, I. Katoh, and T. Kamidjoh, Electron. Lett. **31**, 282 (1995).
8. D. Z. Garbuzov, L. Xu, S. R. Forest, *et al.*, Electron. Lett. **32**, 1717 (1996).
9. J. Wang, B. Smith, X. Xie, *et al.*, Appl. Phys. Lett. **74**, 1525 (1999).
10. E. G. Golikova, V. A. Kureshov, A. Yu. Leshko, *et al.*, Fiz. Tekh. Poluprovodn. (St. Petersburg) **34**, 886 (2000) [Semiconductors **34**, 853 (2000)].
11. M. R. Gokhal, J. C. Dries, P. V. Studenkov, *et al.*, IEEE J. Quantum Electron. **QE-33**, 2266 (1997).
12. E. G. Golikova, V. A. Gorbylev, N. Yu. Davidyuk, *et al.*, Pis'ma Zh. Tekh. Fiz. **26**, 5 (2000) [Tech. Phys. Lett. **26**, 225 (2000)].
13. D. Z. Garbuzov, A. V. Ovchinnikov, N. A. Pikhtin, *et al.*, Fiz. Tekh. Poluprovodn. (Leningrad) **25**, 929 (1991) [Sov. Phys. Semicond. **25**, 560 (1991)].
14. S. L. Chuang, Phys. Rev. B **43**, 9649 (1991).
15. S. Adachi, *Physical Properties of III–V Semiconductor Compounds* (Wiley, New York, 1992).
16. N. A. Pikhtin, I. S. Tarasov, and M. A. Ivanov, Fiz. Tekh. Poluprovodn. (St. Petersburg) **28**, 1983 (1994) [Semiconductors **28**, 1094 (1994)].
17. L. S. Vavilova, A. V. Ivanova, V. A. Kapitonov, *et al.*, Fiz. Tekh. Poluprovodn. (St. Petersburg) **32**, 658 (1998) [Semiconductors **32**, 590 (1998)].
18. H. C. Casey, Jr. and M. B. Panish, *Heterostructure Lasers* (Academic, New York, 1978; Mir, Moscow, 1981).
19. M. Silver and E. P. O'Reilly, IEEE J. Quantum Electron. **QE-30**, 547 (1994).
20. Z. N. Sokolova, D. A. Vinokurov, I. S. Tarasov, *et al.*, Fiz. Tekh. Poluprovodn. (St. Petersburg) **33**, 1105 (1999) [Semiconductors **33**, 1007 (1999)].
21. P. G. Eliseev and I. V. Akimova, Fiz. Tekh. Poluprovodn. (St. Petersburg) **32**, 472 (1998) [Semiconductors **32**, 423 (1998)].

Translated by T. Galkina

Semiconductors, Vol. 34, No. 12, 2000, pp. 1402–1405. Translated from Fizika i Tekhnika Poluprovodnikov, Vol. 34, No. 12, 2000, pp. 1462–1467.

PHYSICS OF SEMICONDUCTOR DEVICES

Long-wavelength Light-Emitting Diodes (λ = 3.4–3.9 μm) Based on InAsSb/InAs Heterostructures Grown by Vapor-Phase Epitaxy

N. V. Zotova, S. S. Kizhaev*, S. S. Molchanov, T. B. Popova, and Yu. P. Yakovlev

Ioffe Physicotechnical Institute, Russian Academy of Sciences, Politekhnicheskaya ul. 26, St. Petersburg, 194021 Russia

**e-mail: serguie@mail.ru*

Submitted May 29, 2000; accepted for publication May 30, 2000

Abstract—InAs/$InAs_{0.93}Sb_{0.07}$/InAs heterostructures were grown by metal-organic vapor-phase epitaxy in a horizontal reactor at atmospheric pressure. Based on the obtained structures, light-emitting diodes operating at λ = 3.45 μm (T = 77 K) and λ = 3.95 μm (T = 300 K) were fabricated. The room-temperature quantum efficiency of light-emitting diodes was 0.12%. © *2000 MAIK "Nauka/Interperiodica".*

1. INTRODUCTION

The 3–5 μm wavelength range includes absorption lines of several industrial and natural gases, i.e., of methane CH_4 (3.31 μm), sulfur dioxide SO_2 (3.9–4.0 μm), carbon dioxide CO_2 (4.27 μm), and carbon monoxide CO (4.7 μm). Because of this, light-emitting diodes (LEDs) operating in this spectral range are widely used in gas analyzers and are important for environment protection. Currently, liquid phase epitaxy [1–3], molecular beam epitaxy [4, 5] and metal-organic vapor-phase epitaxy (MOVPE) [6, 7] are widely used in the fabrication of IR LEDs based on InAsSb solid solutions. LED structures, as a rule, consist of an active region based on an InAsSb layer, or an InAsSb/InAs superlattice, sandwiched between InAsSbP or AlAsSb layers that provide optical and electron confinement. Although the InAs/InAsSb/InAs double heterostructure (DH) has a lower optical and electronic confinement than InAsSbP/InAsSb/InAsSbP or AlAsSb/InAsSb/AlAsSb structures, its fabrication is much simpler and less expensive.

The goal of this study was to fabricate LEDs emitting at room-temperature in the 3.9–4.0 μm wavelength range on the basis of MOVPE-grown InAs/InAsSb/InAs heterostructures.

2. EXPERIMENTAL

InAs/InAsSb/InAs structures were grown by MOVPE in a standard horizontal reactor under atmospheric pressure. The reactor design was similar to those previously described in detail [8, 9]. The LED structure consisted of (111)As-oriented n-InAs substrate ($n \simeq 2 \times 10^{16}$ cm^{-3}), successively overgrown with undoped layers of InAs (0.5-μm) and InAsSb (2 μm), and a zinc-doped p-InAs layer (1.5 μm).

The total rate of hydrogen flow through the reactor was 18 l/min. Trimethyl indium (TMIn), arsine (AsH_3) diluted with hydrogen to 20%, and trimethyl antimony (TMSb) served as indium, arsenic, and antimony precursors, respectively. Bubblers with TMIn and TMSb were maintained at 17.5 and –6°C, respectively. The rate of hydrogen flow through the TMIn bubbler was 190 cm^3/min in all the experiments. Diethyl zinc (DeZn) served as precursor in doping with zinc to obtain compounds with p-type conduction. The DeZn bubbler was maintained at 4.7°C. The rate of hydrogen flow through this bubbler was 20 cm^3/min. The undoped InAs layer was grown at a substrate temperature of 620°C, with the ratio [V]/[III] in the gas phase equal to 40. The InAsSb solid solution was grown at a substrate temperature of 620°C, with the gas-phase ratio [V]/[III] = 8.35, and TMSb/(TMSb + AsH_3) = 0.48. The p-InAs layer was grown at 575°C to suppress the diffusion of zinc.

The elemental composition of the solid solutions was determined using a CAMECA CAMEBAX X-ray microanalyzer.

The light-emitting structures were fabricated as mesa-diodes 300 μm in diameter by the conventional photolithographic technique. A continuous nonrectifying contact was deposited on the substrate. The point contact on top of the epitaxial structure was 100 μm in diameter. The nonrectifying contacts were formed by the vacuum deposition of gold and tellurium onto an n-type layer or gold and zinc onto a p-type layer.

The properties of the grown structures were studied using the photoluminescence (PL) and electroluminescence (EL) methods. The emission was recorded with a cooled InSb photodiode and a lock-in amplifier. The PL was excited by a GaAs diode laser (wavelength λ = 0.8 μm, output power in pulse mode 10 W, τ = 5 μs, and f = 500 Hz). The laser beam was directed onto the

1063-7826/00/3412-1402$20.00 © 2000 MAIK "Nauka/Interperiodica"

InAsSb solid-solution layer in the reflection mode. The EL from the LEDs was studied both in the pulse and CW modes at 77 and 300 K. Capacitance–voltage (*C–V*) and current–voltage (*I–V*) characteristics of the LEDs were measured at 77 and 300 K. The capacitance was measured using a standard bridge technique at 1 MHz.

3. RESULTS AND DISCUSSION

Let us consider the results obtained in studying the photoluminescent properties of the grown structures. The luminescent properties of MOVPE-grown *n*- and *p*-type InAs layers were discussed previously [10]. Calculations based on the model proposed in [11] showed that 7% of Sb in a InAsSb solid solution is necessary to obtain room-temperature emission peaked at 4.0 μm. This solid solution constituted the active region in our LED structure. Figure 1 shows a PL spectrum of the InAsSb solid solution that incorporated 7% of Sb and was grown on an epitaxial *n*-InAs layer. Two peaks are clearly observed in the spectra: the first (short-wavelength) is related to *n*-InAs ($h\nu_{max}$ = 410 meV, half-width $\Delta h\nu_{1/2}$ = 13 meV, which corresponds to an electron concentration of $\sim 2 \times 10^{16}$ cm^{-3}), and the second is related to the $InAs_{0.93}Sb_{0.07}$ solid solution ($h\nu_{max}$ = 363 meV, $\Delta h\nu_{1/2}$ = 25 meV). The larger half-width of the second peak is presumably related to the participation of two channels in the radiative recombination: the band–to–band and the band–to–(structural acceptors) [10]. The appearance of an InAs emission in the PL spectrum is associated both with the penetration of the exciting radiation into the epitaxial layer (or substrate) through the narrow-gap solid-solution layer whose thickness $d \simeq 0.5$ μm is less than $1/\alpha$ ($\alpha \simeq 10^4$ cm^{-1} is the absorption coefficient for the exciting light), and with the large diffusion length of minority carriers in InAsSb [12]. If the PL spectral peak for $InAs_{0.93}Sb_{0.07}$ is assumed to be related to direct band–to–band transitions, then the energy gap E_g in the parabolic band approximation and on the assumption of no degeneracy is $kT/2$ lower than the luminescence-peak energy, i.e. $E_g(T) = h\nu_{max}(T) - kT/2$ [13]. At 77 K, E_g can be estimated at 360 meV, which conforms with the value calculated for the $InAs_{0.93}Sb_{0.07}$ solid solution [11].

The carrier concentration in the barrier layers of the InAs LED structure was estimated from the PL spectra [10] at $n \simeq 2 \times 10^{16}$ cm^{-3} and $p \simeq 8 \times 10^{17}$ cm^{-3}. Figure 2 shows a room-temperature band diagram of the grown double heterostructure. The offsets of the conduction-band bottom and valence-band top were calculated using the model proposed in [11]. At the type II heterointerface, the band offsets are ΔE_c = –21meV and ΔE_v = 70 meV.

Figures 3 and 4 show the *I–V* and *C–V* characteristics, respectively, for the diode SOS-74-I-7. The cutoff voltage for the forward *I–V* characteristic approximately coincides with the band gap of the $InAs_{0.93}Sb_{0.07}$ solid solution at T = 77K. The residual resistance calculated from the *I–V* characteristic is R_r = 1.25 Ω at T = 77 K and 1.5 Ω at 300 K. The relatively high R_r (compared with the data of [14], where R_r = 0.3 Ω at T = 77 K and 0.5 Ω at 300 K) is presumably due to the high resistance of InAs substrates. The capacitance at zero bias was 70 pF. The dependence of capacitance on bias obeys the $1/C^2$ law, indicating the presence of an abrupt *p–n* junction. The width of the space-charge region evaluated from the *C–V* characteristic was 10^{-5} cm (V = 0). The low cutoff voltage in the $1/C^2 = f(V)$ dependence needs further study.

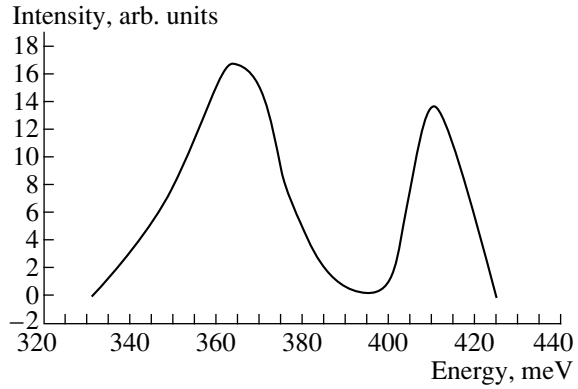

Fig. 1. PL spectrum of the $InAs_{0.93}Sb_{0.07}$ solid solution.

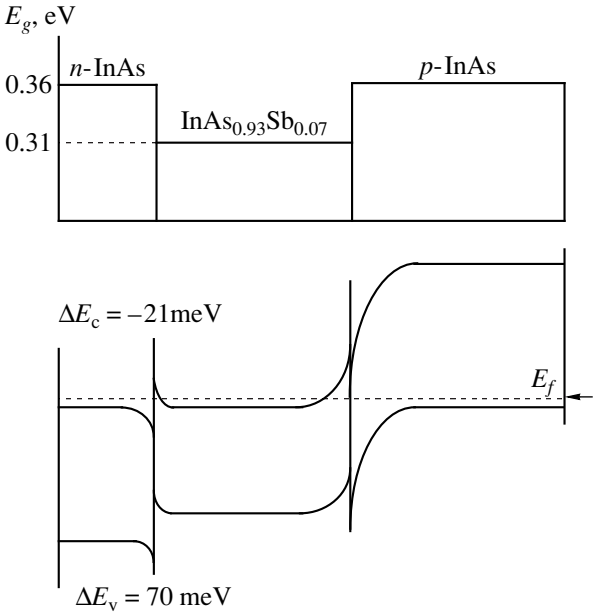

Fig. 2. Room-temperature band diagram of the *n*-InAs/*n*-$InAs_{0.93}Sb_{0.07}$/*p*-InAs(Zn) double heterostructure.

Figure 5 presents EL spectra for an *n*-InAs/*n*-$InAs_{0.93}Sb_{0.07}$/*p*-InAs(Zn) DH, measured in pulse mode at 77 and 300 K. At T = 77 K, four emission

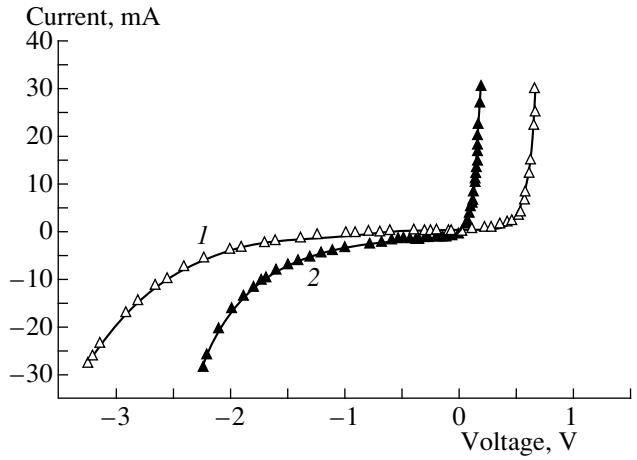

Fig. 3. *I–V* characteristics of SOS-74-I-7 diode at (*1*) 77 and (*2*) 300 K.

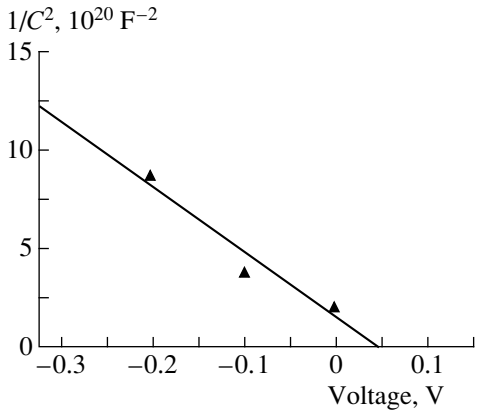

Fig. 4. Room-temperature *C–V* characteristic of SOS-74-I-7 diode.

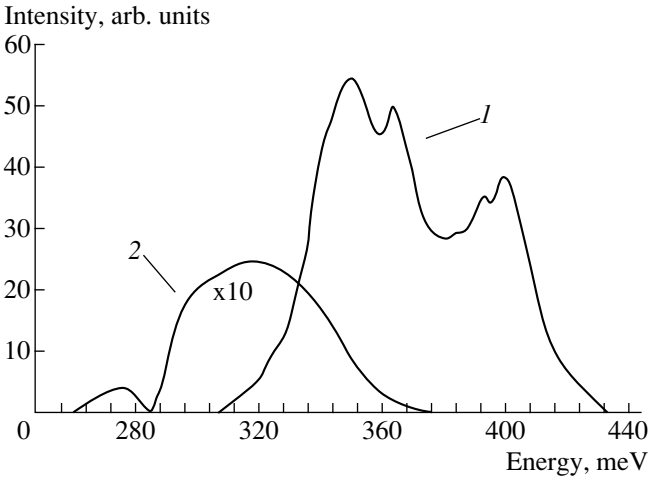

Fig. 5. EL spectra of the *n*-InAs–*n*-$InAs_{0.93}Sb_{0.07}$–*p*-InAs(Zn) double heterostructure at (*1*) 77 and (*2*) 300 K.

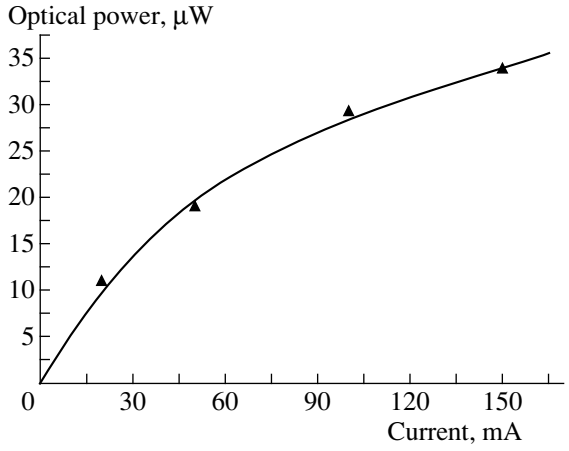

Fig. 6. Emission power as a function of the driving current for SOS-74-I-7 diode at room temperature in the quasi-continuous mode (f = 128 Hz).

peaks are observed at $h\nu$ = 400, 395, 364, and 350 meV. Of these peaks, the first two are related to band–to–band and band–acceptor recombination in InAs [10], and the second two, to band–to–band and band–to–acceptor recombination in the $InAs_{0.93}Sb_{0.07}$ solid solution. The half-width of the total emission spectrum is 75 meV. With the *p–n* junction assumed to be located at the *p*-InAs–*n*-InAsSb heterointerface, the InAs-related radiative recombination can presumably be explained by the fact that the diffusion lengths of nonequilibrium carriers exceed the active layer thickness. The EL peak at $h\nu$ = 364 meV which is similar to that in the PL spectrum corresponds to the band–to–band transition in the $InAs_{0.93}Sb_{0.07}$ solid solution. At 300 K, the EL spectrum of the LED is very broad ($\Delta h\nu_{1/2}$ = 54 meV) and is related to the recombination in InAs and $InAs_{0.93}Sb_{0.07}$, similarly to what is observed at 77 K. The $h\nu$ = 314 meV emission peak is due to interband transitions in the solid solution. The spectral feature at 300 meV is associated with the band–acceptor-level transition, shifted from its position at 77 K in accordance with the E_g temperature-variation coefficient $\Delta E_g/\Delta T = 2.8 \times 10^{-4}$ eV/K. The short-wavelength portion of the spectrum is related to radiative recombination in InAs. The absorption band of atmospheric CO_2 is clearly visible in the spectrum.

Figure 6 shows the emission power as a function of the pump current for an SOS-74-I-7 LED, measured in quasi-continuous mode (f = 128 Hz) at room temperature. The quantum efficiency of the device, calculated from this dependence, is 0.12%.

For the structures studied, the full width at half-maximum of the EL spectrum at T = 300 K is less than that for LEDs emitting at λ = 3.3 μm [7] (54 meV against 70 meV), and the lack of data on the quantum efficiency of the LED in the cited work complicates

comparison. Due to the insufficient optical and electron confinement, the power characteristics of the fabricated devices at 300 K are inferior to those for LEDs based on InAsSb/InAsP quantum-confinement structures with AlAsSb confining layers ($\lambda = 4.3$ μm, $W = 100$ μW in a quasi-continuous mode at an average current $I =$ 200 mA) [6]. The optical output power of the LEDs studied coincides approximately with that obtained in [5] for LEDs based on InAs/In(As, Sb) quantum-confinement structures ($\lambda \simeq 4.2$ μm, $W \simeq 30$ μW at $I =$ 200 mA). It was shown in [5] that the optical output power of LEDs can be raised by a factor of 3.5 by adding AlSb confinement layers to the InAs/In(As, Sb) structure. We hope that fabrication of InAsSbP confining layers will make a substantial increase in the emission power of LEDs possible.

4. CONCLUSION

$InAs/InAs_{0.93}Sb_{0.07}/InAs$ heterostructures were grown by MOVPE. The optimal conditions were determined for fabricating these structures in a horizontal reactor under atmospheric pressure. The luminescence properties of $InAs_{0.93}Sb_{0.07}$ layers and $InAs/InAs_{0.93}Sb_{0.07}/InAs$ heterostructures were studied. The simultaneous occurrence of interband recombination in InAsSb and radiative transitions involving acceptor levels was established. LEDs emitting at $\lambda = 3.45$ μm ($T = 77$ K), $\lambda = 3.95$ μm ($T = 300$ K) were fabricated on the basis of the structures grown. A quantum efficiency of 0.12% was obtained for LEDs operating at room temperature in the quasi-continuous mode ($f = 128$ Hz).

ACKNOWLEDGMENTS

We are grateful to T.S. Lagunova for measurements of galvanomagnetic properties of the grown layers. One of us (S.S.K.) is grateful to the Robert Havemann Foundation for supporting this study.

REFERENCES

1. A. Popov, M. V. Stepanov, V. V. Sherstnev, and Yu. P. Yakovlev, Pis'ma Zh. Tekh. Fiz. **23** (21), 24 (1997) [Tech. Phys. Lett. **23**, 828 (1997)].
2. B. Matveev, N. Zotova, S. Karandashov, *et al.*, IEE Proc.: Optoelectron. **145** (5), 254 (1998).
3. Y. Mao and A. Krier, Electron. Lett. **32** (5), 479 (1996).
4. W. Dobbelaere, J. De Boeck, C. Bruynseraede, *et al.*, Electron. Lett. **29** (10), 890 (1993).
5. C. Philips, H. Hardway, J. Heber, *et al.*, Proc. SPIE **3279**, 154 (1998).
6. R. Biefeld, A. Allerman, S. Kurtz, and K. Baucom, J. Cryst. Growth **195**, 356 (1998).
7. A. Stein, D. Putjer, A. Behres, and K. Heime, IEE Proc.: Optoelectron. **145** (5), 257 (1998).
8. S. Haywood, A. Henriques, N. Mason, *et al.*, Semicond. Sci. Technol. **3**, 315 (1988).
9. S. Haywood, N. Mason, and P. J. Walker, J. Cryst. Growth **93**, 56 (1988).
10. T. I. Voronina, N. V. Zotova, S. S. Kizhaev, *et al.*, Fiz. Tekh. Poluprovodn. (St. Petersburg) **33** (10), 1168 (1999) [Semiconductors **33**, 1062 (1999)].
11. S. Adachi, J. Appl. Phys. **61** (10), 4869 (1987).
12. P. I. Baranskiĭ, V. P. Klochkov, and I. V. Potykevich, *Semiconductor Electronics* (Naukova Dumka, Kiev, 1975).
13. O. A. Allaberenov, N. V. Zotova, D. N. Nasledov, and L. D. Neuĭmina, Fiz. Tekh. Poluprovodn. (Leningrad) **4** (10), 1939 (1970) [Sov. Phys. Semicond. **4**, 1662 (1970)].
14. N. V. Zotova, N. P. Esina, B. A. Matveev, *et al.*, Pis'ma Zh. Tekh. Fiz. **9** (7), 391 (1983) [Sov. Tech. Phys. Lett. **9**, 167 (1983)].

Translated by D. Mashovets

Semiconductors, Vol. 34, No. 12, 2000, pp. 1406–1409. Translated from Fizika i Tekhnika Poluprovodnikov, Vol. 34, No. 12, 2000, pp. 1468–1471.

PHYSICS OF SEMICONDUCTOR DEVICES

Emission-Line Broadening of Current Tunable InAsSbP/InAsSb/InAsSbP Heterostructure Lasers

A. N. Imenkov*, N. M. Kolchanova*, P. Kubat, S. Civish**, and Yu. P. Yakovlev***

** Ioffe Physicotechnical Institute, Russian Academy of Sciences, Politekhnicheskaya ul. 26, St. Petersburg, 194021 Russia*

*** J. Heyrovsky Institute of Physical Chemistry, CAS, 18223 Prague 8, Czech Republic*

Submitted June 1, 2000; accepted for publication June 1, 2000

Abstract—The dependence of emission-line broadening on the drive current was studied at 50–80 K for tunable InAsSbP/InAsSb/InAsSbP double heterostructure lasers operating in the 3.3–3.4 μm spectral region. For a small increase of the injection current I over the threshold current I_{th}, the line width depends on the $I - I_{th}$ difference hyperbolically, in accordance with the Schawlow–Townes and Henry theories that assume a homogeneous distribution of the nonequilibrium carrier concentration across the resonator width. With the current raised to $(3–4)I_{th}$, line narrowing ceases and the line starts to broaden with increasing current. The observed line broadening is explained by the effect of the nonequilibrium carrier concentration gradient between the middle of the resonator and its edges. In tunable lasers, this gradient increases with current, the lasing wavelength simultaneously decreasing. The minimal width of the lasing line is 10–20 MHz. © *2000 MAIK "Nauka/Interperiodica".*

1. At present, current tunable InAsSbP/InAsSb/InAsSbP double-heterostructure lasers emitting in the 3–4 μm spectral range are promising devices for studying the absorption spectra of gas molecules. Along with the output power, spectral range of tuning, and operating speed, the lasing line width is one of the key characteristics of tunable radiation sources designed for spectroscopy, since this width determines the precision of the reconstruction of gas molecule absorption bands and their identification. It has been shown previously that, for CH_3Cl, OSC, N_2O, and H_2O gases [1, 2], the power and the operation speed of the devices in question are sufficient for precise spectroscopic investigations of molecular vibrational rotational spectra in the gas phase. The problem of spectral range was discussed in [2], and the possibility of widening the range by using several lasing modes generated simultaneously was practically demonstrated. This study is aimed at determining the spectral line half-width for $\lambda = 3–4$ μm InAsSb/InAsSbP tunable lasers and to identify the factors affecting this width. This study continues earlier studies of the line width of 2 μm tunable lasers [3].

2. The lasing line width was studied for current-tunable InAsSbP/InAsSb/InAsSbP heterostructure lasers. The laser structures were LPE-grown on (100) *p*-InAs substrates with a 5×10^{18} cm^{-3} hole concentration, similarly to the structures described previously [1, 2]. The structure contains a ~1-μm-thick InAsSb active layer. The thickness of wide-gap emitters is 3 μm. The equilibrium carrier concentration in the undoped active region is about $(2–4) \times 10^{16}$ cm^{-3}. The hole concentration in the Zn-doped *p*-type confinement layer is $(1–2) \times 10^{18}$ cm^{-3}, and the electron concentration in the Sn-doped *n*-type confinement layer, $(5–8) \times 10^{18}$ cm^{-3}. After the epitaxial growth of the layers, the substrate was ground off to a ~100-μm thickness. Chips with a 500-μm step and a 10–100 μm mesa width were formed by photolithography. Cavities 250–375-μm long were obtained by cleavage. Laser structures were mounted on a copper heat sink [4].

3. The lasers were installed in a flow-through helium cryostat with a closed cycle (Laser Photonics L573) operating in the 12–100 K temperature range. The laser was driven by a dc current with a sawtooth modulation (modulation factor 0.02–0.03). The laser temperature and current were measured with Laser Photonics Model L5820 and Model L5731 devices.

The emission of a studied mode was selected by a grating monochromator and directed into a cell containing a gas under study or into a standard resonator, a Fabry–Perot etalon with neighboring resonance frequencies spaced by 0.026 cm^{-1}. CH_3Cl, N_2O, and OCS [1, 2] under pressure of ~1 Torr were used as reference gases. Further, the emission was detected by a cooled InSb photodetector. The detected and amplified signal U was fed into one channel of a Le Groy 9361 digital oscilloscope directly, and into the second channel of this oscilloscope, through a differentiating *RC* high-pass filter with time constant $\tau = 12$ μs.

The spectrum of the laser emission and its variation in the range of drive currents I from 1 to 5 threshold values (I_{th}) were studied at various temperatures in the range $T = 12–100$ K. The widest lasing-wavelength tuning range was observed at 50–70 K, and it is in this temperature range that most measurements were done.

1063-7826/00/3412-1406$20.00

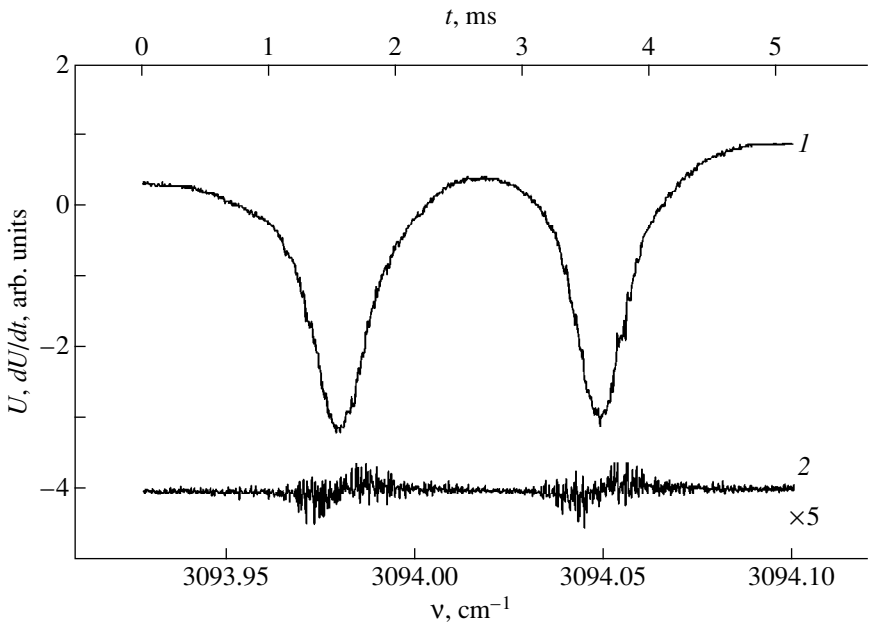

Fig. 1. Oscillograms of (*1*) the signal U proportional to the intensity of laser radiation passed through a cell with CH_3Cl gas, with the laser driven by sawtooth current, and (*2*) the time derivative of the signal, dU/dt, obtained after the signal passed an *RC* circuit.

4. Figure 1 shows oscillograms of the V-12191-3 laser signal U passed through a cell containing CH_3Cl (curve *1*), and the time derivative of this signal (curve *2*). The rate ν' at which the wave number ν of emission of a laser driven by a sawtooth-modulated current varied in time was determined from the time interval between the two minimums of the signal corresponding to the known CH_3Cl absorption lines [5, 6]. For some absorption lines, the rate ν' was determined from the natural frequencies of the standard resonator. In its second channel, the digital oscilloscope determined the linear-mean value of the derivative U_R and the rms deviation of the signal from its mean value $\langle U_\mu \rangle$. These values were measured at the inflection points of curve *1* (where these values are largest) and then were averaged. The half-width of the lasing line was determined at half-maximum and calculated by the relation

$$\Delta f = 2c\tau\nu'\langle U_\mu\rangle/U_R, \qquad (1)$$

where c is the speed of light.

Experimental lasing-line half-widths Δf strongly depend on the drive current I, as can be seen in Fig. 2, in which the half-width of the lasing line of a single-mode laser is represented as a function of the difference between the drive current I and the threshold current I_{th}. For a certain current $I = I_{min}$, the line half-width is the narrowest ($\Delta f = \Delta f_{min}$). For $I < I_{min}$, Δf decreases steeply, and for $I > I_{min}$, it grows gradually with increasing current; $I_{min} = (3–4)I_{th}$. This behavior remains the same for different absorbing gases (e.g., OCS or CH_3Cl). On changing $I - I_{th}$ by an order of magnitude, Δf varies less than twofold. In the laser under study, it remains within 32–18 MHz. For a multimode laser (V-1149-12), the minimal mode half-width Δf_{min} is nearly the same (see table) as in the single-mode lasers (MK 694-1 and V-12191-3). Another general feature was observed: Δf_{min} is smaller in the lasers with larger $I_{min} - I_{th}$ differences. Studies of multimode lasers demonstrated that the half-widths of several simultaneously generated modes differ by no more than 20%. Low-intensity modes do not affect substantially the half-width of the dominant mode. With the temperature deviating within ±10 K from the optimal value (for which the tuning range $\delta\nu$ is the widest) for a fixed $I - I_{th}$ difference, the line half-

Characteristics of the tunable InAsSb/InAsSbP lasers studied

Laser	ν, cm^{-1}	$\delta\nu$, cm^{-1}	T, K	I_{th}, mA	Gas	Δf_{min}, MHz	I_{min}–I_{th}, mA
V-1149-12	2806	2	68	50	N_2O	12	140
MK694-1	3031	3.6	70	120	CH_3Cl	10	210
V-12191-3	3095	10	60	45	CH_3Cl, OCS	18	120

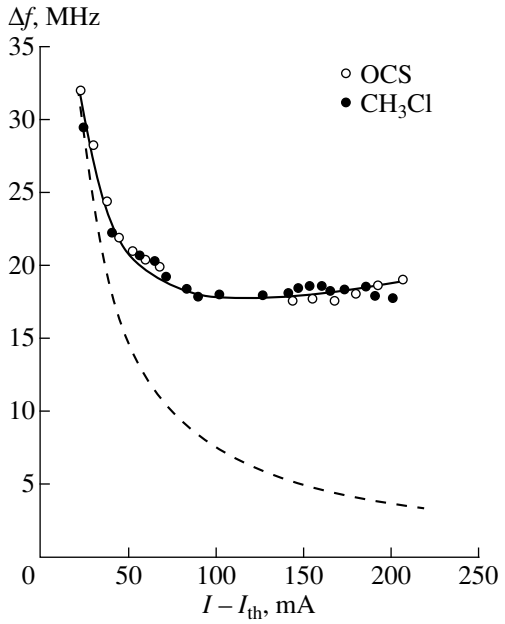

Fig. 2. Experimental values of the lasing-line half-width Δf for V-12191-3 laser for different currents (the half-widths were measured for the absorption bands of CH_3Cl and OCS gases), and theoretical dependences of Δf on current calculated under the assumptions of current-independent concentration of nonequilibrium carriers (dashed line) and a nonequilibrium carrier concentration increasing with current (solid line).

width changes in the same direction as does the absolute temperature, but to a lesser extent. For larger temperature deviations, the error in determining Δf grows owing to the increasing number of modes and decreasing signals from a separate mode.

5. We now discuss the experimental results. The decrease in the lasing-line half-width with increasing current, observed at small injection currents in the beginning of the tuning range, does not contradict the Schawlow–Townes theory for lasers [7]. According to this theory, the laser-line half-width Δf is inversely proportional to the laser-radiation intensity that increases with current in our case. Based on quantum-mechanical and statistical considerations, Henry [8, 9] obtained the following relation for the lasing-line half-width of semiconductor lasers:

$$\Delta f = \mathcal{R}(1 + \alpha_n^2)/4\pi P, \qquad (2)$$

where $\mathcal{R}$ is the average rate of spontaneous emission, α_n is the ratio between the variations of real and imaginary parts of the refractive index, and P is the number of photons in the cavity.

In considering radiation processes in semiconductor structures, Henry assumed that the average concentration of nonequilibrium carriers N is independent of the current if the threshold value N_{th} is exceeded. In this case, $\mathcal{R}$ and α_n are independent of the injection current, and the line half-width Δf is determined by the variation of the number of photons in the cavity P, which usually increases linearly with $I - I_{th}$ up to a certain $I - I_{th}$ value. Consequently, Δf decreases hyperbolically with increasing $I - I_{th}$, as observed in the experiment [10]. The dashed line in Fig. 2 represents the hyperbola calculated by formula (2) for the laser under study (V-12191-3) with the variation of the nonequilibrium carrier concentration with current disregarded. The Δf dependence on current is close to the calculated hyperbola only for small $I - I_{th}$ differences, while, in a wide current range, the calculated dependence lies much lower than the experimental points.

In tunable lasers, whose design gives rise to an optical waveguide, the concentration of nonequilibrium carriers increases toward the side edges of the waveguide, and this increase becomes more pronounced with increasing current [11]. The quantities $\mathcal{R}$ and α_n cannot be regarded as current-independent constants. Now taking into account the variation of the nonequilibrium carrier concentration with current does not yield a hyperbolic dependence of Δf on $I - I_{th}$, as was observed previously. Along with the experimental points and the hyperbola (dashed line), Fig. 2 shows (solid line) Δf calculated theoretically with account taken of the fluctuations of the nonequilibrium carrier concentration (these fluctuations give rise to fluctuations of the natural frequencies of the cavity) for a differential quantum efficiency of the laser equal to 0.44 and cavity length of 375 μm. The carrier concentrations affecting Δf and f were assumed identical:

$$N - N_s = [(\nu - \nu_s/\nu)]n/(-\partial n/\partial N), \qquad (3)$$

where N_s and ν_s are the N and ν values in the initial part of the range in which ν grows with current, and n is the refractive index.

Taking into account the nonuniform distribution of the carrier concentration in the waveguide of tunable lasers leads not only to deviation from the hyperbolic law, which occurs at small above-threshold currents ($I < 2I_{th}$), but also to the appearance of a minimum in the dependence of Δf on $I - I_{th}$ for $I = (3–4)I_{th}$ (solid line), as observed in our experiment. The calculated curve passes through practically all of the experimental points, and it lies substantially higher than the dashed curve obtained by assuming that the concentration of nonequilibrium carriers is independent of current.

The small difference between the width of separate lasing modes in multimode lasers can be explained by the simultaneous generation of these modes at the maximum of the gain spectrum. The simultaneous generation is due to self-suppression of modes, resulting from the long energy-relaxation time at low temperatures. In this case, no abrupt switching from one mode to another occurs and the distribution of carriers over the cavity remains, on average, unchanged. As a result, all the modes are involved in the suppression of spontaneous fluctuations of charge carriers, and the mode half-

width turns out to be independent of the number of modes.

To conclude, the lasing-line half-width and its dependence on current and temperature were studied for InAsSbP/InAsSb/InAsSbP laser structures. Consideration of the specific features of the waveguide, with the concentration of nonequilibrium carriers gradually increasing toward the waveguide edges and depending on current, leads to spectral line broadening; as a result, the line half-widths exceed those predicted by the Schawlow–Townes theory.

ACKNOWLEDGMENTS

This study was supported in part by the Program "Optics and Laser Physics," Ministry of Science of the Russian Federation, Grant Agency of the Academy of Science of the Czech Republic (grant no. 4040708), Russian Foundation for Basic Research (project no. 99-02-18109), and CRDF (grant RPO-695).

REFERENCES

1. A. P. Danilova, A. N. Imenkov, N. M. Kolchanova, *et al.*, Fiz. Tekh. Poluprovodn. (St. Petersburg) **34** (2), 115 (2000) [Semiconductors **34**, 237 (2000)].
2. A. P. Danilova, A. N. Imenkov, N. M. Kolchanova, *et al.*, Fiz. Tekh. Poluprovodn. (St. Petersburg) **33** (12), 1469 (1999) [Semiconductors **33**, 1322 (1999)].
3. V. G. Avetisov, A. N. Baranov, A. N. Imenkov, *et al.*, Pis'ma Zh. Tekh. Fiz. **16** (14), 66 (1990) [Sov. Tech. Phys. Lett. **16**, 549 (1990)].
4. A. Popov, V. Sherstnev, Yu. Yakovlev, *et al.*, Spectrochim. Acta, Part A **54**, 821 (1998).
5. A. G. Maki and J. S. Wells, *Wavenumber Calibration Tables From Heterodine Frequency Measurements NIST Special Publication 821* (Washington, 1991).
6. G. Gualachvili and K. Narahari Rao, *Handbook of Infrared Standards 11 with Spectral Coverage of 1.4–4 μm and 6.2–7.7 μm* (Academic, Boston, 1993).
7. A. L. Schawlow and C. H. Townes, Phys. Rev. **112**, 1940 (1958).
8. C. H. Henry, IEEE J. Quantum Electron. **QE-18**, 259 (1982).
9. C. Henry, in *Semiconductors and Semimetals*, Vol. 22: *Lightwave Communications Technology*, I: *Semiconductor Injection Lasers*, Ed. by W. T. Tsang (Academic, New York, 1985; Radio i Svyaz', Moscow, 1990), Chap. 3.
10. D. Welford and A. Mooradian, Appl. Phys. Lett. **40**, 560 (1982).
11. A. P. Danilova, T. N. Danilova, A. N. Imenkov, *et al.*, Fiz. Tekh. Poluprovodn. (St. Petersburg) **33**, 1088 (1999) [Semiconductors **33**, 991 (1999)].

Translated by D. Mashovets

Semiconductors, Vol. 34, No. 12, 2000, pp. 1410–1411. Translated from Fizika i Tekhnika Poluprovodnikov, Vol. 34, No. 12, 2000, pp. 1473–1474.

IN MEMORIAM

Sergeĭ Petrovich Solov'ev (1932–2000)

Sergeĭ Petrovich Solov'ev, Doctor of Physics and Mathematics, passed away on June 13, 2000, at the age of 68. He was a prominent scientist in the fields of experimental physics, solid-state physics, and the physics of semiconductors and insulators. He was a professor at the Institute of Physics and Power Engineering in Obninsk.

S.P. Solov'ev was born on September 18, 1932, into a large peasant family in the village of Malipki (Zagorsk region, Moscow oblast). After graduating from the Krasnozavodsk Chemical-Technology Technical College with distinction, he entered the Moscow Institute of Engineering Physics in 1951. In 1957, S.P. Solov'ev graduated with distinction from this institute and was assigned to the Karpov Research Institute of Physical Chemistry (Moscow) where he completed his undergraduate study concerned with X-ray diffraction analysis of ferroelectrics. After the completion of his postgraduate studies, S.P. Solov'ev defended his candidate thesis in 1960 and was assigned to the town of Obninsk to organize experimental studies at a large radiation-chemistry center (a branch of the Karpov Research Institute of Physical Chemistry) that was being set up at that time. The center was equipped with one of 15 Soviet research nuclear reactors (a VVR-ts water-cooled and water-moderated cylindrical reactor), high-power gamma-ray installations, and electron accelerators, which required the active participation of physicists.

From 1960 to 1982, S.P. Solov'ev worked at the Obninsk branch of the Karpov Research Institute. During the last decade, he was the director of this branch.

As a researcher, S.P. Solov'ev founded a solid experimental center at the Obninsk Branch and initiated research in the fields of neutron dynamics in solids and neutron and X-ray diffraction analysis (in collaboration with R.P. Ozerov and V.Ya. Dudarev). He also directed studies in the field of the radiation physics of solids and technical applications related to the radiation resistance and the radiation-induced modification of properties of inorganic nonmetallic materials (in collaboration with I.I. Kuz'min). After defending his doctoral thesis, S.P. Solov'ev directed and supervised the studies of his young colleagues and founded his scientific school in Obninsk; he also ensured the success of a large number of application-oriented studies related to important national projects. S.P. Solov'ev received the title of professor in 1978. He participated in many international crystallographic congresses, in conferences on ferroelectricity, and in regional conferences on crystallography, ferroelectricity, and solid-state radiation physics. A large number of candidate and doctoral theses have been written and defended under his supervision and guidance. S.P. Solov'ev was a member of two special councils of the Academy of Sciences of the USSR and was the deputy Editor-in-Chief of the journal *Nuclear Power Engineering*.

In collaboration with leading scientists and technologists from many academic and industrial institutions and organizations and with the support of the President of the Academy of Sciences, Academician A.P. Aleksandrov, S.P. Solov'ev initiated pioneering studies related to permutation-induced doping of semiconductors on the basis of a VVR-ts nuclear reactor. At the Obninsk branch of the Karpov Institute, all technological stages of the process of permutation doping were studied in detail (a gold medal was awarded for this research by the Exhibition of Economic Achievements of the USSR), and the mechanisms of formation and annealing of radiation defects were also investigated. As a result of these studies, the required technological line was assembled and large-scale production of ingots of transmutation-doped silicon was organized. Currently, the radiation technology developed at the Obninsk Branch of the Karpov Institute is used to dope

1063-7826/00/3412-1410$20.00 © 2000 MAIK "Nauka/Interperiodica"

silicon single crystals for a number of foreign companies on a contract basis.

S.P. Solov'ev (in collaboration with N.G. Kolin) started long-term studies on transmutation doping of III–V semiconductors and radiation-induced modification of properties of these compounds; in these studies, a VVR-ts reactor was used. The technology was developed to the level of small-scale production of single-crystal wafers, including those of high-quality radiation-modified semi-insulating gallium arsenide with a diameter as large as 104 mm. This research is currently being conducted with the participation and support of the Lawrence Livermore National Laboratory (Berkeley, California).

Based on the results of his studies, S.P. Solov'ev (with L.S. Smirnov, V.A. Kharchenko, and V.F. Stas' as coauthors) wrote and published the book entitled *Doping of Semiconductors by the Method of Nuclear Reactions* (Nauka, Novosibirsk, 1981).

In 1983, S.P. Solov'ev began his administrative and tutorial activity at the Obninsk Branch of the Moscow Institute of Engineering Physics (now MATÉ). For many years, S.P. Solov'ev acted as vice principal (concerned with educational matters) and was the head of the Department of Nuclear Electric Power Plants and, later, the Department of Materials Science. In recent years, he concentrated on lecturing. S.P. Solov'ev, as an expert on and a participant in the elimination of the Chernobyl catastrophe consequences, was the editor of the textbook *Accidents and Incidents at Nuclear Electric Power Plants*. He participated in preparation of the textbook *Physical Crystallography* for senior students.

S.P. Solov'ev was very active and was a man of principles; these traits along with his democratism and kindness made him a recognized leader. S.P. Solov'ev worked to the fullest extent and thus received the appreciation of the government.

The death of S.P. Solov'ev is an irreplaceable loss to his colleagues and friends.

V. N. Brudnyĭ, V. T. Bublik,
B. N. Goshitskiĭ, V. V. Emtsev,
Yu. A. Kazanskiĭ, R. F. Konopleva,
Yu. V. Konobeev, N. G. Kolin, I. I. Kuz'min,
M. G. Mil'vidskiĭ, R. P. Ozerov,
V. B. Osvenskiĭ, V. G. Plotnikov,
A. P. Simonov, L. S. Smirnov,
and V. A. Kharchenko

Editorial Board of the journal
Fizika i Tekhnika Poluprovodnikov

Translated by A. Spitsyn